Characterization of Hydrothermal Alteration in Mount Berecha Area of Main Ethiopian Rift using Hyperspectral Data

OLUWADEBI AYOMIPOSI GRACE
February, 2011

SUPERVISORS:
Mr. C.A. Hecker (MSc)
Prof. Dr. F.D. van der Meer

Characterization of Hydrothermal Alteration in Mount Berecha Area of Main Ethiopian Rift using Hyperspectral Data

OLUWADEBI AYOMIPOSI GRACE
Enschede, The Netherlands, February, 2011

Thesis submitted to the Faculty of Geo-Information Science and Earth Observation of the University of Twente in partial fulfilment of the requirements for the degree of Master of Science in Geo-information Science and Earth Observation.
Specialization: Applied Earth Sciences

SUPERVISORS:
Mr. C.A. Hecker (MSc)
Prof. Dr. F.D. van der Meer

THESIS ASSESSMENT BOARD:
Prof. Dr. F.D. van der Meer (Chair)
Dr. P.M. van Dijk (External Examiner)

ABSTRACT

An understanding of hydrothermal alteration is of great value because it provides insight into origin of ore fluids as well as chemical and physical attributes of ore (deposit) formation. Recent discovery of gold in Main Ethiopian Rift (MER) system is related to felsic peralkaline volcanics and basin-fill volcanoclastic sediments of the rift system but much is yet to be known about the hydrothermal alteration system of the MER. This study is about understanding the characteristics of hydrothermal alteration in Mount Berecha area of Main Ethiopian Rift and the potential for the mineralization in the area.

Airborne Imaging Spectroradiometer for Applications (AISA) Hawk data was used to identify and map hydrothermal alteration mineralogy in Mount Berecha area of Main Ethiopian Rift valley. The Airborne image mapping was coupled with laboratory analysis involving reflectance spectroscopic measurements with the use of ASD FieldSpec Pro for mineral and rock samples. Pre-processing of the AISA Hawk data was performed and different mapping methods such as Wavelength of Minimum, Wavelength Mapping, Minimum Noise Fraction (MNF) transformation and Spectral Angle Mapper (SAM) classification were applied. The study was based in the shortwave infrared wavelength (SWIR) region, laboratory spectra acquired from field data analysis serves as guide in selecting image endmembers used as input in the SAM classification for mineral mapping. In addition to this, LiDAR-DEM data was used to map structures (lineaments) in the area which was later integrated with hyperspectral data to understand the impact of structure on spatial distribution of the alteration minerals.

SWIR spectroscopy was able to detect the main very fine grained mineral assemblages which occur in the study area, including Kaolinite, Halloysite, Opal, Montmorillonite, Nontronite, Calcite, K-alunite, Palygorskite, MgChlorite, Zoisite, Illite and mixture of these minerals. Wavelength mapping algorithm show clear difference between altered areas and unaltered area as well as patterns within the altered areas; MNF reveals the dimensionality of the Hawk data and show spectrally distinct areas while SAM classification algorithm gives the overall classification of the alteration minerals of Berecha area and was used to generate the surficial mineral map of the study area. Kandite mineral group (kaolinite and halloysite) are mostly distributed over the study area with less abundance of smectite (montmorillonite). Opal and palygorskite are also common over the study area. Structural information extracted from LiDAR-DEM data integrated with alteration mineral map reveals the control of structure on spatial distribution of the alteration minerals. Comparison of alteration in Berecha area with conceptual model of high sulfidation and low sulfidation systems indicates that Berecha alteration is related to low sulfidation system. The most widespread alteration effects are represented essentially in advanced argillic alteration assemblage consisting mainly of kaolinite + opal + smectite ± alunite which is likely of steam heated origin. Quartz veining and shallow silicification is common in the area. Few occurrences of pyrite and bladed calcite were found in the study area.

Keywords: Hyperspectral, Imaging Spectrometry, AISA Hawk, LiDAR-DEM, Wavelength Mapping, Berecha, ASD FieldSpec Pro, Minimum Noise Fraction, Spectral Angle Mapper, Minimum Noise Fraction

ACKNOWLEDGEMENTS

First and foremost, my appreciation goes to God Almighty for His sustaining grace, strength and successful completion of my MSc program. Ebenezer unto him for hitherto he has helped me. Many thanks to the Netherland Fellowship Program (NFP) for providing the financial support needed to make this MSc a reality.

My profound appreciation goes to my supervisors. Mr Chris Hecker, my first supervisor for his scientific comments, recommendation and assistance in making available important dataset for this research as well as his memorable support and assistance during the field work stage. I would also like to thank Prof. Dr. Freek van der Meer, my second supervisor, for providing advice and suggestions which improved the content and scientific level of this thesis.

I also want to thank Drs. T.M. Loran, the Applied Earth Science (AES) Course Director for his efforts in ensuring a successful running of the MSc program. Many thanks also to Drs. Boudewijn de Smeth for his advice and encouragement during the study period at ITC and to Dr Harald van der Werff for his contribution to this research work. I also thank Dr. F.J.A van Ruitenbeek, Dr. E.J.M Carranza and all the staff of Earth Resources Exploration stream for their valuable instructions during this program.

I would also like to thank the Airborne Research and Survey Facility of the Natural Environment Research Council (NERC-ARSF) and Principal Investigator Dr. Graham Ferrier, University of Hull for providing the airborne data sets.

I also appreciate Mr Raul Pablo Andrada De Palomera for his advice and assistance during this research work. Many thanks to the staff of Geological Survey of Ethiopia for their assistance during the field work and especially to my field work mate, Mr Ferede Gobena.

Undoubtedly, my sincere gratitude goes to my loving and understanding husband, Mr Joseph Olawale Oluwadebi and my little daughter, Treasure Oluwadebi for their patient, sacrifice and unbroken link during my MSc program. I also appreciate my brothers, sisters and my extended family for their prayers and encouragements during my stay in the Netherlands. Thanks to Engr. Rotimi Oladimeji, the head of Water Supply Department of Ondo State Water and Sanitation Project (WATSAN) for his encouragement and support during my MSc study.

Thanks to all members of International Christian Fellowship (ICF), Enschede for their spiritual and moral support during my MSc study. Special thanks to all members of support group of ITC fellowship for the love shown all through my stay in Netherlands.

To all my classmate of Applied Earth Science, friends and colleague from Nigeria, I say thank you.

TABLE OF CONTENTS

LIST OF FIGURES

LIST OF TABLES

LIST OF ABBREVIATIONS

3-D	Three Dimensional
AISA	Airborne Imaging Spectroradiometer for Applications
AMSL	Above Mean Sea Level
ASD	Analytical Spectral Device
ASTER	Advanced Spaceborne Thermal Emission and Reflection
CSIRO	Commonwealth Scientific and Industrial Research Organisation
DEM	Digital Elevation Model
EARS	East African Rift System
ENVI	Environment for Visualizing Image
FCC	False Colour Composite
GPS	Global Positioning System
IMU	Inertial Measurement Unit
KCI	Kaolinite Crystallinity Index
LIDAR	Light Detection and Ranging
MER	Main Ethiopian Rift
MIN	Minimum
MNF	Minimum Noise Fraction
SAM	Spectral Angle Mapper
SIFM	Spectral Interpretation Field Manual
SNR	Signal to Noise Ratio
SWIR	Short Wave InfraRed
TSA	The Spectral Assistant
TSG	The Spectral Geologist
USGS	United State Geological Survey
VIS	Visible
VNIR	Visible and Near InfraRed

1. INTRODUCTION

Hyperspectral imagery has been proved successful in the mapping of hydrothermal alteration minerals particularly since early 1980's and it has represent a mature and established technology (Kruse et al., 2003). Abundant information about many important earth-surface minerals is found within the spectral range of 0.4 – 2.5 μm. In particular, the 2.0 – 2.5 μm shortwave infrared (SWIR) spectral range covers spectral features of hydroxyl-bearing minerals, carbonates and sulfates, common to many geologic units and hydrothermal alteration assemblages (Goetz et al., 1985).

Hydrothermal alteration is a complex process involving chemical replacement of original minerals in the rock by new minerals where a hydrothermal fluid delivers the chemical reactants and remove the aqueous reaction products (Reed, 1997). An understanding of hydrothermal alteration is of great value because it provides insight into origin of ore fluids as well as chemical and physical attributes of ore (deposit) formation.

A typical example of hydrothermal altered area is found in Mount Berecha area of the Main Ethiopia Rift (MER). Much study has not been carried out in this area, the alteration type and the age of the system is not known neither is the potentials for metal deposits associated with it. However, a unique combination of remote sensing data (hyperspectral and LiDAR) that is available for this research will assist in making regional geologic interpretation of the area and to understand better the hydrothermal alteration system of the area.

According to Abebe et al. (2007), the rift valley is the dominant physiographic and tectonic structure splitting Ethiopia from north to south. Extensive on-going volcanic activity is associated with the rift valley producing large volumes of basaltic and silicic volcanic. Studies have shown that various volcanic rock hosted epithermal deposit and precious base metal deposits are distinguished with certain characteristics. These characteristics include the ore, gangue, alteration mineral assemblages, chemical composition of the fluids, the spatial and temporal distributions of these assemblages, host-rock composition, age relations between ore deposition and emplacement of the host rock, size of the district, temperatures of mineral deposition, paleodepth estimates, origin(s) of the fluids, and regional geologic setting. However, estimation of relative value of each of these features for distinguishing epithermal precious and base metal deposits shows that alteration mineral assemblages and veins are the most important factors (Heald et al., 1987). Therefore, mapping of hydrothermal alteration mineralogy plays a significant role in mineral exploration.

1.1. Problem Statement

Traditionally, rift systems are not considered prospective for gold mineralization but have been discovered to be important for soda ash, diatomite, bentonite, salt, sulfur, and pumice which is abundantly found on the floor of the Rift (Demessie, 1996). The occurrence of gold in various part of Ethiopia is known to be associated with the metamorphic rocks (green schist facies & amphibolites facies), low-grade bimodal meta-volcano sedimentary island-arc (ophiolitic suites) and syn-tectonic to post-tectonic intrusive (Tadesse, 1999; Tadesse et al., 2003).

Recently, there has been gold discovery in the rift system which is related to the felsic peralkaline volcanics and basin-fill volcanoclastic sediments of the rift system (Tadesse et al., 2003), but much is yet to be known about the hydrothermal alteration system of the study area.

This research is to contribute to better understanding of the characteristics of hydrothermal alteration in Mount Berecha area of Main Ethiopian Rift system which will assist in determining the potential for the mineralization in the area. A remote sensing approach of utilizing new hyperspectral methods integrated with LiDAR (Light Detection And Ranging) offers the capability to resolve the key geological features of this geologically dynamic area. The hyperspectral data will be utilized for mineralogical mapping at the surface in order to understand the spatial distribution of hydrothermal alteration minerals while the LiDAR data will be used to map structures and their control on alteration mineral distribution and through that have knowledge on the potential mineralization. These datasets, will enable a characterization of hydrothermal alteration system in Mount Berecha area which is a remote and poorly understood area.

1.2. Research Objectives

1.2.1. General Objective

The overall objective of this research is to study the characteristics of the hydrothermal alteration in Mount Berecha area of the Main Ethiopian Rift system by mapping the surface mineralogy and structural features associated with these alteration systems.

1.2.2. Specific Objectives

The above objective will be achieved by focusing on the under listed sub objectives

- To identify different lithological units and hydrothermal mineral assemblages in the study area.
- To link the spatial distribution of the minerals to the factors that controls their distribution.
- To identify the type of system that is associated with the hydrothermal alteration of the study area.

1.3. Research Questions

- Which lithological units and mineral assemblages can be mapped from the study area using remote sensing data?
- Do factors like structure and lithology control the spatial distribution of the minerals in the study area?
- Which type of system is associated with hydrothermal alteration of the study area and can it be compared with systems that occur in some other part of the world?

1.4. Datasets and Research Setup

1.4.1. Datasets

The following datasets were available for processing and analysis in this research:

- AISA Hawk Airborne Hyperspectral data
- LiDAR-DEM data
- ASTER image scene
- Topographic map
- Geology map of the area

1.4.2. Software

Software use in the course of the research includes:

- ENVI 4.7
- AZGCORR
- PyENVI
- TSG
- ViewSpecPro
- ArcGIS 10
- ArcScene

ENVI 4.7 is mainly use for hyperspectral analysis. AZGCORR is for geometric correction of the Hawk data. PyENVI is use for hyperspectral pre-processing and processing such as image destriping, log residual, wavelength mapping etc. ViewSpecPro is to check and visualize spectral while TSG is to analyze and interpret field spectral data as well as to calculate their absorption depths and wavelength region. ArcGIS 10 is for digitizing, georeference of topographic maps, and to capture various map in a database. ArcScene is to visualize data in three dimensional view (3-D).

1.4.3. Research Setup

In order to answer the research questions, the following methods were followed:

1. Literature review: Review of geology of the area was done to know the link between geology and alteration mineralogy in the area. Also, review on application of remote sensing in mineral mapping was considered.
2. Digitization of geological map of study area from existing regional geology map of MER after (Tsegaye et al., 2005).
3. Remote sensing data preliminary processing: Data such as AISA Hawk data and ASTER data were processed for identification of field work target area.
4. Field work (between 5th – 26th September, 2010): involving mineral and sample collection as well as spectra acquisition.
5. Analysis of laboratory spectra acquired from samples (minerals and rocks).
6. Hyperspectral airborne (AISA Hawk) data and LiDAR-DEM processing, analysis and interpretation.
7. Data Integration: This involved integration of structural map with mineral map as well as result from field analysis to know the impact of structure on mineral distribution in the study area.

The overall methodology flowchart for this research is explained in Figure (1.1).

1.5. Organization of Thesis

The thesis consist of seven chapters,

- Chapter one emphasizes the research problem, overall and specific objectives, research questions as well as dataset and software available for the research.

- Chapter two deals with literature review on the geology and tectonic setting of the study area as well as review on remote sensing for mineralogical mapping.

- Chapter three describes the instrumentation and datasets used for the research.

- Chapter four emphasizes the methodology involved in the research processing and analysis of the mineral and rock collected from the study area, remote sensing data pre-processing and analysis (mainly AISA Hawk hyperspectral data) and analysis of LiDAR-DEM data.

- Chapter five centers on results and discussion from various methodology applied in the research study and relationship of this with hydrothermal alteration systems of Berecha area.

- Chapter six deals with linkage of result to conceptual models of hydrothermal system in relation to Berecha area.

- Chapter seven gives the conclusion, recommendation and limitations of the study.

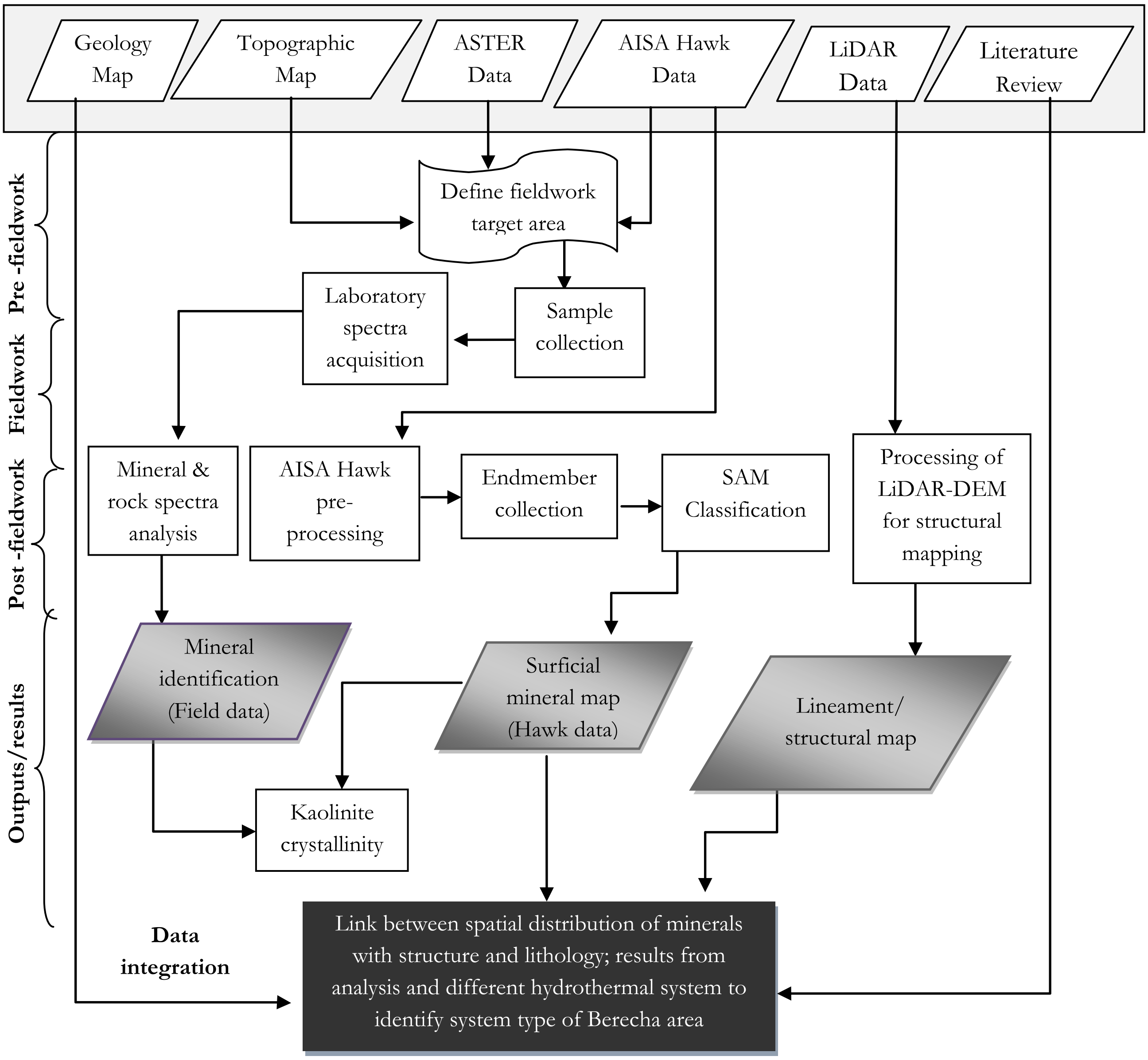

Figure 1.1: Research Methodology Flowchart

2. LITERATURE REVIEW

This section deals with literature review on the geology and tectonic setting of the study area as well as review on remote sensing for mineralogical mapping.

2.1.1. Location of Study Area

Mount Berecha area is situated in the central part of the Main Ethiopian Rift (MER) valley near the city of Nazret (Figure 2.1a). It is located within latitudes 8^{0}9'28.91''N and 8^{0}16'1.95''N, and longitudes 38^{0}58'30.14''E and 39^{0}7'20.22''E. The study area is bounded by Lake Koka to the north and to the north-east by Wonji Sugar plantation and Gademsa caldera (Figure 2.1b). It is accessible through two main asphalted high ways, Mojo - Alem Tena and Nazret - Assela road.

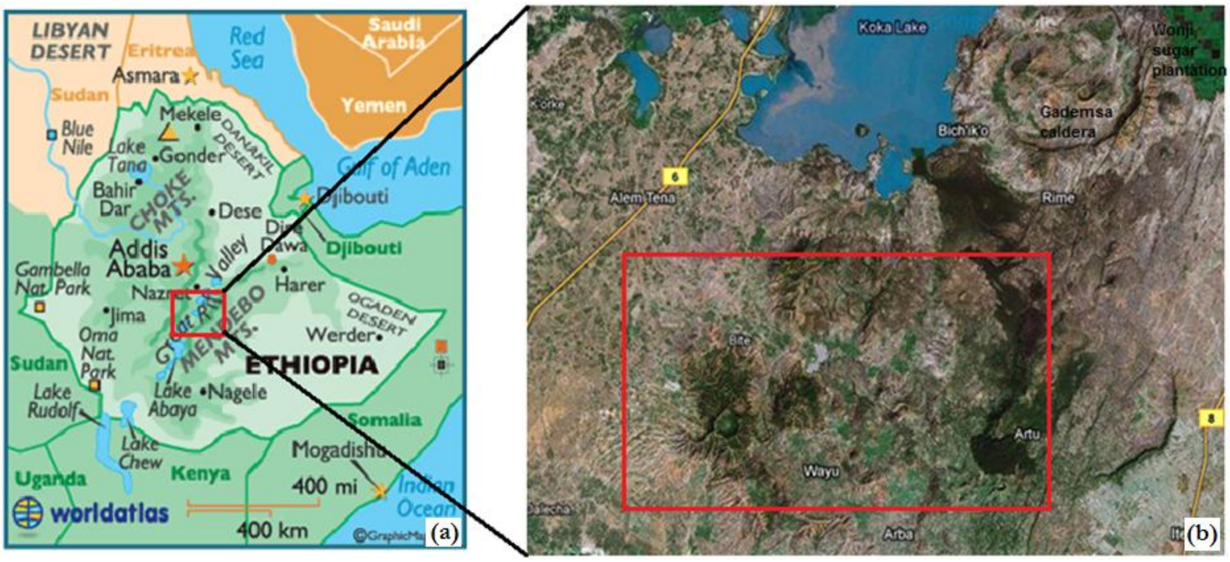

Figure 2.1: (a) Location of study area from www.worldatlas.com; (b) Study area (in red box) and environs from Google map

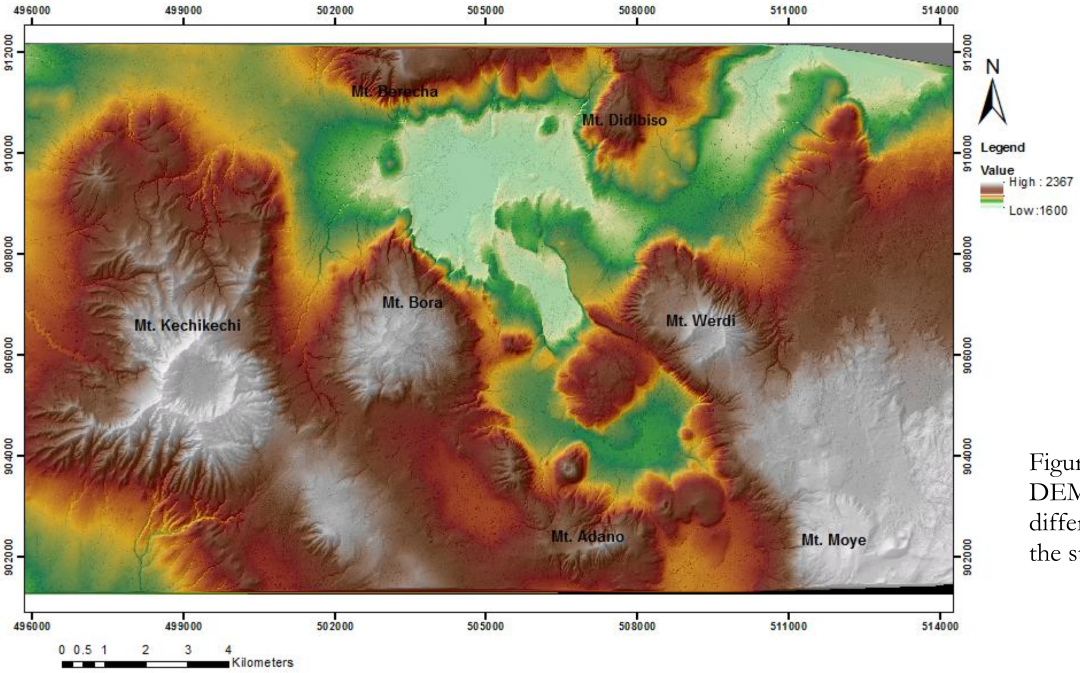

Figure 2.2: LiDAR-DEM showing different elevation of the study area

Mount Berecha area is characterized by the occurrence of both mountainous and flat topography. The elevated topography is associated with the major volcanic centers which include; Mt. Kechikechi, Mt. Berecha, Mt. Bora and Mt. Tulu Moye. Less elevated volcanics include; Mt. Adano, Mt. Werdi, and Mt. Didibiso (Figure 2.2). Flat volcano-sedimentary plains characterize the areas between the volcanic centers.

The study area is a dry area with natural vegetation mainly covered by shrubs, acacia, perennial grasses and herbs. The region is characterized by alternating wet and dry seasons with mean annual rainfall of about 7000 mm (Ayele et al., 2002). Mean annual temperature is more than 20ºC in the area and evaporation ranges from more than 2500 mm (Caroline Le Turdua et al., 1999).

2.2. Regional Geology and Tectonic Setting of the Main Ethiopian Rift

According to Abebe et al. (2007), the Main Ethiopia Rift (MER) constitute the north-eastern part of the East African Rift System (EARS) and comprises a series of rift zones extending over a distance of about 1000 km from the Afar Triple Junction at the Red Sea-Gulf of Aden intersection to the Kenya Rift. The MER is divided geographically into three sectors: northern, central and southern (WoldeGabriel et al., 1990), the study area falls within the central part (Figure 2.3).

The MER is marked by recent volcanic products (rocks) which are represented by composite volcanoes and by caldera structures (Boccaletti et al., 1998). According to WoldeGabriel et al (1990), most of the geologic sections exposed along the MER is dominated by the Tertiary volcanic rocks except for a few locations where Mesozoic sedimentary and /or Tertiary volcanic rocks unconformably overlain the crystalline basement .

The MER developed during Late Miocene and it is also characterized by well-developed Quaternary faulting that is mostly related to Wonji Fault Belt (Boccaletti et al., 1999) and striking between NNE–SSW in the south and NE–SW in the north (Korme et al., 2004). The faulting in the central part of MER strikes in different direction. Areas like Aluto and Bora-Berecha are slightly dissected by NW–SE faults. Aluto-Gedemsa strikes in N–NNE whereas the Bosetti-Fantale zone is a NE–SW volcanic field flanked and partially dissected by NNE faults (Abebe et al., 2007).

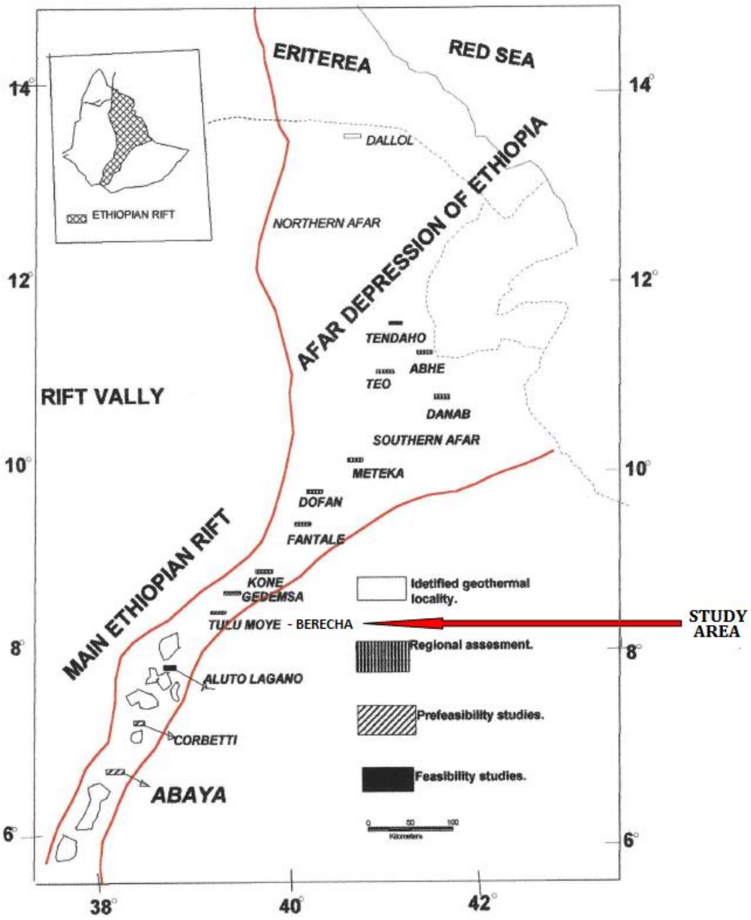

Figure 2.3: Map of Main Ethiopian Rift showing study area after (Ayele et al., 2002)

The MER is associated with bimodal Quaternary magmatism. Field and geochronology data have been used to examine the relationships between acidic volcanoes and basaltic eruptions (Abebe et al., 2007). Two main quaternary magmatic episodes have been recognized in the MER; (i) basaltic flows followed by ignimbrites and silicic centers in the rift floor (2-1 Ma) and (ii) axial silicic volcanoes and basalts since ~650 ka. The interaction between the silicic and basaltic volcanism is complex and strongly influenced by faulting. Mineralization in Ethiopia is mostly associated with Precambrian crystalline basement and the Tertiary formations which contain metallic and industrial minerals and rocks (notably gold, platinum, rare metals, nickel, copper, iron, chromium, kaolin, feldspar, clay, asbestos, talc, marble, limestone and granite). However, the MER volcanics and sediments have also known to be important for geothermal energy, epithermal gold, soda ash, diatomite, bentonite, salt, sulphur, pumice etc (Tadesse et al., 2003). Therefore understanding hydrothermal alteration system of Berecha area (central part of the rift) which epithermal gold might be associated with is important and the focus of this study.

2.3. Geology of Mount Berecha Area

Berecha area exists in the central part of the Main Ethiopian Rift valley which is mostly covered by ignimbrite rock (Dipaola, 1970). Berecha ignimbrite is the youngest unit out of the three ignimbritic units of the volcanic complex that belongs to a bimodal magmatic suite erupted between 830 Ka and 20 Ka (thousand years)(Trua et al., 1999). The recent felsic products of the Berecha unit consist of pantelleritic ignimbrites and obsidian lava domes and flows ranging from 240 - 20 Ka. The pyroclastics are unwelded pumice flows and ashes, which are the final products (Boccaletti et al., 1999). Berecha area consist of Pleistocene – Holocene (<1.6 Ma) volcanic complex with volcano-sedimentary rocks which is Recent (< 500 Ka) (Tsegaye et al., 2005). Figure (2.4) show geology map of Berecha area and the sequences of the volcanic rocks.

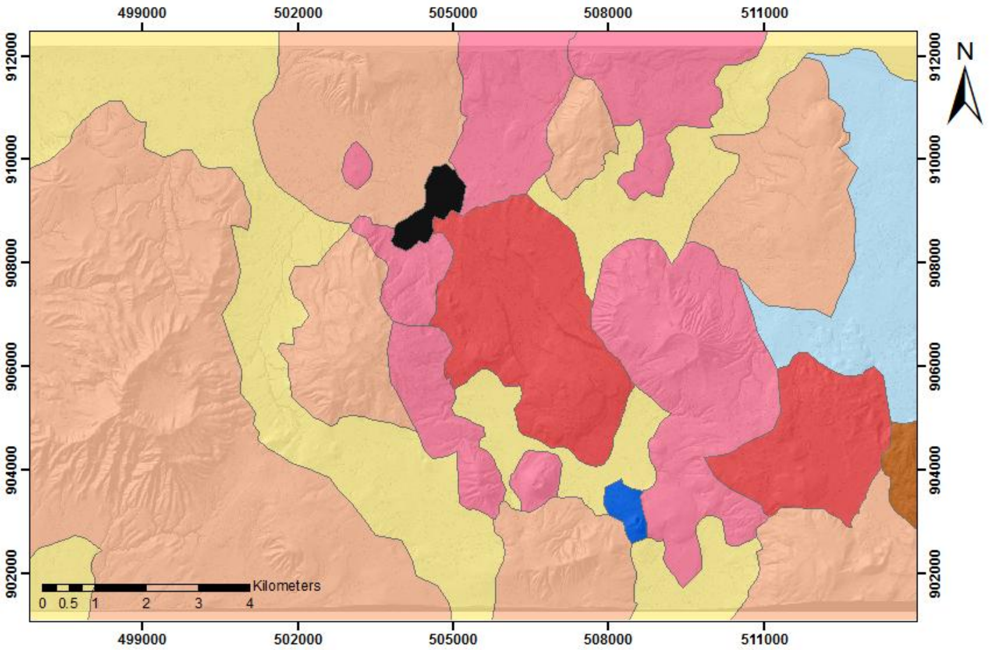

Lithology

■ Lake (Water body)

Recent (<500 Ka)

🟨 Alluvial (Sand and silt with abundant component of volcanic origin)

Pleistocene – Holocene (<1.6 Ma)

🟫 Comenditic obsidian lava flows and domes
🟥 Trachyte (Porphyritic glassy trachytic lava flow)
🟦 Basalt (Alkaline to olivine basaltic lava flow with minor tholeiites)
🟧 Pumice (Pyroclastic deposits, fine ash falls and flow)
🟪 Rhyolite (Comenditic and pantelleritic lava flows and domes)
🟦 Basalt (Scoria cones and fallout deposits)

STRATIGRAPHY COLUMN		
AGE	ROCK TYPES	CODE
Recent	Alluvium	Ls
Pleistocene – Holocene	Obsidians	Brd
	Trachytes	Brc
	Basalt	Wba
	Pumice Pyroclastics	Bra
	Ryholites	Brb
	Older Basalts (Scoria cones)	Wbb

Figure 2.4: Geology map of Berecha area and stratigraphy column of the lithological units after (Tsegaye et al., 2005)

The following volcanic sequence exists in Berecha area from youngest to oldest; Obsidians (Brd), Trachytes (Brc), Basalt (Wba), Pumice Pyroclastics (Bra), Ryholites (Brb) and Older Basalts (Wbb). The vocano-sedimentary unit is the alluvial (Ls) sediments (Ayele et al., 2002; Tsegaye et al., 2005).

- **Obsidian (Brd):** Obsidian is a volcanic rock found in the area. It forms thick viscous lava flow associated with pumice. The porphyritic type is abundant in the area while sometimes there are those with non-porphyritic (fine dark shining crystals) occurring in the area.

- **Trachyte (Brc):** Trachyte occurrence in the area is not as much as pumice and rhyolite. They are formed from the moderate domes with numerous large alkali feldspar (Anorthoclase), pyroxene and quartz. The lava flows from this unit are inferred to be highly viscous, as signify by vitrophyric texture (glassy), dark grey colour and moderately porphyritic to coarsely porphyritic (Tsegaye et al., 2005).

- **Pumice (Bra):** Pumice is well represented in the area and found in almost every part of the study area. They are mainly characterized by pumice breccias and sometimes by lithic breccias. They consist of thin layers of volcanic sands or ashes interbedded with silt or clay, brownish to yellowish in colour (Figure 2.5a). They probably formed from distinct volcanic center as pyroclastic flow, fine ash fall or as air-falls (Dipaola, 1970). The pumice pyroclastic deposits are altered in the area.

- **Rhyolite (Brb):** Rhyolite covers large part of the area and formed from the acidic lave domes. Texturally, there are varieties of phenocrysts. Most commonly occurring minerals are alkali feldspar (sadine and orthoclase) and quartz. Clinopyroxene (aegirine and aegirine-augite), biotite, amphibolites (hornblende) and opaque minerals occur in minor quantity (Tsegaye et al., 2005). The rhyolite in the area is highly fractured with columnal joints (Figure 2.5b) especially in the upper part while those at the rift floor often exhibit weathered surface.

- **Basalt (Wba & Wbb):** Basalt is basic volcanic rock found in the north-eastern part of the study area. They occur as a series of lava flow. Some are associated with scoria cones referred to as older basalts (Wbb) while some are younger mostly of fresh surface (Wba) formed between Pliocene to Recent age (Dipaola, 1970). Their texture ranges from aphaneritic to porphyritic. Petrographically, their major constituents are plagioclase feldspar, olivine and pyroxene.

- **Alluvial (Ls):** Alluvial is a volcano-sedimentary products in the area. It is generally homogeneous and made up of ash, fine sands and clay. It covers large part of the study area and sometimes occurs as thick pile.

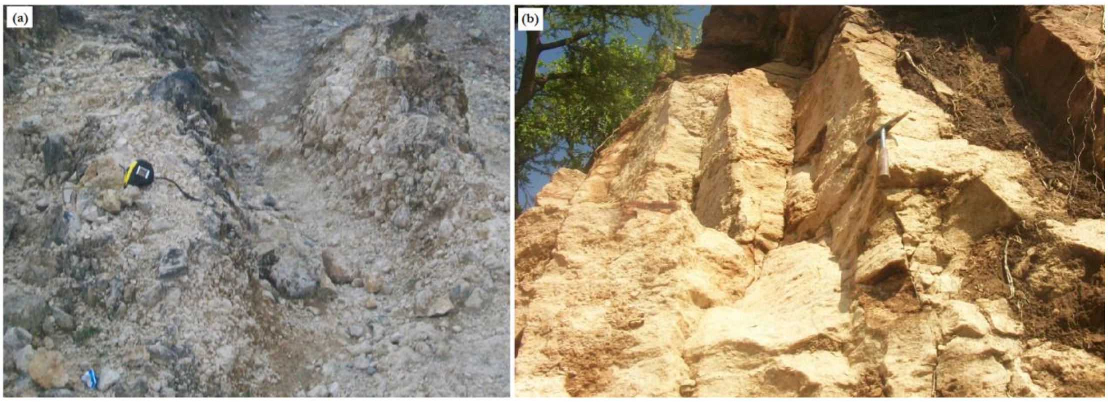

Figure 2.5: (a) Pumice pyroclastic breccias; (b) Rhyolite showing columnal joints

Tectonic and structural setting of Mount Berecha area is mainly characterized by NNW – SSE and NW-transverse normal faults. The part of Wonji Faults Belt (WFB) segment trending in NNE-SSW which affects Gademsa caldera faulting also extends to some part of Berecha area. The Berecha transverse faults intersect the NNE-SSW fault. Reconnaissance study carried out in 1987 by Ethiopian Institute of Geological Survey and Geothemica Italiana also recorded the NNW-SSE direction of faulting in Berecha area (Ayele et al., 2002).

2.4. Surficial Mineral Mapping using Shortwave Infrared Spectroscopy: Literature Review

Hydrothermal alteration in Berecha area has been poorly studied. Previous works in the central part of the Main Ethiopian Rift on geothermal resource exploration was conducted around Gademsa caldera, Tulu-Moye and Abaya which cover small part of Berecha area. Report from the geothermal resource exploration indicate presence of periodic eruptions and young eruptive centers, widespread occurrence of steaming ground and hydrothermal surface, numerous active faults and phareatic explosion crater which indicate existence of an active heat source. Study of alteration minerals in Gademsa caldera, Tulu-Moye and Abaya area reports occurrence of both acid sulphate and alkaline type of alteration, wide distribution of chalcedony deposit which could indicate deep reservoir temperature (Ayele et al., 2002). The report from the previous studies, gives hint about hydrothermal alteration activity in Berecha area, which the essence of this study.

In time past, characterization of hydrothermal minerals is done by laboratory-based analytical techniques, such as X-ray diffractrometry and optical and electron microscopy, which is convectional method, time-consuming and costly. However in recent decade, field-based short-wave infrared (SWIR) spectroscopy has been increasingly applied in mineral exploration (Yang et al., 2001). The study of hydrothermal alteration in Berecha area was carried out using shortwave infrared spectroscopy (the new technology). The approach is useful in surficial mineral mapping using spectral signatures. Spectral range of 0.4-2.5 μm of the electromagnetic spectrum show abundant information about many important earth-surface minerals. In particular, the 2.0-2.5 μm shortwave infrared (SWIR) spectral range covers spectral features of hydroxyl-bearing minerals, carbonates and sulfates, common to many geologic units and hydrothermal alteration assemblages (Goetz et al., 1985; Rowan et al., 2006).

Reflectance spectra of rocks and minerals acquired in the short-wave infrared (SWIR), from 1.3 μm to 2.5 μm offers a useful approach in alteration mapping and mineral exploration. The technique is ideal for detecting layer-silicates and carbonates, because the vibrations of the inter-atomic bonding in these minerals are active in the infrared region. The degree of crystallinity and compositional variations of minerals also can be gained by this technique. Moreover, rapid acquisition of SWIR data by the PIMA-II or ASD FieldSpec Pro enhances the production of drill logs, geological maps and the definition of alteration zones. For these reasons, this technique is widely applied in mapping mineralogical variations within a hydrothermal alteration system (Sun et al., 2001).

3. INSTRUMENTATION AND DATASETS

This chapter describes the remote sensing instrumentation and datasets applicable in this research. These include; AISA Hawk (airborne hyperspectral data), LiDAR for the digital elevation model (DEM) data, ASTER and ASD FieldSpec Pro for the acquisition of laboratory spectra.

3.1. AISA Hawk

Airborne Imaging Spectroradiometer for Applications (AISA) Hawk sensor (instrument) is a commercial hyperspectral push broom type imaging spectrometer system developed by SPECIM based in Finland (van der Meer, 2001). The flight campaign of the study area was carried out in January 2008 by NERC-ARSF (National Environmental Research Council - Airborne Research and Survey Facility) based in United Kingdom.

AISA Hawk imaging spectrometer produces hyperspectral remote sensing data in many contiguous bands in the wavelength range of electromagnetic spectrum between 390 nm to 2460 nm. The AISA Hawk records the SWIR range between 1006 nm and 2457 nm and it is accompany by AISA Eagle which covers the VIS-VNIR range between 393 and 988 nm. AISA Hawk data is used in this research work due to its SWIR region spectral coverage that is of interest in alteration mineral mapping.

The AISA Hawk data is recently acquired covering the study area of about 25 km by 10 km. The image data produced is calibrated sensor data (level 1) and not georeferenced data (level 3). This has an advantage in that level 2 products (e.g. atmospherically corrected radiances) can be generated and the data can also be georeferenced after spectral processing (NERC-ARSF, 2008). Table (3.1) shows specification of AISA Hawk.

Spectral Range	1006 - 2457 nm
Sampling Interval	6.3 nm
Spectral Band	252
Spectral Resolution	12 nm
Altitude amsl	12000 feet
Pixel size	2.5 m
IFOV	0.075 degree
Ground IFOV at 2000 m flying height	2.62 m

Table 3.1: AISA Hawk Sensor Specification

3.2. LiDAR

LiDAR (Light Detection And Ranging) is an active sensor, similar to radar, that transmits laser pulses to a target and records the time it takes for the pulse to return to the sensor receiver. This technology is currently being used for high-resolution topographic mapping by mounting a LiDAR sensor, integrated with Global Positioning System (GPS) and inertial measurement unit (IMU) technology to the bottom of aircraft and measuring the pulse return rate to determine surface elevations (NOAA, 2011). LiDAR was used to obtain the digital elevation model (DEM) of the study area by NERC-ARSF at the same time of acquiring the hyperspectral data. Table (3.2) gives the LiDAR specification applicable in this study.

Scan angle	20
Scan frequency	20
Resolution	1.24 meters
Altitude amsl	12000 feet
Illumination %	100
Shadow %	0
Cloud %	0
Data quality	10

Table 3.2: LiDAR Sensor Specification

3.3. ASTER

The Advanced Spaceborne Thermal Emission and Reflection Radiometer (ASTER) is a multispectral imaging system. It consists of 14 bands within the electromagnetic spectrum with 3 bands in the visible and near infrared (VNIR) with 15m spatial resolution, 6 bands in the short wave infrared (SWIR) with 30m spatial resolution and 5 bands in the thermal infrared (TIR) with 90m spatial resolution (SIC, 2011). The bands within the SWIR range were used in this study. ASTER image was combined with AISA Hawk data to delineate field work target areas. The ASTER image available for the study has been processed; sub-setting of the study area was however carried out as well as colour composite. Table (3.3) summarized the description of ASTER image.

Spectra Range	Bands	Spatial Resolution (m)	Swath width (km)
VNIR	1-3	15	60
SWIR	4-9	30	60
TIR	10-14	90	60

Table 3.3: Description of ASTER image

3.4. ASD FieldSpec Pro

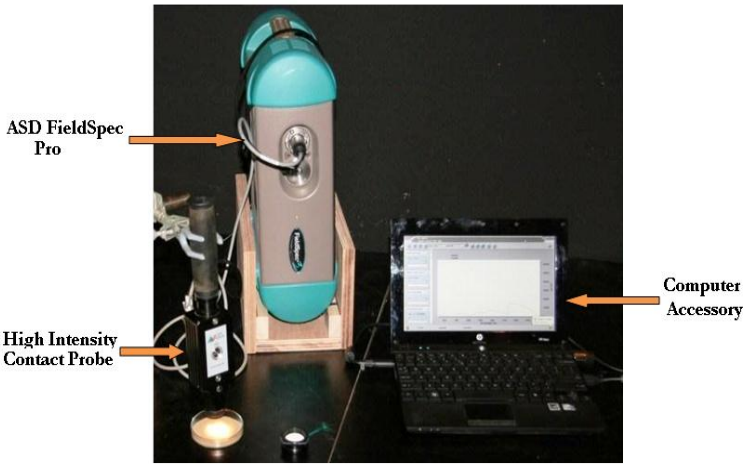

Figure 3.1: ASD FieldSpec Pro Diagram

ASD FieldSpec Pro is a full computer-controlled spectroradiometer with a spectral range of 350–2500 nm. It is designed to collect solar reflectance, radiance and irradiance measurements of materials. It has spectral resolution of 3 nm at 700 nm, 10 nm at 1400 nm and 12 nm at 2100 nm and sampling resolution of 2 nm at 1000-2500 nm and 1.4 nm at 350-1000 nm. ASD FieldSpec Pro is compact and easy to set up, thus allowing much data collection. The instrument has contact reflectance probe, which can be fixed to the fibre-optic cable to provide spectral capabilities measurement. This attachment brings the ASD FieldSpec in line with other instruments such as the PIMA SP, allowing collection of high quality reflectance spectra over a range of surfaces, with improved signal to noise ratios, thus making it ideal for spectral library creation across a range of applications, such as in geology, mining, oceanography, forestry and plant physiology etc. (Arthur, 2007). The ASD FieldSpec Pro was used to acquire laboratory spectra of rock and samples during fieldwork. Detailed and simplify specification of ASD FieldSpec Pro is found in Table (3.4) and Figure (3.1) show ASD FieldSpec Pro diagram.

Spectral Range	350-2500 nm
Sampling Interval	1.4 nm, 350-1000 nm 2 nm, 1000-2500 nm
Spectral Resolution	3 nm at 700 nm, 10 nm at 1400 nm, 12 nm at 2100 nm
Input	1.4 m fiber optic light guide
Fore Optics Field of View	8°, 18°, 25°
Additional Fore Optics	High intensity contact probe
Power Source	Mains, external Ni MH rechargeable cells, or 12 V batteries
Weight	7.2 kg

Table 3.4: Specification of ASD (Arthur, 2007)

4. METHODOLOGY

This chapter describes the methods, algorithms and techniques used in this research. The research methodology is described in three phases in order to meet the objectives of the study. The Pre-field work phase, Field work phase and Post-field work.

4.1. Pre-Field work phase

At this stage, research questions, hypothesis and suitable research approach were formulated in order to meet the objectives of the research study. Reviewing of literatures related to the topic was carried out; exploratory data analysis; visualization and preliminary pre-processing of AISA Hawk hyperspectral image integrated with ASTER image were done.

Field work targets were derived from ASTER and hyperspectral image in which image processing such as colour composite and wavelength mapping has been applied (image processing discussed in later section). ASTER image colour composite, band 1:2:3 show interesting features that assist in delineating the field target area in combination with the hyperspectral data. The result derived from the two (ASTER image and AISA Hawk data) was further combined with topographic map (that is, road and network map). Interesting target locations were finally selected as shown in Figure (4.1).

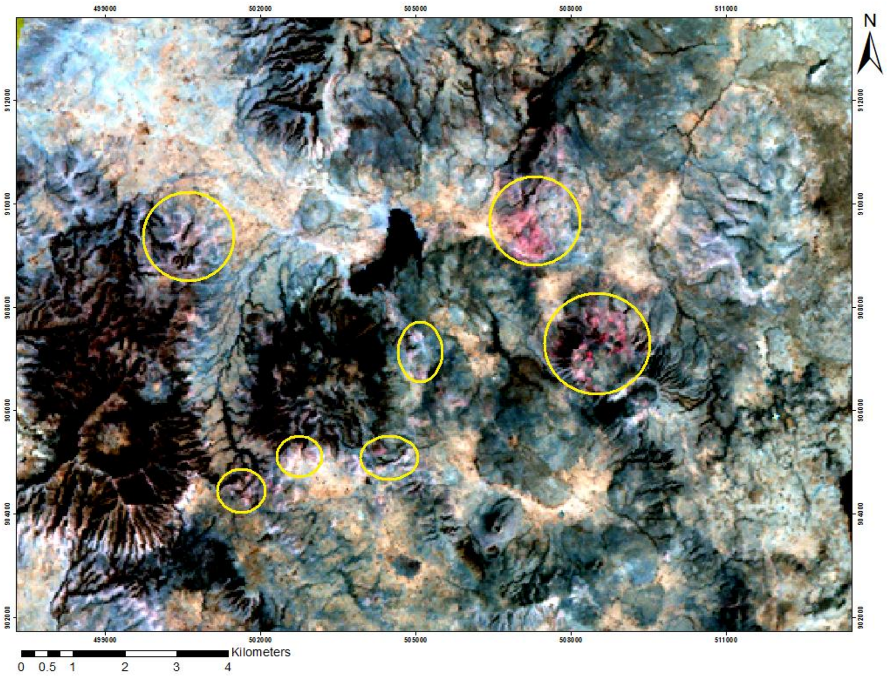

Figure 4.1: ASTER image (band 1:2:3) showing field work targets locations in yellow circle as tentative sample location obtained before field work

4.2. Field work phase

The field work phase of the study involves collection of mineral and rock samples which are related to the study, GPS data were taken as well as photographs. Eighty-three (83) sampling points (locations) were visited. Sampling was carried out initially by random collection of samples from altered part of the study area. At the later part of the field work however, detailed and systematic sampling was done along a profile section at every 50 steps (50 m intervals) in order to have variation of minerals in the study area and to avoid been bias. The detailed sampling was based on information obtained from preliminary processing (wavelength mapping) of the AISA Hawk data which show variability in colour indicating different alteration minerals. Samples were also taken from unaltered rock in order to study petrography of the rocks and to have knowledge about the geology of the alteration zones; the rocks in the area include rhyolite, trachyte, quartz, basalt etc (Appendix 01). The rocks are partly altered to clay minerals (whitish, brownish, reddish, purplish and greyish in colour). Supplementary data such as location, elevation, and geology were recorded alongside with sample collection.

Laboratory spectra of mineral and rock were acquired back at the hotel on the samples collected from the field using "ASD FieldSpec Pro" and a high intensity contact probe instrument (Arthur, 2007). Several measurements were taken per sample in order to have full information about minerals present. Measurement that could not be carried out in the field due to late collection of such samples were taken in spectroscopic laboratory in ITC (Faculty of Geo-information Science and Earth observation, University of Twente) Netherlands and some samples were re-measured to obtain multiple laboratory spectra for better interpretation. Some field photographs are shown in Figure (4.2).

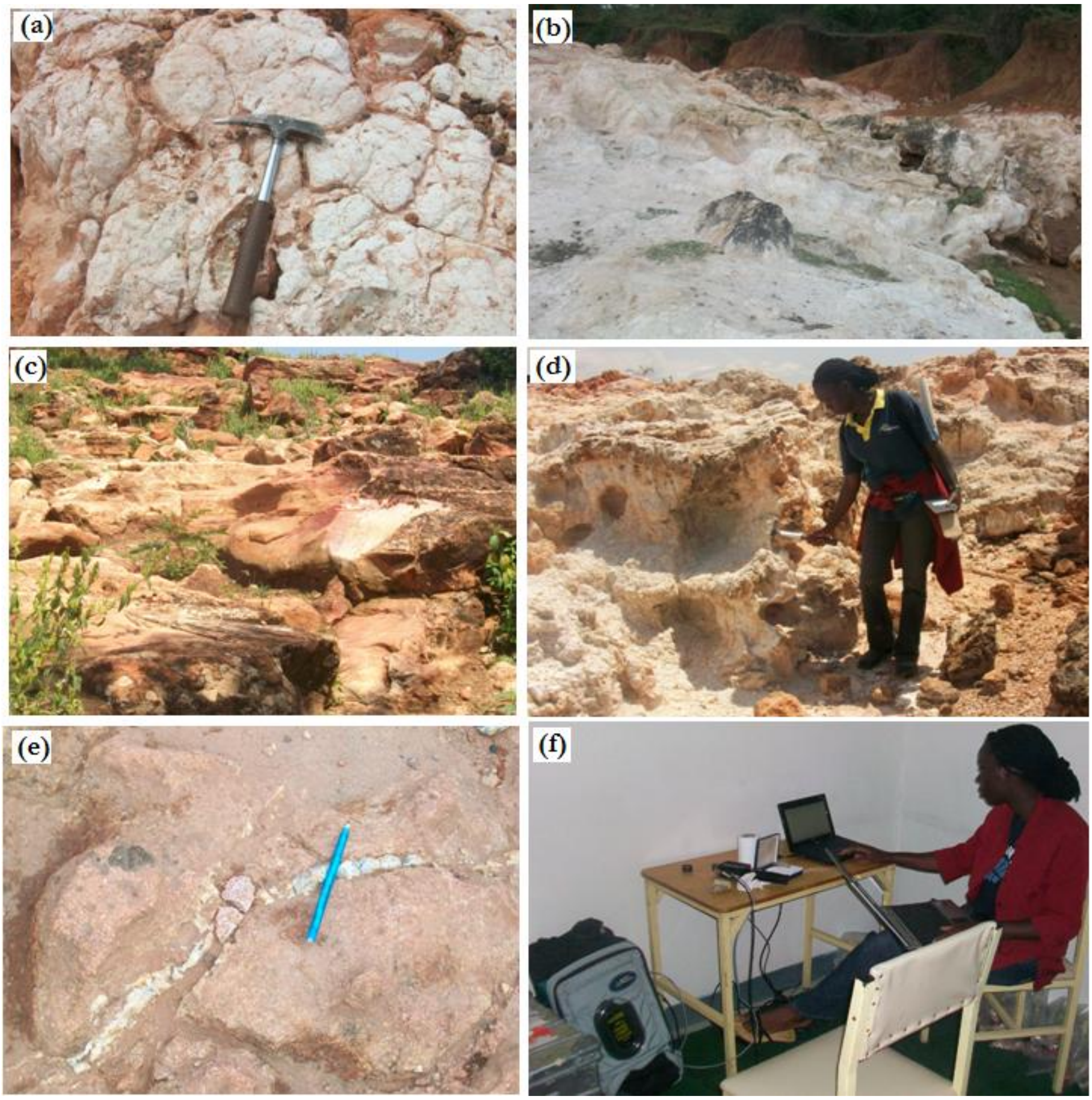

Figure 4.2: (a) Sample of clay mineral collected; (b) A location showing demarcation between altered area and alluvial lithological unit (unaltered area); (c) Rhyolite rock type becoming altered; (d) Collection of sample in the field; (e) Quartz vein- like in an altered area; (f) Reflectance spectra acquisition of minerals and rocks with the ASD in the hotel

4.3. Post - Field work phase

The Post-field work phase involves analysis of spectra acquired from samples collected during field work, pre-processing and application of mapping methods on airborne data (AISA Hawk). Finally, analysis of LiDAR-DEM data for structural mapping in order to understand the control of structure on spatial distribution of the alteration minerals in the study area.

4.3.1. Field Data Analysis

Laboratory spectra acquired from the field samples with ASD FieldSpec Pro were checked visually using software called ViewSpecPro, the spectra were converted to text format for further analysis. The converted spectra were analyzed with "The Spectral Geologist" (TSG) software (CSIRO, 2010).

4.3.1.1. Analysis with TSG

TSG is specialized software designed for spectra analysis and interpretation. It provides automated assistance in spectral interpretation via two different approaches: *The Spectral Assistant (TSA)* and the *Auxiliary matching* method. The **TSA method** uses a training library of spectra either to match the unknown project spectrum against a single mineral spectrum or to create a simulated mixture of two mineral spectra that match the project spectrum (whichever has the lowest errors). TSA has been trained using a Training Library of over 500 spectra, representing 47 "pure" minerals and 8 different non-mineral artefacts in the SWIR. The samples have been collected from many sites around the world, in an attempt to represent the diversity of samples of the same mineral. **Auxiliary matching method** is a shape matching process which matches the spectral shape of a project spectrum with those in a series of spectra in a Custom or Auxiliary library and the result with the best fit is output as the best match (CSIRO, 2010).

In this study, the first method was applied. The algorithms checks for the specific absorption features in the unknown spectra (the laboratory spectra put in) and matches it with the TSG library (reference) spectra. TSA is not perfect in mineral identification; certain degree of error is possible. Such error was noticed in the analysis where some spectra were matched as siderite which on visual inspection has no absorption feature of siderite or spectra shape of siderite. Therefore, results from TSA were vetted by visual inspection following the Spectral Interpretation Field Manual (SIFM) method (Pontual et al., 1997b) and by comparison to 2006 USGS spectral library (Clark et al., 2007). Duplicate spectra of same mineral exists in some sample, in such case, selection of one spectrum is used as representative by taking an average. While in other sample, different spectra werefound, with such, final selection is based on careful examination and thorough evaluation of the mineral spectra, TSA weight of the mineral in the sample also gives some clue to handling this. Sample number 024 is shown as an example in Table (4.1), five ASD measurements were taken on the sample and the mineral identified by TSA is shown accordingly:

Sample Number	TSA_S Mineral-1	TSA_S Weight-1	TSA_S Mineral-2	TSA_S Weight-2
AL_10_02400001	Opal	1	NULL	NULL
AL_10_02400002	Opal	0.841	Halloysite	0.159
AL_10_02400003	Opal	0.75	Kaolinite	0.25
AL_10_02400004	Opal	1	NULL	NULL
AL_10_02400005	Opal	1	NULL	NULL

Table 4.1: Table showing TSA analysis on sample 024

Final record of the minerals in this sample is done by careful examination, visual inspection and comparison of the spectra with reference library (USGS) and then recorded as:

Station No	Mineral-1	Mineral-2	Mineral-3
AL_10_024	Opal	Kaolinite	Halloysite

The final record is based on explanation given above, i.e. opal exists severally, then it is consider as dominant mineral and average of it is taken as mineral-1, kaolinite is recorded as mineral-2 and halloysite as mineral-3 based on their TSA weight.

4.3.1.2. Analysis with Spectral Interpretation Field Manual

In Spectral Interpretation Field Manual, certain principles were followed in order to better analyze and interpret mineral spectra in the study area. It is established that minerals have characteristics spectral signatures or pattern; however it could be burdensome to identify an unknown spectrum by comparison with spectra in a large spectral library (Pontual et al., 1997b). Therefore, following guidelines were put in place for mineral spectral interpretation;

- That most minerals have a characteristic spectrum between 1300-2500 nm
- That most minerals have major diagnostic absorption feature between 1300-2500 nm
- That most minerals can be grouped spectrally according to wavelength position of the deepest absorption feature between 1300-2500 nm.

These precepts were applied during the analysis of the field data, putting also into consideration other parameters like depth of absorption feature, asymmetric of the absorption features and spectra shape. Most of the minerals were identified using the wavelength position of the deepest absorption feature. They occur within characteristic wavelength bands of the spectrum as shown in Figure (4.3).

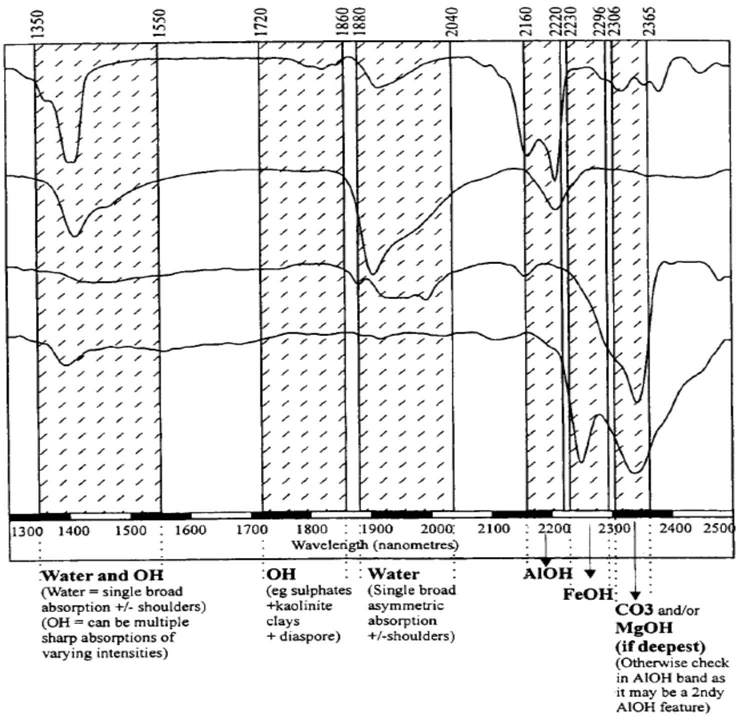

Figure 4.3: Major spectral absorption band in SWIR after (Pontual et al., 1997b)

4.3.1.3. Comparison with USGS Library

Spectra obtained from the above analysis were furthered checked and compared with USGS spectral library using ENVI software. Main absorption features of spectra from samples analyzed were critically checked and studied in order to compare their absorption wavelength to that of the spectral library. Diagnostic absorption feature (i.e. OH, H_2O, Al-OH, Fe-OH, Mg-OH and carbonate absorption features) of most of the mineral spectra analyzed occur at same (approximately same) wavelength position in comparison with the USGS spectral library. The similarity in their shape was also observed with this method. The result is discussed in next chapter. The final minerals are classified as mineral-1, mineral-2 and mineral-3 based on thorough application of the above mentioned methods (Appendix 02).

4.3.2. Pre-Processing of AISA Hawk Data

In this section an overview of the methods used in the pre-processing of the AISA Hawk data is presented. The AISA Hawk data used in this research is newly obtained, thus much pre-processing steps were involved. During the processing, a wavelength shift in the 2.2 μm absorption features of kaolinite from 2.208 μm to 2.217 μm became apparent in the data. This is related to an inadequate wavelength calibration of the Hawk sensor. The shift at other wavelengths than 2.2 μm is unknown and cannot be corrected for. Due to the poor wavelength calibration no rigorous atmospheric correction by modeling was attempted. Instead a simple log residual correction was used. A flow diagram which summarizes various pre-processing and mapping methods applied to the AISA Hawk data is shown in Figure (4.4).

4.3.2.1. Spatial Subset

Spatial sub-setting of the AISA Hawk flightlines was done in order to reduce the image size to the study extent and also to avoid memory problem. This process removed the beginning and end of each flightline which show distortion as a result of aircraft movement (unbalanced position of the aircraft).

4.3.2.2. Fix Nodata

Fix Nodata is an image pre-processing method used to convert unwanted values (i.e. no data values) or erroneous values to not a number (NaN). The advantage of this is that NaN's are not taken into consideration in statistics and when further processing operations are perform.

4.3.2.3. Destriping

Destriping is a way of removing stripping patterns or effect in an image. The AISA Hawk sensor has clear vertical striping as a result of poor radiometric calibration. Destriping approach adjust the image column brightness. Destriping was done by division and no smoothing was performed.

4.3.2.4. Median Filtering

Median Filtering was performed on the AISA Hawk image for noise reduction and to replace drop out lines. The algorithm used in medium filtering is 3-dimension median filter which uses the central pixel, the 4 spatial neighbours and the 2 spectral neighbours.

4.3.2.5. Spectral Subset

The bands 154 – 230 of wavelength 1.971 - 2451 μm were selected to avoid noisy bands around water features (1.400 μm and 1.900 μm), band 231 with noise and bands without much information on alteration mineralogy (shorter than 1.950 μm) were neglected in order to generate effect result.

4.3.2.6. Log Residuals Normalization

Log Residuals processing is a fast, simple, alternative way to rigorous atmospheric correction. The purpose of the algorithm is to remove albedo effects (caused by topography or shadow etc.) and to remove atmospheric effects (Bakker, 2010). It is a two-step normalization method in which the spectra of the pixel are normalized first and then pixels are divided by the mean spectrum of the whole image. The Log Residuals was applied after the spectra subset in which the noisy bands have been removed in order to obtain useful result. To make the mean spectrum of the entire image less sensitive to noise, the algorithms uses a statistical method to determine the spectrum. The statistical least upper bound (SLUB) spectrum is determined as follows (per channel);

$$SLUB_i = \min((scene\_avg_i + N * scene\_stdev_i), scene\_max_i)$$

Where;

- $scene\_avg_i$ is the scene's average value for band i.
- $scene\_stdev_i$ is the scene's standard deviation for band i.
- $scene\_max_i$ is the scene's maximum value for channel i.
- N is the user-supplied factor, 3.0 standard deviation is used for the process.

4.3.2.7. Geometric Correction

Imaging spectrometer data acquired from airborne imaging system usually suffer spatial distortions due to the aircraft movements and the ruggedness of the terrain. Thus, geometric correction is done to produce a geocorrected image. The software use for geometric correction in this research study is called **azgcorr,** an airborne remote sensing hyperspectral direct georeferencing package developed and distributed by NERC-ARSF with the data. The method used in **azgcorr** geocorrection procedures was initially called "parametric geocorrection" but of recent times has adopted the title "direct georeferencing". This indicates that, the aircraft precise 3D navigation (position, pitch, roll and heading) is used for the geocorrection, without the need for any ground control (Azimuth, 2005).

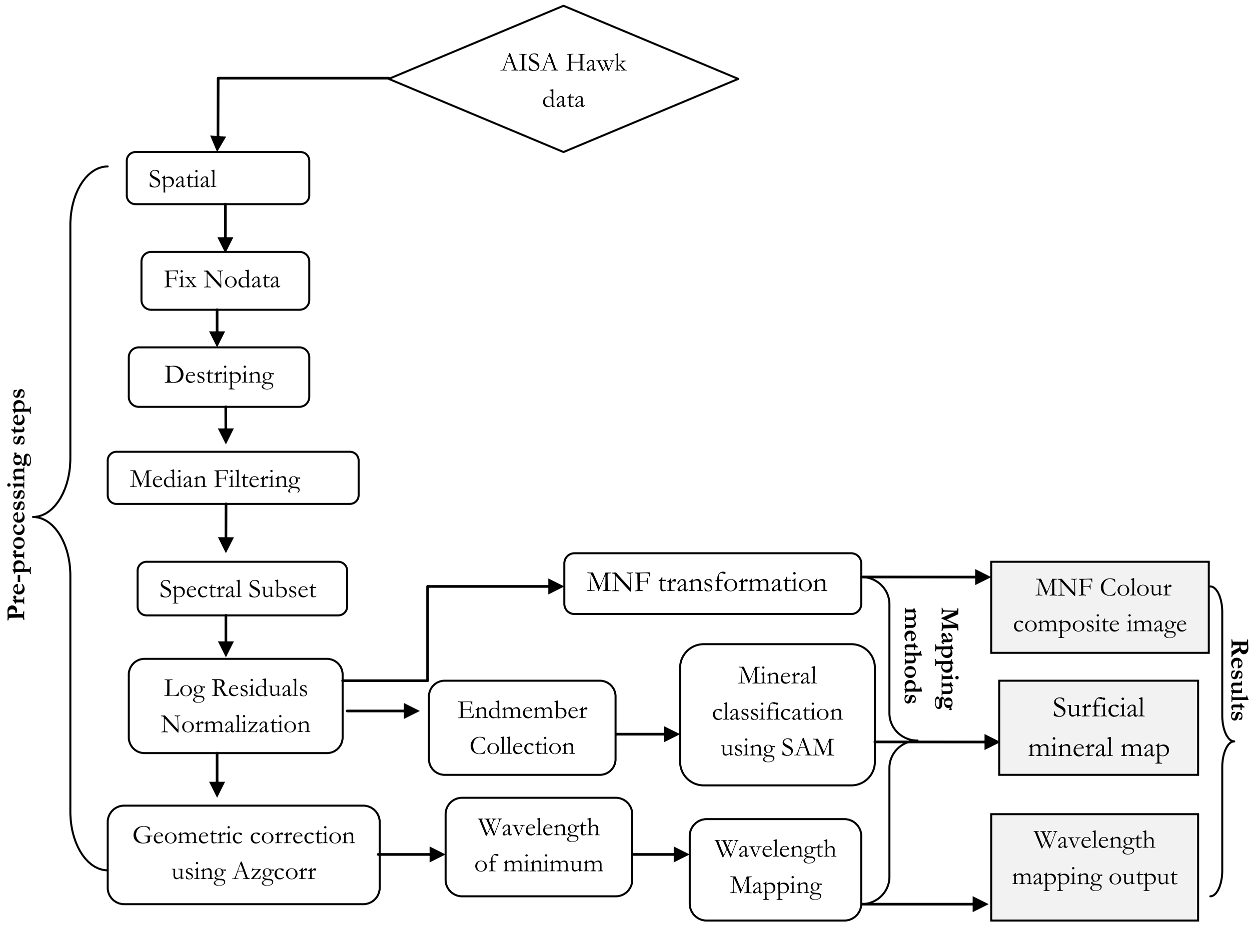

Figure 4.4: Flowchart of pre-processing steps and mapping methods of AISA Hawk data

4.3.3. Mineral Mapping Methods using Hyperspectral Image

Different mapping techniques were applied to map out the alteration minerals in the study area. Wavelength of Minimum and Wavelength Mapping were applied in PyEnvi software while MNF transformation, endmember collection and Spectral Angle Mapper (SAM) classification were carried out in ENVI 4.7.

4.3.3.1. Wavelength of Minimum

Wavelength of Minimum is technique that determines the wavelength of the smallest value of the spectrum. In other word, the algorithm check for location in the spectrum where the most pronounced absorption feature happens and models its depth and width. This technique makes use of Absorption-band parameters such as the position, depth, width, and asymmetry feature. The algorithm works by input wavelength range of one choice depending on the spectrum region that is of interest. In this study, SWIR region of the spectrum is analyzed due to important information that can be generated from it, the wavelength used ranges from 2.0 μm to 2.4 μm. The technique generates or produces output image of several bands, each band having information useful in interpretation and identification of alteration minerals (Bakker, 2010). The output bands useful in this study which serves as input in processing wavelength Mapping are: *interpolated minimum wavelength* (i.e. wavelength of the minimum of the interpolated parabola) and *interpolated depth* (i.e. depth of the parabola at the minimum).

4.3.3.2. Wavelength Mapping

Wavelength mapping is a simple technique that makes use of output from wavelength of minimum to produce a colour map. This is done by making use of colour table and hue saturation value (HSV) on the interpolated wavelength of minimum, merging it with the interpolated depth of the feature. The wavelength range used for this process varies between 2.204 µm and 2.439 µm where most of the alteration minerals have their deepest absorption features and the depth use is 0.0 - 0.2. This technique is very useful in mineral interpretation and usually generates mineral map with different colour for different wavelength absorption feature, it is mostly useful in areas with alteration zones (Bakker, 2010). The image generated was analyzed further in ENVI software to link the wavelength position of deepest absorption feature to their mineral match. This is done by carefully examining different pixels and obtain wavelength value of deepest absorption feature using guide from spectral interpretation field manual and comparison with USGS library, minerals related to each colour were identified.

4.3.3.3. Minimum Noise Fraction Transformation

Minimum Noise Fraction (MNF) transformation is a principle similar to Principal Components (PC) transformation that transforms images to uncorrelated components. The images are sorted on the basis of their noise statistics from low to high noise component. Like Principal Components transformation, the MNF transformation can be used to determine the inherent dimensionality of image data, to segregate noise in the data and to reduce the computational requirements for subsequent processing. MNF transformation is a two-step transformation; the first step of the transformation removes band-to-band correlations and rescales the noise in the data to have unit variance. The second step is a standard Principal Components transformation of the normalized data. (Kruse, 1995). The MNF transformation was performed on the log residuals image. Not a number (NaN) values were masked out from the input image before the MNF transformation process.

4.3.3.4. Endmember Collection

Analysis of the image endmember was done by using the laboratory spectra acquired from field data as guide in picking image pixels with pure endmember spectra from the log residuals output. Field location points with the identified mineral were checked for on the log residual image (i.e. where pure kaolinite spectrum was found in the field data, same position was searched for in the image and then selected as kaolinite endmember, this step was applicable to all selected endmembers). The image derived endmembers were compared with USGS spectra library to check their similarity in absorption features and shape.

4.3.3.5. Spectral Angle Mapper Classification

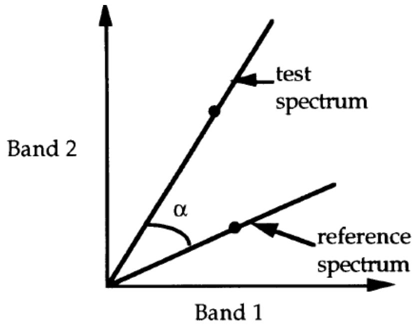

Figure 4.5: Two dimensional illustration on the concept of Spectra Angle Mapper algorithm (Kruse et al., 1993)

The Spectral Angle Mapper is a tool that permits rapid mapping of the spectra similarity of image spectra to reference spectra. The algorithm determines the spectral similarity between test reflectance spectrum and reference reflectance spectrum by calculating the "angle" between the two spectra, treating them as vectors in a space with dimensionality equal to the number of bands (Figure 4.5); assuming that the data is correctly calibrated to apparent reflectance with dark current path and radiance removed (Kruse et al., 1993). The image derived endmembers serves as the training set (input) in Spectral Angle Mapper (SAM) classification. Threshold angle of 0.10 radians was used in the classification to show best SAM match at each pixel between each spectrum in the image and the reference spectrum (see result in section 5.2.4).

4.3.4. Kaolinite Crystallinity

Preliminary spectral analysis showed that kaolinite strongly dominates other alteration minerals in the study area. In an attempt to further differentiate zones within large kaolinite altered area, kaolinite crystallinity was determined. Crystallinity literally means the degree of structure order in a solid. Thus, in the context of kaolinite crystallinity in this study, it refers to analysis of structural order of kaolinite spectra which should give more insight about the environment we are dealing with apart from been able to differentiate zones within large kaolinite altered area. Kaolinite crystallinity in this study was analyzed based on the shape and wavelength spacing of the Al-OH band doublets absorption feature. This is described using two different methods; *Slope parameter* and *Kaolinite Crystallinity Index*.

4.3.4.1. Slope Parameter

Kaolinite crystallinity can be described in terms of two values proportional to the gradient or slope of the spectrum in the 2160-2180 nm region. These values are referred to as slope '2160' and slope '2180' parameter. *Slope '2160' parameter* is calculated as a ratio at 2160 nm over 2177 nm; while *Slope '2180' parameter* is calculated as a ratio at 2184 nm over 2190 nm. Both calculation is performed on a hull quotient corrected spectrum (Pontual et al., 1997b). The slope parameter was applied using the guide in Table (4.2) below.

Group	Slope 2160	Slope 2180	Crystallinity type
K1	> 1.02	< 1.01 and > 1.00	Very poor
K2	> 1.02	< 1.00	Very poor
K3	> 1.00 and < 1.03	> 0.99 and < 1.02	Poorly crystalline
K4a	< 1.00	> 1.01 (often > 1.02)	Moderately-highly crystalline
K4b	< 1.00 (often > 1.02)	> 1.01 (often > 1.02)	Very highly crystalline

Table 4.2: Slope parameter guide for kaolinite crystallinity analysis

4.3.4.2. Kaolinite Crystallinity Index (KCI)

This method combine the two slopes (2160 slope and 2180 slope) mentioned above into one parameter using the formula:

KCI = (2180 slope – (2160 slope – 2180 slope)) *where KCI is kaolinite crystallinity Index*

The KCI increases in value with increasing kaolinite crystallinity and has advantage over the slope parameters because it can easily being represented as a histogram or line profile (Pontual et al., 1997a). The result (values) obtained for the kaolinite crystallinity is found in (Appendix 03) and the interpretation is discussed in next chapter.

4.4. LiDAR-DEM Data: Structural Analysis.

LiDAR-DEM data was analyzed in order to map out the structure in the study area. Digital elevation model (DEM) reveals the surface expression of the earth geomorphology and it's useful in delineating structural information of the earth surface. Bretar and Chehata (2010) described digital elevation model as representation of the earth topography. LiDAR-DEM was used in conjunction with Hawk data to identify lineaments (faults and fractures) and other interesting features in the study area in order to understand the control of structure on mineral distribution. The LiDAR-DEM is high resolution data and does not require much processing. However, some enhancement was carried out for better interpretation. Hill-shade of the LiDAR-DEM was processed in ARCGIS and this was further stretched using standard deviation of 2.0. The datasets was stretched with different elevation values to highlight difference in the topography and structural features in the study area. Combination of the hill-shading image and the DEM data assist in identifying the structural features in the area.

4.5. Generation of 3D Model

Three-dimensional model of some of the output data was generated using Arcscene software in order to see things in 3-D view so as to obtain more interpretation on hydrothermal alteration system of the study area. The surficial mineral map obtained from SAM classification algorithm was draped on the DEM and 30% transparency hill-shaded DEM was also applied. The DEM data serves as the base surface while mineral map and structural map were draped on it. The raster surface resolution of the input datasets was changed from 128 x 128 to 30 x 30 in order to generate good output result. Vertical exaggeration of the DEM used is 5 (vertical exaggeration of DEM: x5)

5. RESULTS AND DISCUSSION

This chapter presents the results obtained from the analysis of field data, AISA Hawk hyperspectral data and LiDAR-DEM data using the methods described in chapter 4.

5.1. Field Data

Analysis of the field data (mineral and rock spectra) is based on interpretation from TSG and spectral interpretation field manual as well as comparison with USGS spectral library. Result of the method applied show the presence of several SWIR-active alteration minerals which include: Kaolinite and Halloysite (Kandite group minerals), Montmorillonite and Nontronite (Smectite group mineral), Opal, Calcite, K-alunite, Palygorskite, MgChlorite, Zoisite, Illite and mixture of these minerals. Some of the samples have pure spectra of the mineral identified (e.g. kaolinite, opal etc); these are discussed in later section with their diagnostic absorption features. Others however occur as mixture with other mineral without pure spectra to described their spectral features (these include Palygorskite, MgChlorite, Zoisite, Illite). Variation in the distribution of these minerals was observed.

5.1.1. Identified Minerals and their Diagnostic Absorption Features

This section describes different alteration minerals identified in the area after interpretation with spectral interpretation field manual and comparison with USGS spectral library.

5.1.1.1. Kandite group minerals

Kaolinite and halloysite are the common minerals that belong to kandite group in the alteration system of the study area. These minerals are very similar and not easy to differentiate because they have similar spectral shape and absorption features and they often occur together as a mixture in samples. However few spectra of pure halloysite occur in the samples analyzed to differentiate it from kaolinite.

- **Kaolinite**

Kaolinite spectra identified in the area have major characteristic kaolinite absorption features: hydroxyl (OH) stretching doublet around 1.400 μm and 1.412 μm, water (H_20) absorption feature 1.913 μm and the AL-OH diagnostic double absorption feature at 2.164 μm and 2.208 μm (Figure 5.1a). Moderate and high kaolinite crystallinity was identified in the area based on the shape and wavelength spacing of the Al-OH band doublets. Kaolinite crystallinity of the area is discussed in subsequent section.

- **Halloysite**

Halloysite is another mineral that belong to kandite group of clay mineral. Halloysite occur mostly as mixed spectra in the alteration system of the area. Hydroxyl doublet absorption feature occur around 1.392 μm and 1.412 μm and diagnostic double absorption feature for kandite minerals at 2.167 μm and 2.206 μm, this is similar to that of kaolinite but it is weaker or not well defined (Figure 5.1a)

5.1.1.2. Opal

Opal is a low temperature mineral that form from silica-bearing waters (Bishop et al., 2001) and next in abundance to the kandite mineral group. It occurs in the study area mostly as a fissure filling in rocks. It resembles chalcedony in appearance but less dense and less hard. Hydroxyl and deep water absorption features occurs at 1.412 μm and 1.913 μm respectively. Diagnostic absorption feature at 2.212 μm (Figure 5.1b).

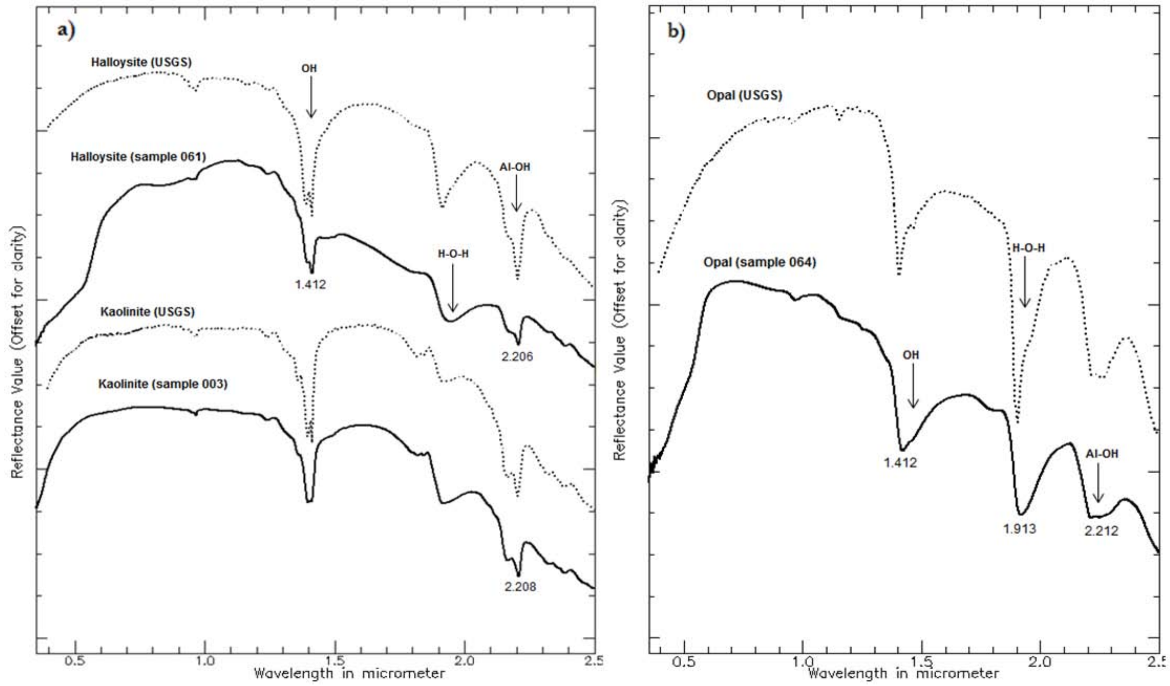

Figure 5.1: Laboratory spectra of minerals compared with USGS Library spectra

5.1.1.3. Smectite group minerals

Apart from the Kandite group, other clay minerals are present in the samples analyzed by the laboratory spectroscopy. These include montmorillonite and nontronite which belong to the smectite group.

- **Montmorillonite**

In montmorillonite spectra, sharp minima and asymmetric shape of water absorptions occur at 1.417 μm and 1.914 μm in its representative sample (Figure 5.2a). Broad intense diagnostic absorption feature is present at 2.208 μm wavelength. This feature is caused by a combination tone involving the Al-OH bending fundamental and is so particularly of clays containing aluminum (Hunt, 1979).

- **Nontronite**

Nontronite is the Fe-endmember of montmorillonite (Pontual et al., 1997b). Deep water absorption feature is present and this is similar to that of montmorillonite at wavelength 1.418 μm and 1.914 μm. Fe-OH diagnostic absorption feature occur around at 2.296 μm (Figure 5.2a).

5.1.1.4. K-alunite

Apart from the minerals mentioned above, K-alunite and calcite spectra also exist in the analyzed samples although in few occasion. K-alunite spectra have major characteristic alunite absorption features: hydroxyl (OH) stretching doublet around 1.431 μm and 1.476 μm, diagnostic absorption feature 1.763 μm and the Al-OH diagnostic double absorption feature at 2.174 - 2.208 μm and 2.323 μm (Figure 5.2b).

5.1.1.5. Calcite

Diagnostic carbonate absorption occurs at wavelength 2.340 μm; weaker carbonate absorptions are not present which is likely due to mixed spectra and this is probably replaced by water absorption at 1.418 μm and 1.914 μm wavelength (Figure 5.2b).

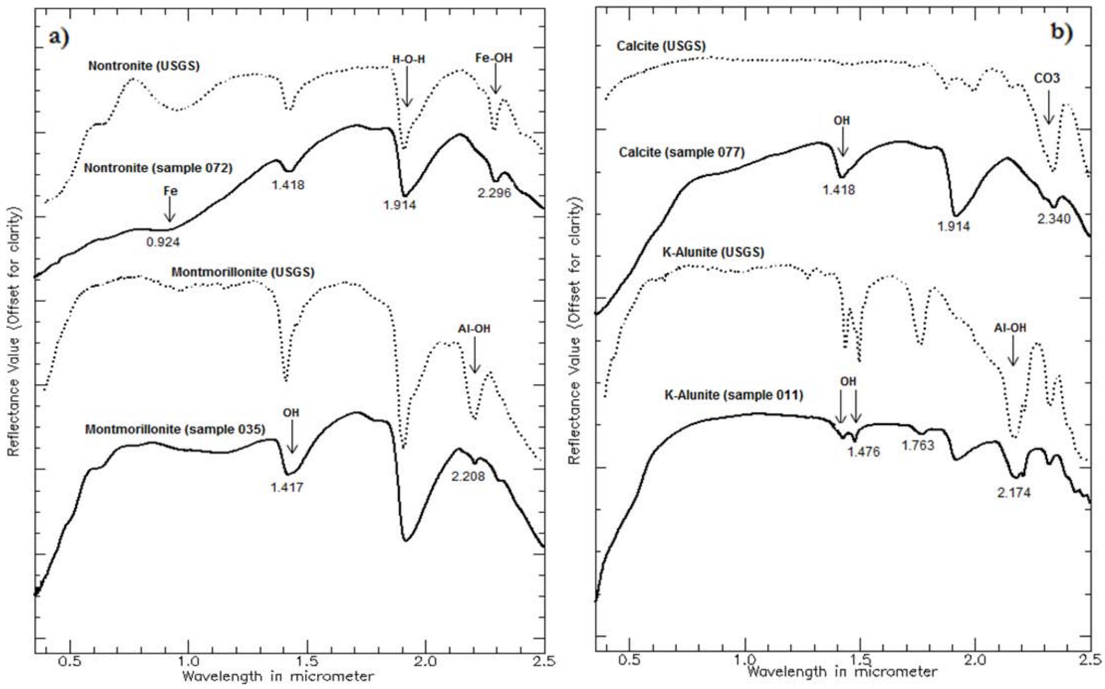

Figure 5.2: Laboratory spectra of minerals compared with USGS Library spectra

As stated above, minerals like Palygorskite, MgChlorite, Zoisite, and Illite occur as mixture with other minerals in the samples analyzed and no pure spectra to describe their features. Minerals like quartz and pyrite which have no absorption feature in shortwave infrared were also identified in the study area. The main minerals studied in the area and their diagnostic absorption feature is in Table (5.1) below.

Absorption features (μm)	Kaolinite (Sample 003)	Halloysite (Sample 061)	Opal (Sample 065)	Montmorillonite (Sample 035)	Nontronite (Sample 072)	K-alunite (Sample 011)	Calcite (Sample 077)
OH	1.400 1.412	1.392 1.412	------- 1.412	------- 1.417	------- 1.418	1.431 1.476 1.763	------- 1.418
Al-OH	2.164 2.208	2.167 2.206	------- 2.212	-------- 2.208	--------	2.174 2.208	------- -------
Fe-OH	------	-------	-------	--------	2.296	-------	-------
CO_3	-------	-------	-------	--------	-------	-------	2.340

Table 5.1: Mineral studied and their diagnostic absorption features

Some minerals like kandite and the smectite group were identified with their diagnostic absorption features using the methods described in chapter 4 (i.e. TSG, SIFM and comparison with USGS library spectra), these mineral are reliable. Some mineral match from TSA is however not too reliable because they have no pure spectra to identify their absorption features and no other evidence to prove their existence in the study area, example of such is Zoisite. Minerals like MgChlorite has no pure spectra to define its absorption features but spectra measurement from drill core show certain occurrence of chlorite, so more information was available to confirm presence of chlorite in the study area as analyzed by TSA. Different minerals were identified in some samples due to several spectra measurements taken. In most cases, the same mineral persist if it is the dominating one as found in most samples with kaolinite, (only one mineral is therefore recorded for such sample as representative mineral) while in some cases different minerals are identified and they are recorded as mineral-1, mineral-2 and mineral-3 using the methodology described in section (4.3.1.1). Detail of minerals identified from the field data is in Appendix (02).

5.1.2. Distribution of Alteration Minerals

Alteration minerals are unevenly distributed over the study area. Kaolinite dominates other alteration minerals and covers larger part of the area. It exists as pure spectra in some cases and as mixed spectra with other minerals in most cases. Next to kaolinite, opal is also abundant occurring mostly in the southern part of the study area and also on the ridge of the volcano (Figure 5.3a and 5.3b). Smectite group (montmorillonite and nontronite) occur sparsely within the study area. Calcite and K-alunite occur in few samples analyzed, while Palygorskite, MgChlorite, Zoisite and illite occurs as mixture with other minerals and are poorly distributed in the area. Figure (5.3) show an overview of the mineral distribution in the area using field observation points overlay on geology map of the study area. Major part of the alteration is associated with the Pleistocene - Holocene rhyolite felsic rock and some occurring on pumice pyroclastic deposits and on trachyte unit with fewer occurrence in the volcano- sedimentary lithological units. The result from mineral classification of the image also show that some alteration occur in the basaltic lithological unit. This infers that alteration in the study area is associated with bimodal (rhyolite and basalt) volcanic rocks.

Profile Section: Detailed study was observed along a profile section of the study area (stated in field work phase section in chapter 4). From the profile section, pattern of mineral occurrence was shown better (Figure 5.3b). Minerals with similar composition often occur together as found in the case of kaolinite and halloysite while minerals with different composition are not often seen together (e.g. montmorillonite and nontronite, nontronite is Fe rich). Kaolinite and halloysite dominate the top of the crater while opal and montmorillonite are found along the ridge. Mineral-1 indicates the most occurring mineral in a sample while mineral-2 is the next mineral abundance and mineral-3 appear when there are up to three minerals in the sample. Some samples have just a mineral in the sample analyzed as seen in kaolinite in Figure (5.3b), while in some cases two or three minerals are found. Minerals analyzed in the detailed area are shown graphically in (Figure 5.4) for clarity. From the graphical illustration, kaolinite and halloysite are clearly seen occurring together at the middle of the section, opal montmorillonite and a sample with calcite and k-alunite at the edges.

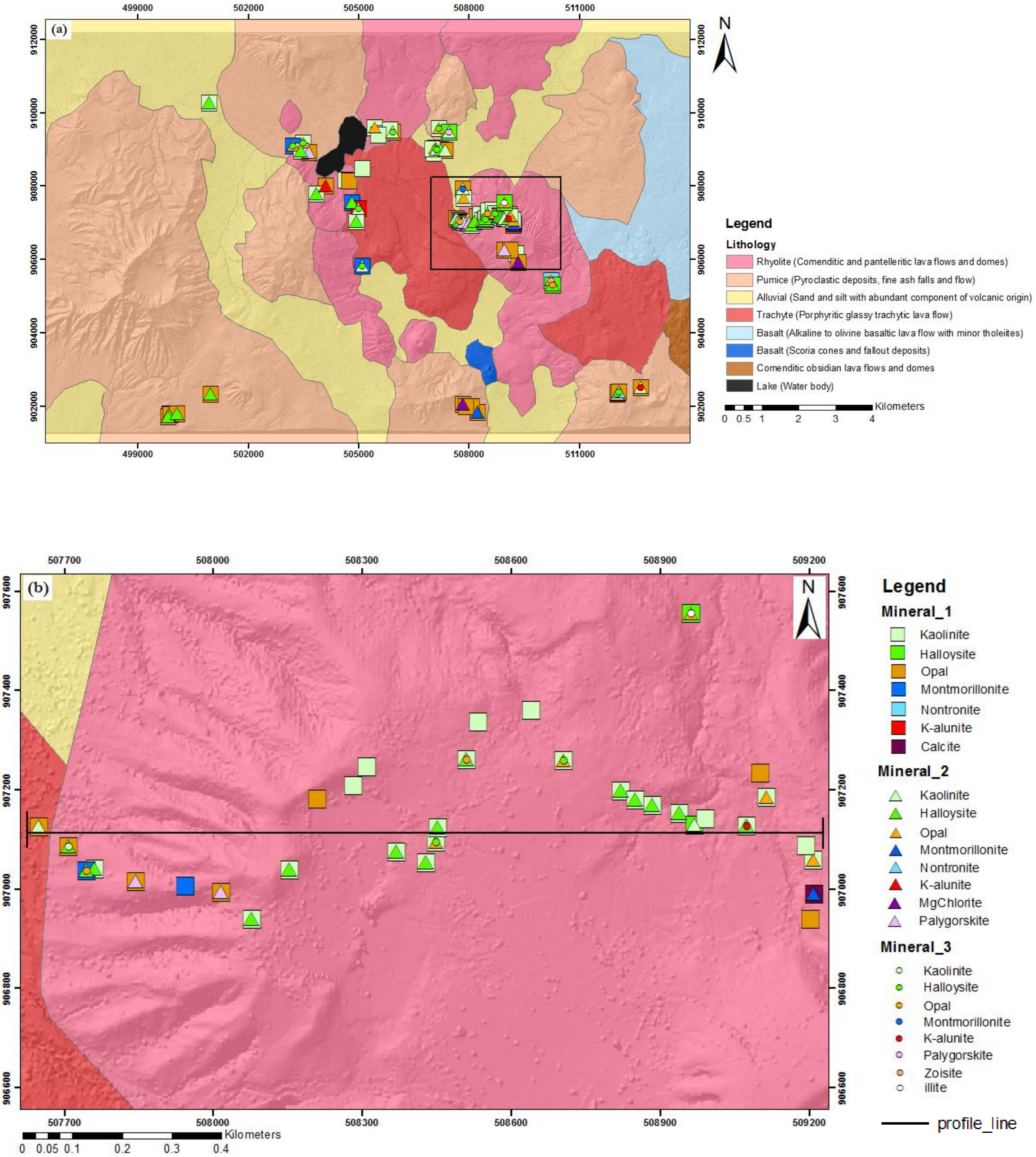

Figure 5.3: (a) Mineral distribution in the study area overlay on Geology map;
(b) Profile section of part of the area in black box (area on top of crater)

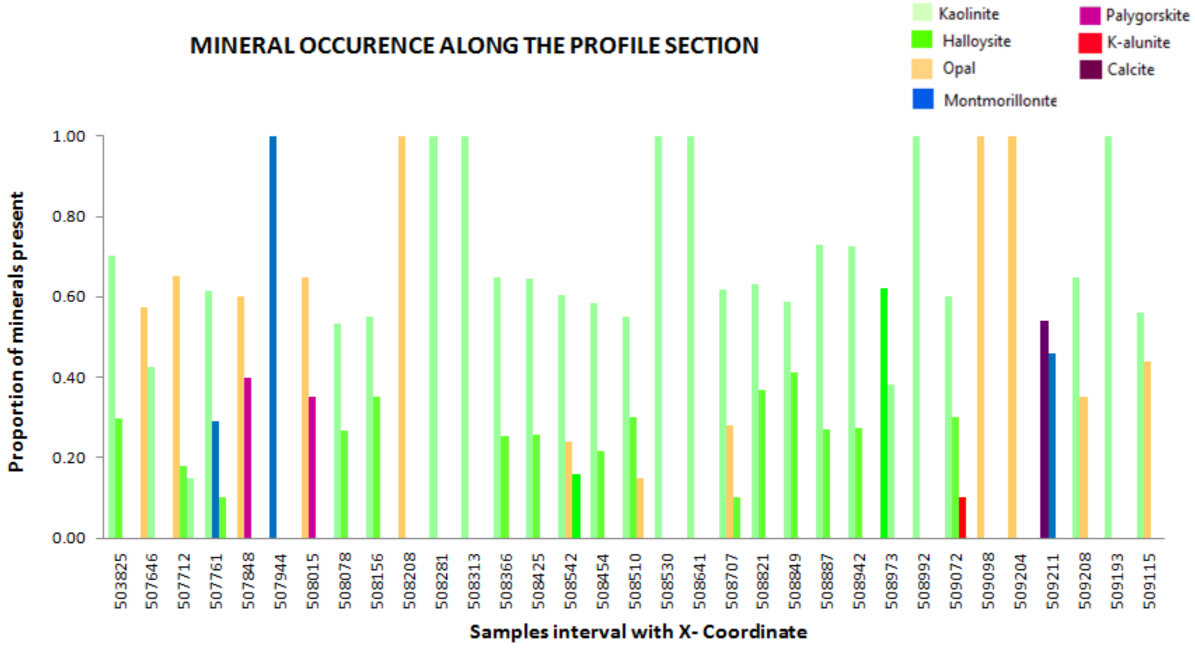

Figure 5.4: Graphical illustration of mineral occurrence along the profile section

5.1.3. Kaolinite Crystallinity Result from Field Data

The results obtained from analysis of kaolinite crystallinity using both methods described in chapter four shows that the area has moderate - high kaolinite crystallinity. Evaluation of result from slope parameter (i.e. slope 2160 and slope 2180) shows that the kaolinite in the area falls within the moderate to high crystallinity. The increase order of the crystallinity was determined using the second method, kaolinite crystallinity index (KCI), the result from this method show some variation in the kaolinite crystallinity over the study area. The result of KCI is plotted on the geology map to show if there is pattern in kaolinite crystallinity over the area and variation in their values (Figure 5.5). Lowest value of KCI is 1.011 and the highest value is 1.120 (all in moderate-high kaolinite crystallinity group).

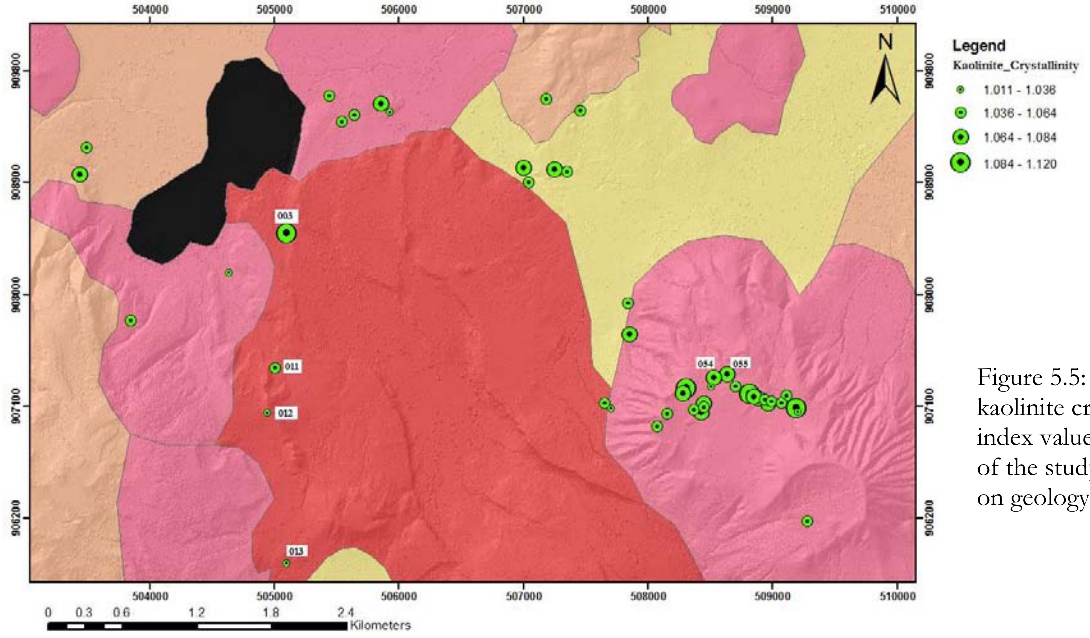

Figure 5.5: Variation in kaolinite crystallinity index value in a subset of the study area overlay on geology map

From the plot, no pattern was observed in the kaolinite crystallinity in the area with the field data, (the image however show some pattern, detail in image section). The high and the moderately crystalline kaolinite are scattered over the study area (see Figure 5.5). Figure (5.6) shows spectra structure (shape) of few samples indicated with their sample numbers in the map above, the difference in high and moderately crystalline kaolinite is highlighted in their spectra shape (structure) which is related to the kaolinite crystallinity spectra guide from spectral interpretation field manual. Generally, high kaolinite crystallinity could indicates formation of kaolinite under acidic condition or lateritic weathering (Pontual et al., 1997a; Yang et al., 1999). At Berecha area however, hydrothermal alteration is the most likely origin for the kaolinite, due to its association with other high-temperature alteration minerals (halloysite and some alunite) and the absence of deep weathering. In other words, high kaolinite crystallinity indicates high temperature formation, hence hydrothermally formed kaolinite.

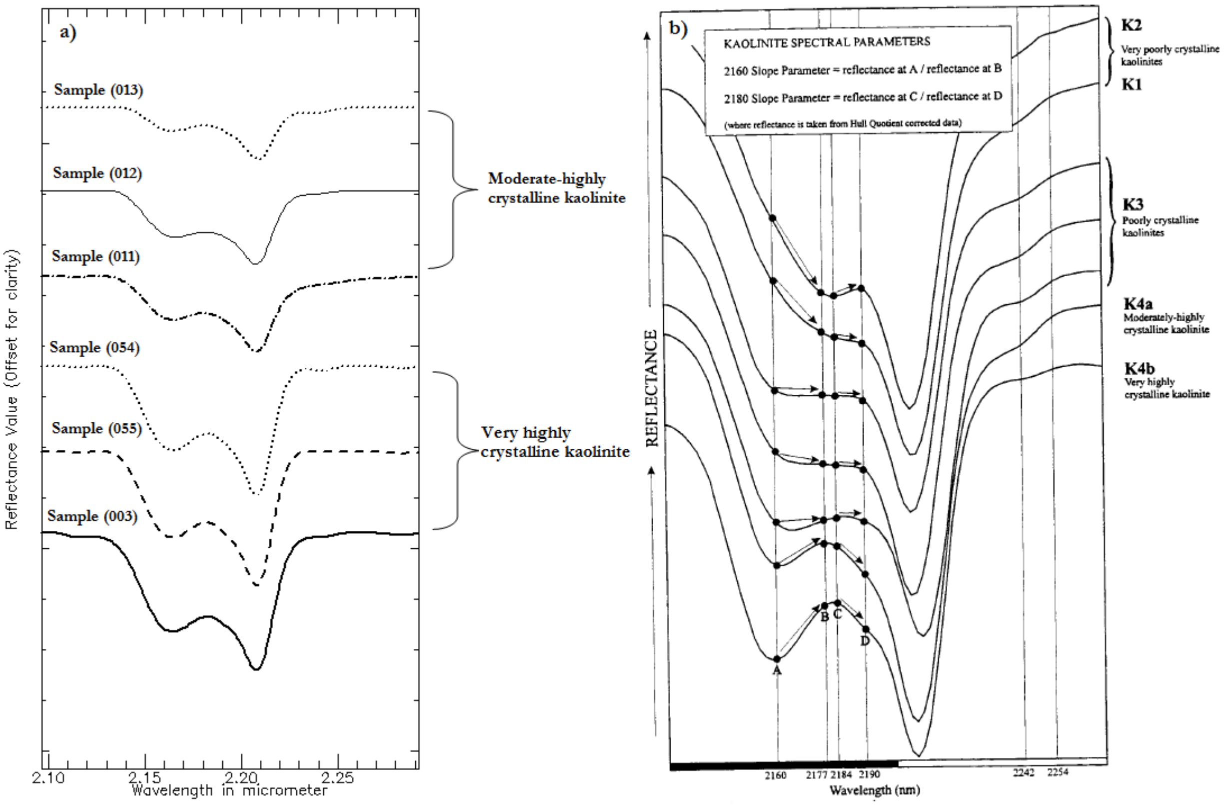

Figure 5.6: (a) Some kaolinite spectra from analyzed samples showing differences in kaolinite crystallinity (b) Kaolinite crystallinity spectra shape and parameter guide after (Pontual et al., 1997a)

5.2. AISA Hawk Data

The results derived from the airborne image (AISA Hawk data) are discussed in this section. The image gives an overview of alteration mineral distribution in the study area in comparison to field data sampling points.

5.2.1. Wavelength Mapping

Wavelength mapping is a unique tool that shows overview of alteration pattern in the area. The map obtained from merging of the interpolated wavelength of minimum with the interpolated depth of the feature in this algorithm pointed out which absorption features is dominating each pixel. The resulting map show image with different colour symbolizing various absorption feature wavelengths, each colour show degree of saturation at different absorption depth (Figure 5.7a and 5.7b).

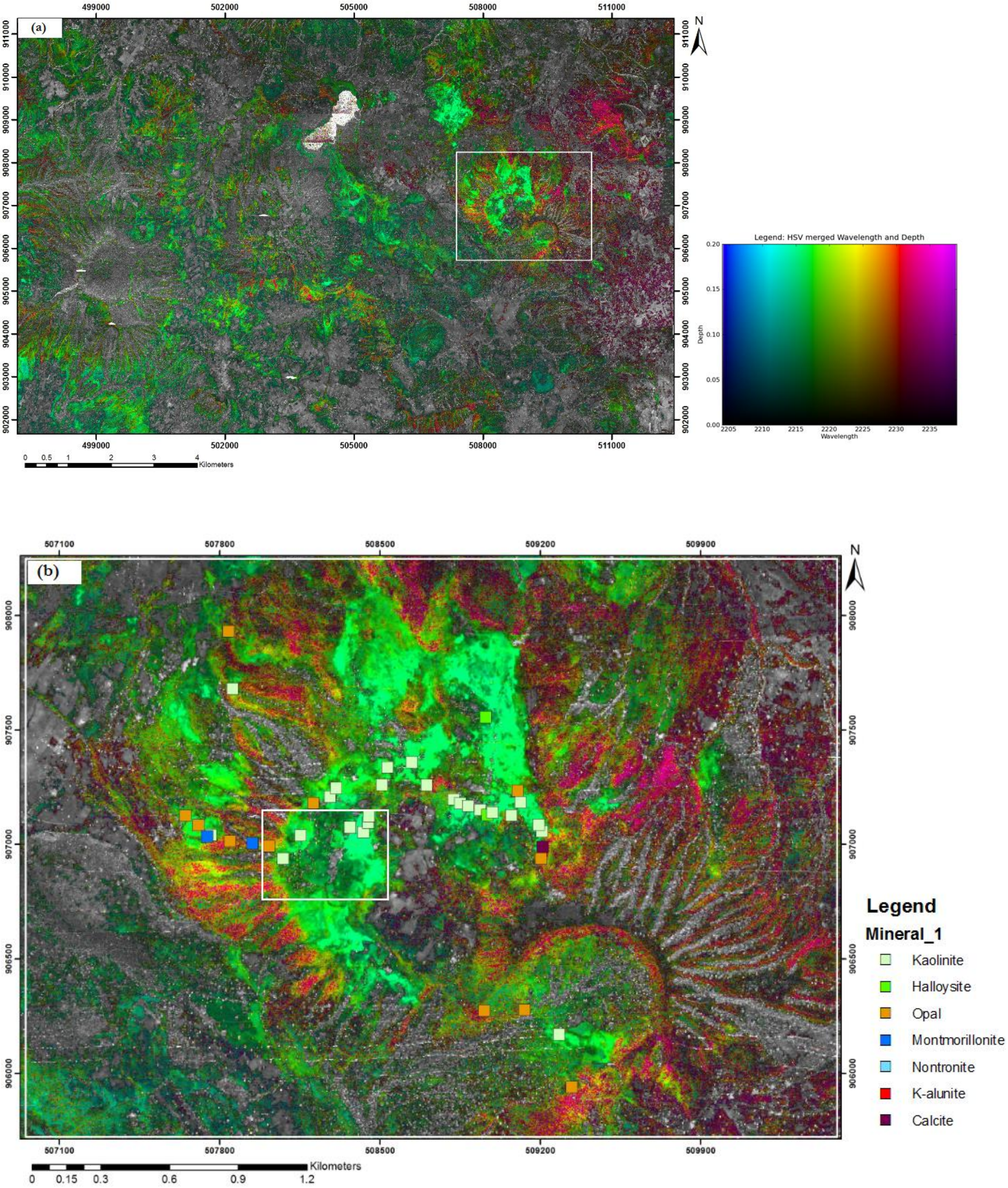

Figure 5.7: (a) Resulting map from wavelength mapping algorithm with the wavelength value for colour interpretation; (b) Zoom in of detailed study area with mineral-1 observation points overlay, (white box in 5.7b is shown as Figure 5.8 in next page)

At higher depth of absorption feature, the degree of colour saturation increases; thus similar spectra with same wavelength position of absorption feature will show slight changes in colour saturation as a result of different depth of absorption. Figure (5.8) show difference in colour saturation in similar (kaolinite) spectra as a result of different depth of absorption feature (depth of absorption feature indicate as D1 and D2). At higher depth, the colour becomes bright while lower depths shows dark colour.

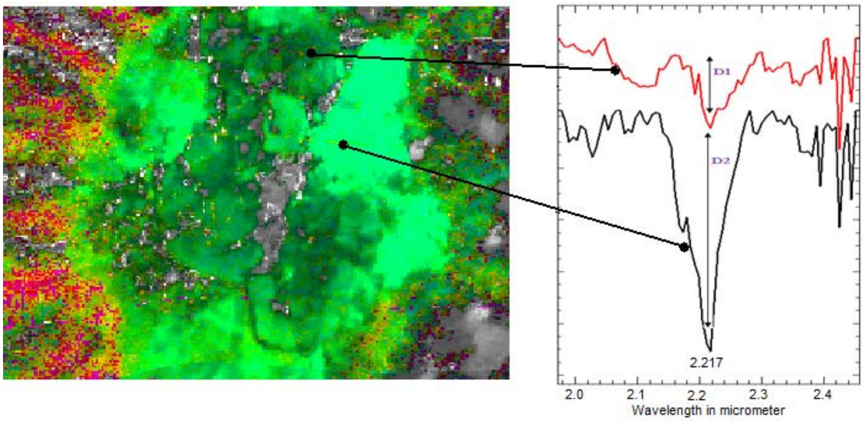

Figure 5.8: Part of study area showing difference in depth of absorption feature resulting in colour saturation differences (light green=higher depth, dark green=lower depth)

Regionally, major part of the mineral alteration in the study area is reflected in the wavelength region between 2215 nm to 2225 nm shown as green colour. Less area reflect higher absorption features (2225 nm and above) shown as yellow-red-magenta colour (see Figure 5.7a). The resulting map can be used to find altered versus unaltered area and the colour indicates different clay compositions.

Larger part of detailed study area show predominantly wavelength of 2215 nm to 2220 nm (green colour) (Figure 5.7b). Interpretation of this absorption feature wavelength range indicates presence of kaolinite with absorption features at wavelength of 2217 nm leading to the bright green colour on top of the crater (i.e. plus wavelength shift of 9 nm due to inadequate wavelength calibration of the sensor mentioned earlier, usually kaolinite absorption wavelength is around 2.208 µm.). Some pixels in the kaolinite region are mixed with other minerals causing a slight change in the spectral shape and decrease in the absorption depth, though deepest absorption features at wavelength of 2217 nm are retained, these pixels are reflecting as dark green in the image. On the ridges, different colours were noticed (yellow and red colour) meaning different absorption wavelength. Mineral interpreted from the yellow colour is montmorillonite (smectite) with deepest absorption features at wavelength of 2223 nm (i.e. plus wavelength shift of 9 nm). Most pixels from red colour area have deepest absorption features at wavelength between 2230 nm and 2236 nm (i.e. plus wavelength shift of 9 nm), which is similar to absorption features of Palygorskite, although in samples analyzed from field data, such location have occurrence of Opal and Palygorskite. The knowledge obtained from the field data about minerals present in the study area is to assist in interpreting better the result from wavelength mapping. Display of mineral observation points on the map with detailed study area also show correlation with mineral interpretation applied to the wavelength mapping result (Figure 5.7b).

On the north-eastern part of the entire study area (Figure 5.7a), more of the longer wavelength absorption feature exists with wavelength of 2235 nm and above (magenta colour). Pixel within 2230 nm and 2236 nm can also be interpreted as Palygorskite while those higher that this will be assumed as another mineral which is unknown. Unfortunately, field sampling was not carried out in this part of the study area in order to have idea or knowledge about mineral existing in this part of the area (the basaltic lithological unit). The grey colour part of the map indicates extreme values not considered in the wavelength mapping algorithm, they are mainly agricultural field and vegetation cover based on field work observation.

5.2.2. Minimum Noise Fraction Transformationn

The MNF transformation was done to check the dimensionality of the data and to find areas with different spectral behavior. Flightline eight was used for this analysis and the result showed quality of the image in cascading order of signal to noise ratio (SNR). 20 MNF bands were generated out of the 78 bands used for the processing. The first 13 bands contain information useful for interpretation while band 19 and 20 barely contain any information. Figure (5.9) show series of output image from bands 1 to band 12 respectively.

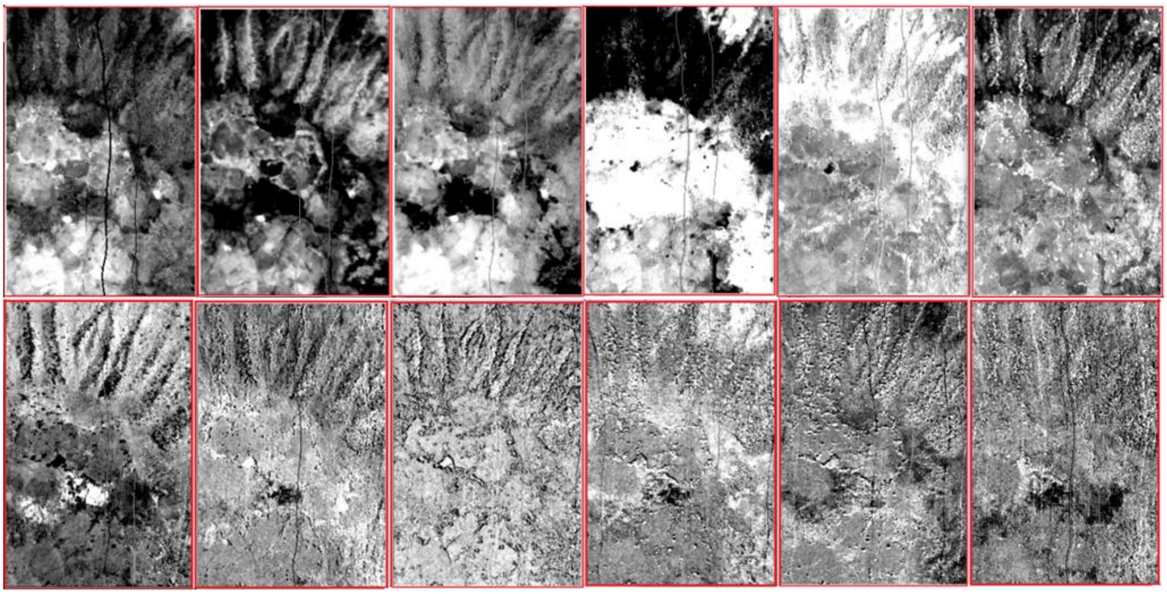

Figure 5.9: First 12 bands of MNF output with decrease in SNR of part of the study area

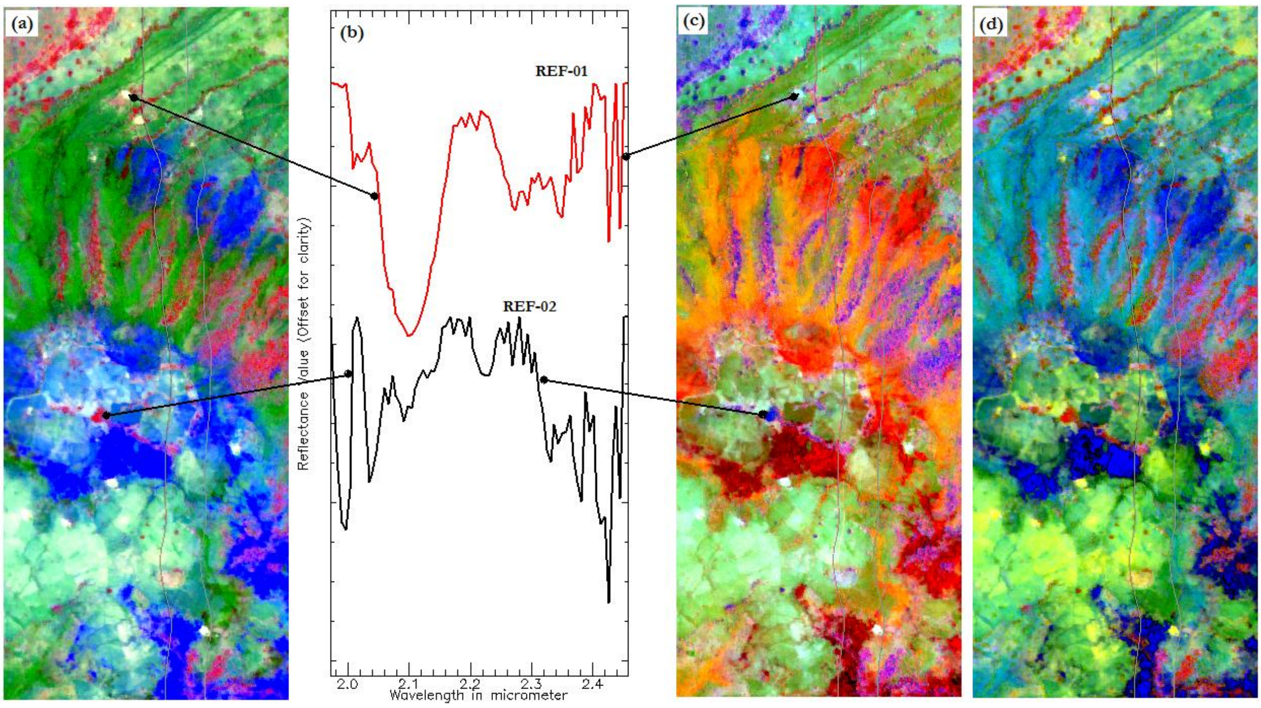

Figure 5.10: (a) MNF band 2, 3 & 4; (b) Reflectance spectra of distinct area in the colour composite; (c) MNF band 5, 3 & 2; (d) MNF band 2, 3 & 7

Colour composite of various bands were combined to check for further information (Figure 5.10 a, c, d). Some distinct features in term of different colour from surrounding colour were noticed in MNF band 2, 3 and 4 as well as in other MNF band combination as shown above. Reflectance spectra of such areas were collected for analysis in order to interpret what likely mineral might be present. The white dot area symbolize with spectra REF-01 have absorption feature similar to that of calcite at wavelength of 2.343 µm, but not having other absorption features of calcite. The deepest absorption feature is found at wavelength 2.097 µm, this does not match any mineral spectra using the guide from spectral interpretation field manual, thus, the mineral related to the spectra REF-01 is yet to be known.

The second part noticed in the MNF colour composite image is the reddish-pink dot area around the kaolinite area, spectra here is represents as REF-02. The spectrum is noisy although absorption feature at wavelength position of 2.331 µm is noticed which is similar to one of the double absorption feature of chlorite spectra, but other absorption features were not found. So, it cannot be established that it is a chlorite spectra. Comparison of spectra from MNF output (REF-01 and REF-02) with USGS spectra library is shown in Figure (5.11a and 5.11b). There is no much correlation in the absorption features or in the spectra shape. More information is needed to better interpret the distinct features in the MNF output image.

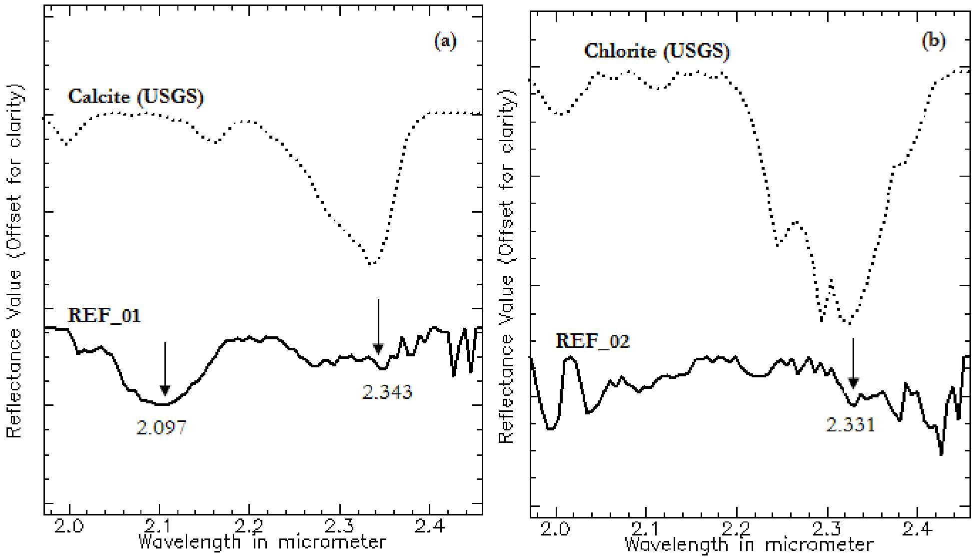

Figure 5.11: Spectra from MNF output compared with USGS spectra library

5.2.3. Endmember Collection

Eight (8) groups of endmembers were identified from the image using the method described in chapter four (Figure (5.12). The selected endmembers were further compared with USGS library spectra to check their similarity in absorption features and spectral shape.

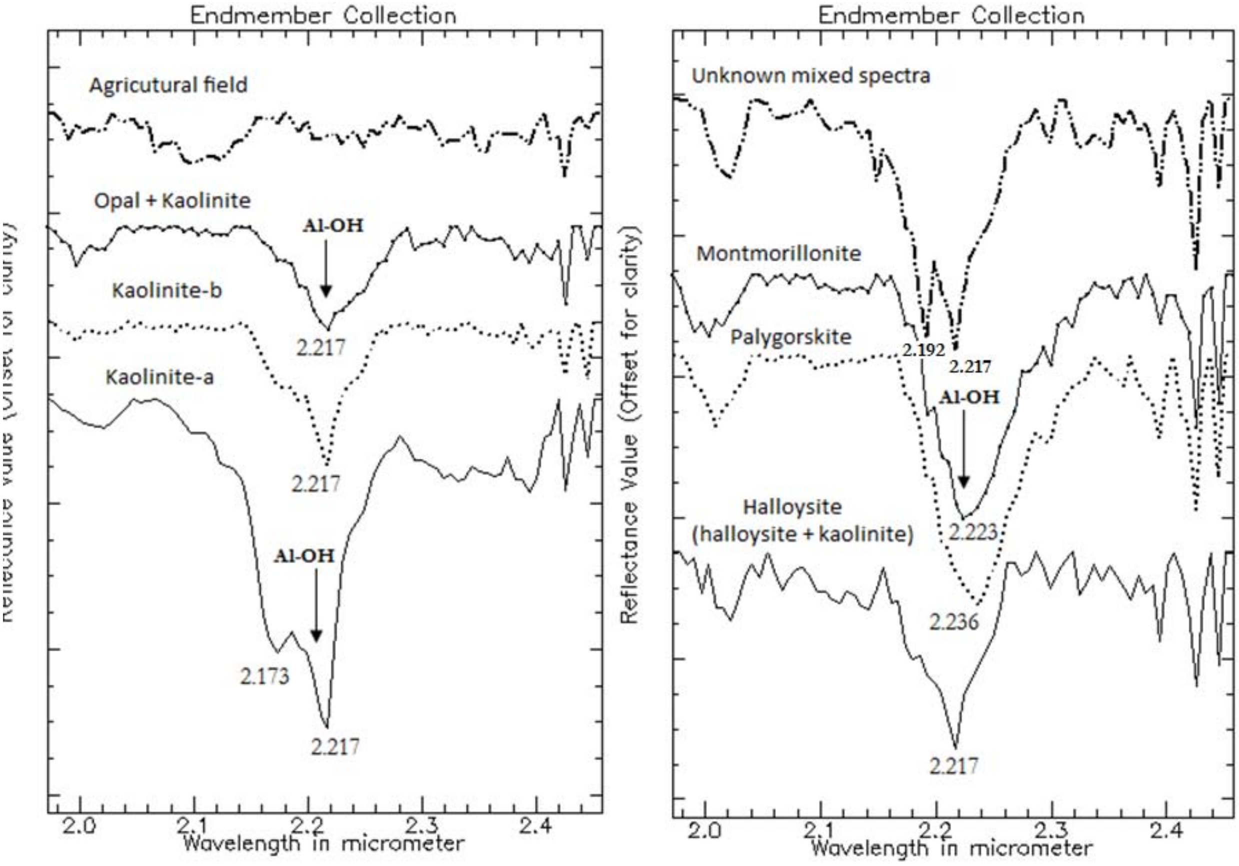

Figure 5.12: Image derived endmembers

Kaolinite spectrum is clearly seen in few area of the image while in many case, it occur as mixed spectra. Therefore, due to impurity of the pixels, two endmembers were selected for kaolinite [i.e. kaolinite (a) and kaolinite (b)] in order to obtain good classification result. Halloysite and kaolinite which are both kandite mineral group are found in association with each other with main absorption feature at 2.217 μm, they are group together as halloysite endmember. It is difficult to distinguish between kaolinite and halloysite spectra but based on information from field analysis, where pure spectra of halloysite were found in some samples, halloysite endmember is selected. Similar case occurs with presence of opal and kaolinite with absorption feature of kaolinite at 2.217 μm but spectral shape of opal (Figure 5.12). These two minerals also exist together in many samples from field data.

Montmorillonite which belong to smectite group exist as an endmember. Spectra of palygorskite were found in the image with absorption feature of 2.236 μm against the usual palygorskite absorption feature of 2.225 μm when there is no wavelength shift. It is therefore considered as endmember, although it occurs often with opal in the field data. But the absorption feature and the shape is more of palygorskite and have no similarity with opal (see comparison of image endmember comparison with USGS in Figure 5.13).

Other mixed spectra of unknown minerals exist in the image. Although diagnostic double absorption feature of Al-OH was noticed in some of the pixels group under this endmember at 2.192 µm and 2.217 µm, it is similar to alunite absorption feature but other diagnostic absorption feature of alunite were absent, therefore the group was not considered as alunite but grouped as unknown mixed spectra. Endmember was selected for agricultural field/vegetation cover to distinguish it from altered area in the classification result; they are without diagnostic absorption feature.

Nontronite and calcite spectra that occur in two to three samples from field data were not found in the image same pixels (location) in the image. Few spectra from the image that have absorption feature similar to that of nontronite and calcite were classified into agricultural field area when used for the SAM classification. These spectra were ignored and not considered as endmember because the area they appear in the SAM classification result were observed during field work as agricultural field use for cultivation of cereal. The image endmembers comparison with USGS library in the wavelength region of 1.98 µm to 2.46 µm is display in Figure (5.13) showing similarity in absorption features and spectral shapes.

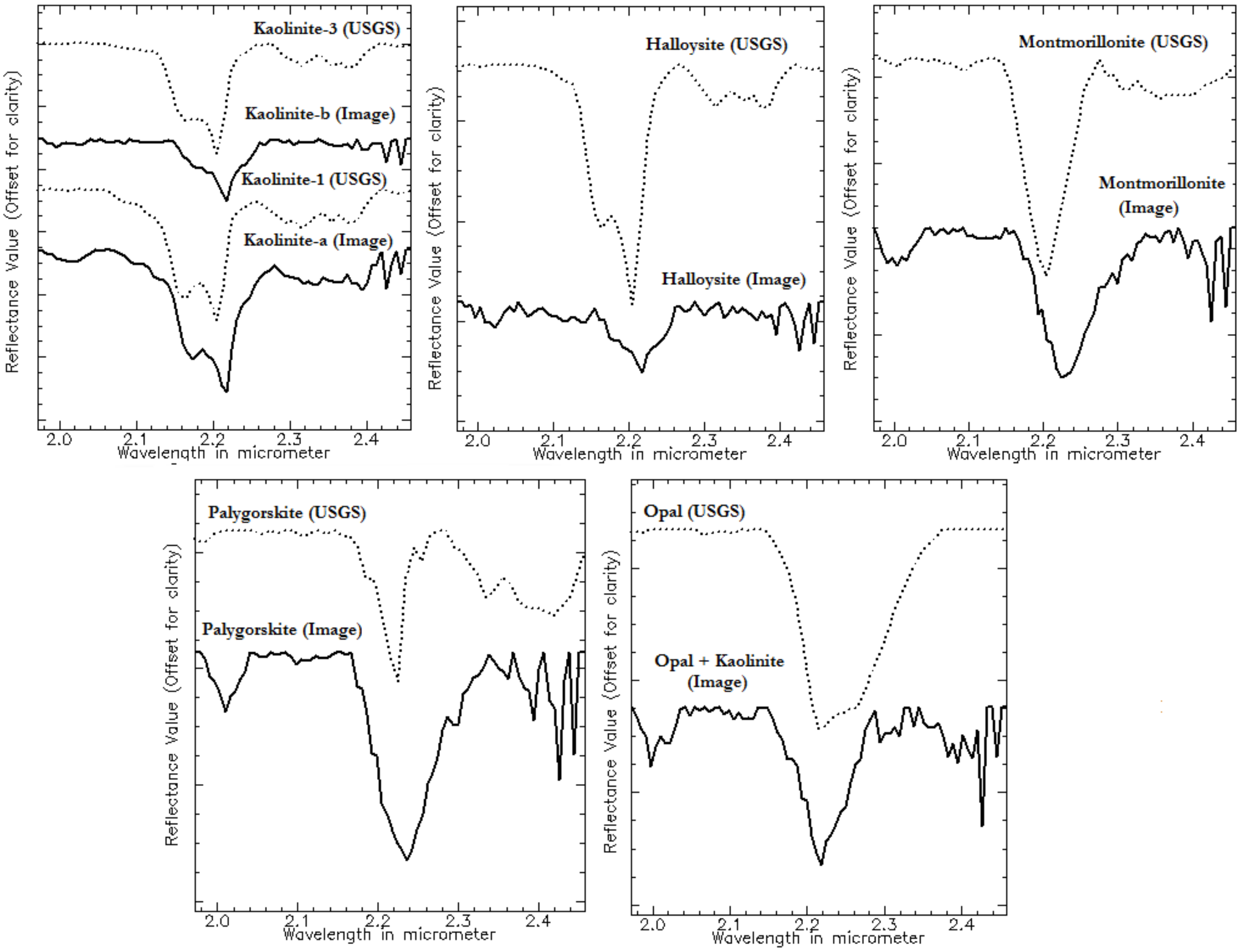

Figure 5.13: Comparison of image derived endmembers with USGS spectra library

5.2.4. Spectral Angle Mapper Classification

The image endmember spectra (Figure 5.12) serve as inputs in Spectral Angle Mapper (SAM) classification algorithm in order to determine spatial distribution of alteration mineral in the study area, especially the clay alteration minerals and their extent of occurrence. Before the discussion of the SAM classification result (surficial mineral map), some of the rule images generated are shown and their false colour composite.

- ***Rules Images and False Colour Composite.***

Rule images for each endmember were generated from the Spectral Angle Mapper classification algorithm. Some of the rule images generated from SAM classification in the analysis are shown in Figure (5.14). Areas in the image with dark colour show where the best matches occur. The display images are rule images for kaolinite, Montmorillonite and halloysite respectively.

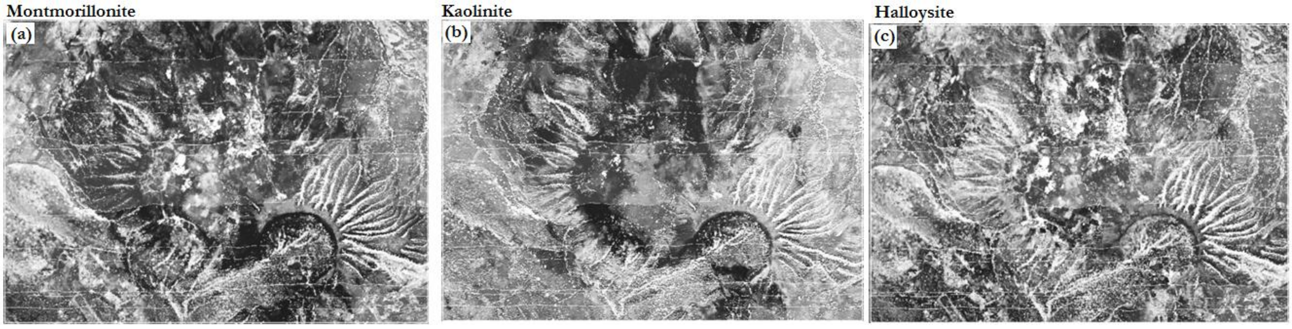

Figure 5.14: SAM classification rule images of detailed study area (a) Montmorillonite; (b) Kaolinite; (c) Halloysite (Dark shades indicate good fit)

False colour composite of the SAM rule images was produced to see if there is pattern in the alteration minerals present in the study area and also to compare it with the final mineral map obtained. Colour composite is a useful approach of combining three separate wavelengths bands of black and white images (as shown in the rule images) together as red, green and blue (R:G:B). Rule images for montmorillonite; kaolinite and halloysite were used as red, green and blue respectively to generate the false colour composite image. The resulting image (Figure 5.15) show contrast between the alterations minerals and also differentiate between altered area from unaltered area. There is variation in colour obtained from this image. The light green coloured area indicated with letter "“B" clearly show where the kaolinite mineral occur while the dark green (letter "A") reflects the unaltered area which most part are considered as agricultural field or vegetation cover. The light blue coloured area (letter "C") is assumed to be halloysite, since halloysite is displayed as blue in the colour composite combination. Areas with montmorillonite are expected to show red colour, thus the slight red coloured part (letter "D") are interpreted as montmorillonite area, although it might be with mixture of other minerals in reality. The part with yellowish colour (letter "E") surrounding kaolinite area is also notice, this part is interpret as mixture of opal and kaolinite; this is based on knowledge from field data analysis. Some area is also with purplish colour (e.g. eastern part of the image), minerals here are unknown. Shadow effect in some areas might also reflect as part of the purplish colour, e.g. on top of the crater (south-eastern part).

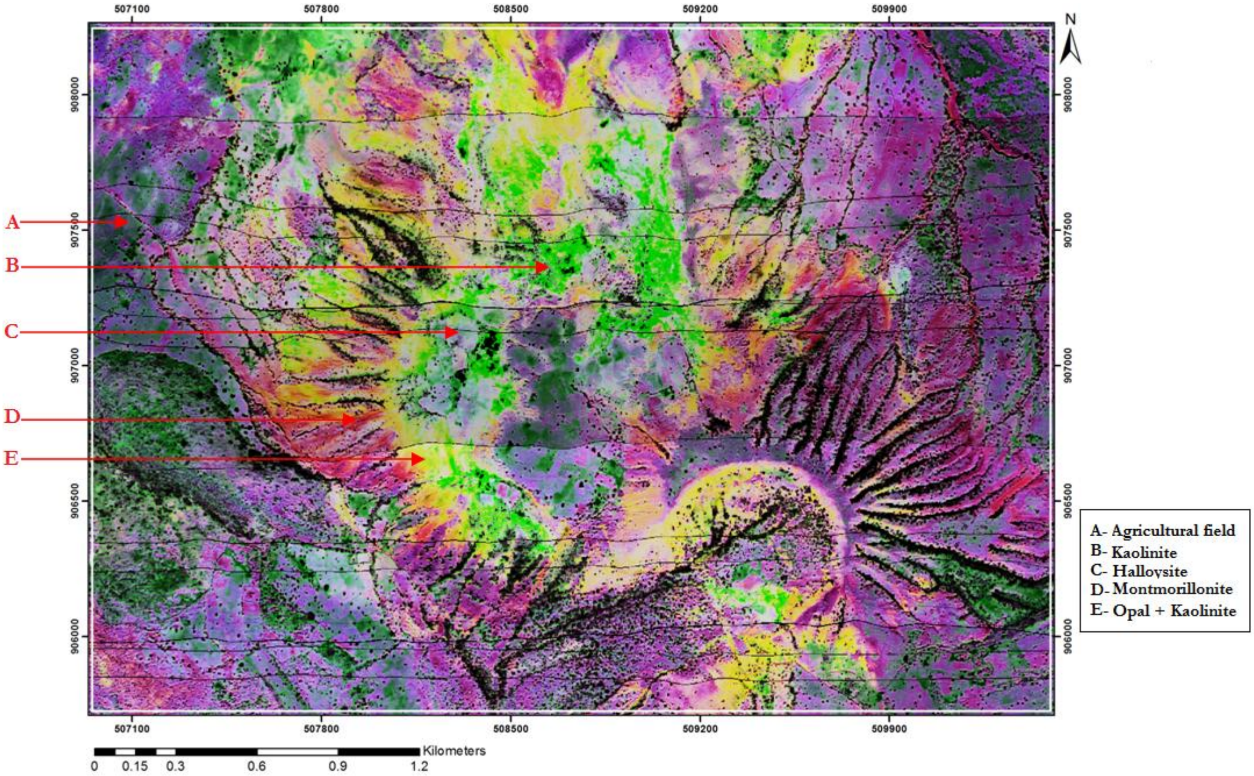

Figure 5.15: False colour composite of SAM rule image of detailed study area; R- Montmorillonite: G-Kaolinite: B- Halloysite

- **Surficial Mineral Map (SAM Classification Result)**

From SAM classification algorithm, surficial mineral map (Figure 5.16a and 5.16b) was generated, which shows spatial distribution of the alteration mineral in the study area. Figure (5.16a) shows the mineral map for the entire study area while Figure (5.16b) emphasis the differences in spatial distribution of the alteration areas in the detailed study area. From the surficial mineral map, kandite mineral group (kaolinite and halloysite) are mostly distributed over the study area, especially at the center of the study area where detailed study was carried out. Another massive occurrence of kaolinite mineral is found directly above the detailed study area (north-eastern part of the study area). Smectite mineral group (mainly montmorillonite) has low abundance and is sparsely distributed over the entire area. Occurrence of opal in association with kaolinite is also much in the study area. They occur in vast extent in north-eastern of the study area and at the central part (detailed study area). Palygorskite is less common over the study area in comparison with occurrence of opal and kaolinite. Palygorskite are found on the ridges,(edge of the crater) (Figure 5.16b). The unknown mineral group with mixed spectra is also common in the study area. This group could be assumed as mixture of different eroded minerals, because they are present mainly along the drainage pattern and at the river bank. Asides the alteration minerals, the agricultural field or the vegetation cover also occupy large part of the study area in which the alteration minerals occur in between.

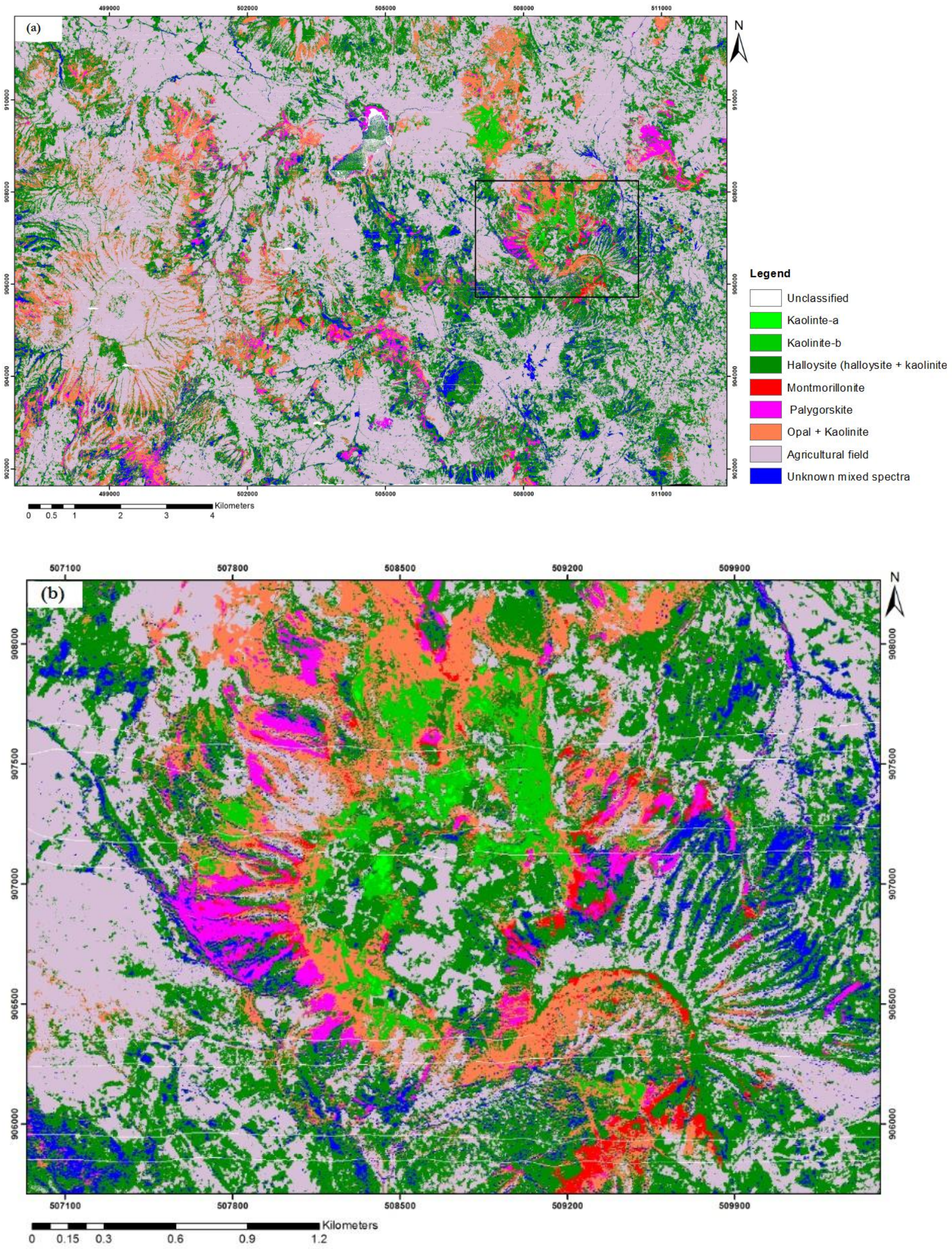

Figure 5.16 (a) Surficial mineral map obtained from SAM classification algorithm; (b) Zoom in of detailed study area

5.2.5. Comparison of Results from Mineral Mapping Methods

Comparing the result from wavelength mapping, false colour composite of rule images, MNF and SAM classification, it can be deduced that the output images complement each other. In the case of wavelength mapping, it is a fast method that gives overview about the spectral pattern in the study area showing the main absorption features. By restricting the algorithm to 2.204 µm and 2.439 µm wavelength range, clay features related to alteration are revealed. The exact mineral associated with different wavelength position is not known, extra step has to be taken by relating the minimum wavelength position to likely minerals in order to know the type of alteration mineral present. But in general, the method show clear difference between altered areas and unaltered area as well as patterns within the altered areas without the use of endmember (see Figure 5.7a and 5.7b).

MNF transformation algorithm also complements other methods used in understanding the characteristics of hydrothermal alteration mineral in this study. MNF help to see other distinct features that are not easily recognized with wavelength mapping. SAM classification algorithm deals with actual classification of the minerals and groups each pixel in the image to the endmembers that it matches. Each pixel is assigned to a mineral class. However, it is a long method that required experience analyst in selecting the correct endmembers as a training set in which the classification will be based on. The result from SAM complements that of wavelength mapping because altered area remains the same in both and vice versa, the only difference is that SAM classification assign mineral name to each pixel which is not the case in wavelength mapping. False colour composite result is also in agreement with the other methods but does not give thorough classification in comparison to SAM algorithm. However, mineral present in the bands used for the FCC combination is usually emphasized in the FCC result. For example in Figure (5.15), kaolinite showed up very well in green colour because rule image of kaolinite was put in as green band in the R:G:B false colour composite, so also is montmorillonite appearing in red colour, although it might be in mixture with other minerals.

5.2.6. Kaolinite Crystallinity Result from Image

The same methodology used in calculating kaolinite crystallinity on field data was also applied to the image (mainly on the flightline 8, where most of the detailed study was carried out). The kaolinite crystallinity was calculated on kaolinite (a) and kaolinite (b) group after masking it from SAM classification result as shown in Figure (5.17a-c). The image in Figure (5.17c) is the output image from KCI (second method that combine the two slope parameter), density slicing was applied to show variation in the KCI value and to check pattern in the kaolinite altered area. The kaolinite crystallinity index values obtained ranges between 0.824 – 1.227. Most of the KCI value falls within the range of 0.90 - 1.10, pixels below 0.90 and above 1.20 were not common in the area, especially in the zoom in part, they do not appear. Result from slope parameter values shows that high – moderately crystalline kaolinite as well as moderate - poorly crystalline kaolinite exist in the study area. Relating this to KCI method in the image shown in Figure (5.17c), the blue and red coloured pixels are mostly the high – moderately crystalline kaolinite while the green coloured pixels are moderate – poorly crystalline kaolinite. This is somewhat different from the field data result where almost all sample analyzed falls within the high - moderately crystalline kaolinite. The results from the image which shows moderate – poorly kaolinite crystallinity might be as a result of impurity in the pixels which affect the spectra shape, hence kaolinite crystallinity values. Therefore, since some values falls into the high - moderately crystalline kaolinite (mostly kaolinite (a) endmember group which have pure spectrum of kaolinite), the best hypothesis is to make use of the high – moderately crystalline kaolinite from the image in combination with result of kaolinite crystallinity value from field data which is more reliable and use this for the interpretation needed for the study area. And the interpretation is the same as mentioned in kaolinite crystallinity conclusion from field data that hydrothermal alteration is the most likely origin for the kaolinite in Berecha area. Pattern seen in the image in Figure (5.17c) shows that the high – moderately crystalline kaolinite occur mainly at the central part of the image while more of the moderate – poorly crystalline kaolinite occur in the other part.

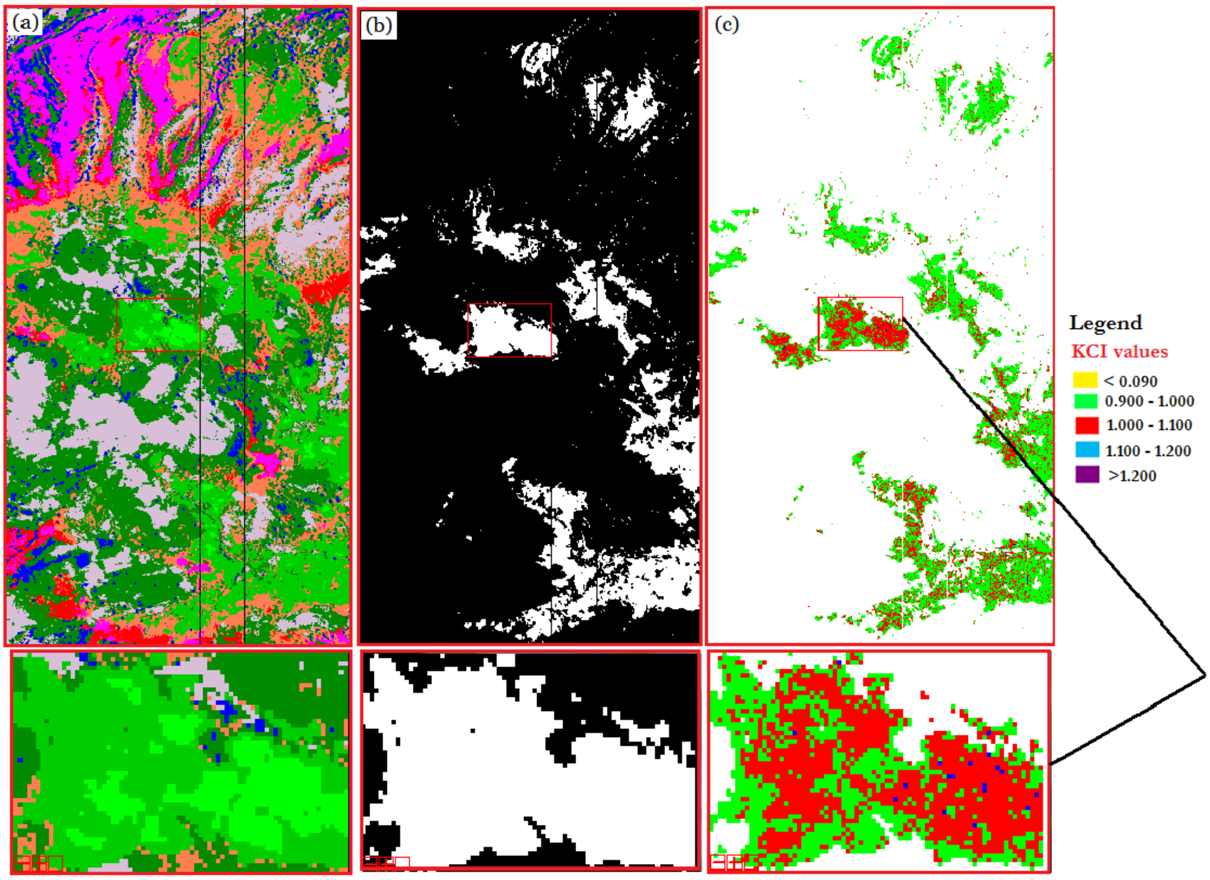

Figure 5.17: (a) SAM classification result of part of the image; (b) Masking out of kaolinite from the SAM – white colour indicates kaolinite (a) and kaolinite (b) while black indicates other minerals; (c) Image showing variation in KCI value for kaolinite pixels)

5.2.7. Comparison of Field and Airborne Result

- **Using minimum wavelength from laboratory and image spectra**

Image and field data were compared to see if there is any agreement between the two. Minimum wavelength of absorption feature for laboratory and image spectra were analyzed for the comparison. Deepest absorption features of laboratory spectra analyzed from field data (where detail study was carried out; station 038 – 064 along the profile section) were checked against spectra in same point (location) in the image using the interpolated wavelength position values (Table 5.2). The plot of deepest absorption feature of wavelength between the laboratory spectra against the image spectra shows certain degree of correlation between the two, although variation occurs in few cases (Figure 5.18a). The plot of minimum wavelength values of laboratory spectra and that of the image spectra at each sampling points (location) also shows correlation between the image and the laboratory spectra. When minimum wavelength of laboratory spectra is high the wavelength position in the image also is high and vice versa (Figure 5.18b), except on few occasion when two have relatively same value (e.g. sample AL-10-040b).

Station Number	Laboratory spectra min. wavelength values	Image spectra interpolated min. wavelength values	X-Coordinate	Y-Coordinate
AL_10_038	2209	2212	507646	907117
AL_10_039	2211	2218	507712	907081
AL_10_040a	2208	2213	507761	907041
AL_10_040b	2212	2211	507747	907037
AL_10_041	2217	2236	507848	907013
AL_10_042	2215	2226	507944	907005
AL_10_043	2217	2236	508015	906996
AL_10_044	2209	2240	508078	906940
AL_10_045	2207	2217	508156	907041
AL_10_046	2215	2217	508208	907179
AL_10_047	2208	2230	508281	907213
AL_10_048	2207	2218	508313	907250
AL_10_049	2208	2216	508366	907075
AL_10_050	2208	2209	508425	907054
AL_10_051	2207	2218	508542	907093
AL_10_052	2208	2225	508454	907128
AL_10_053	2209	2217	508510	907264
AL_10_054	2208	2218	508530	907339
AL_10_055	2207	2220	508641	907358
AL_10_056	2208	2217	508707	907259
AL_10_057	2210	2217	508821	907201
AL_10_058	2209	2222	508849	907180
AL_10_059	2208	2219	508887	907171
AL_10_060	2210	2217	508942	907150
AL_10_061	2206	2216	508973	907130
AL_10_062	2208	2218	508992	907142
AL_10_063	2207	2230	509072	907124
AL_10_064	2213	2222	509098	907236

Table 5.2: Table showing wavelength of minimum absorption feature for laboratory and image spectra along the profile section

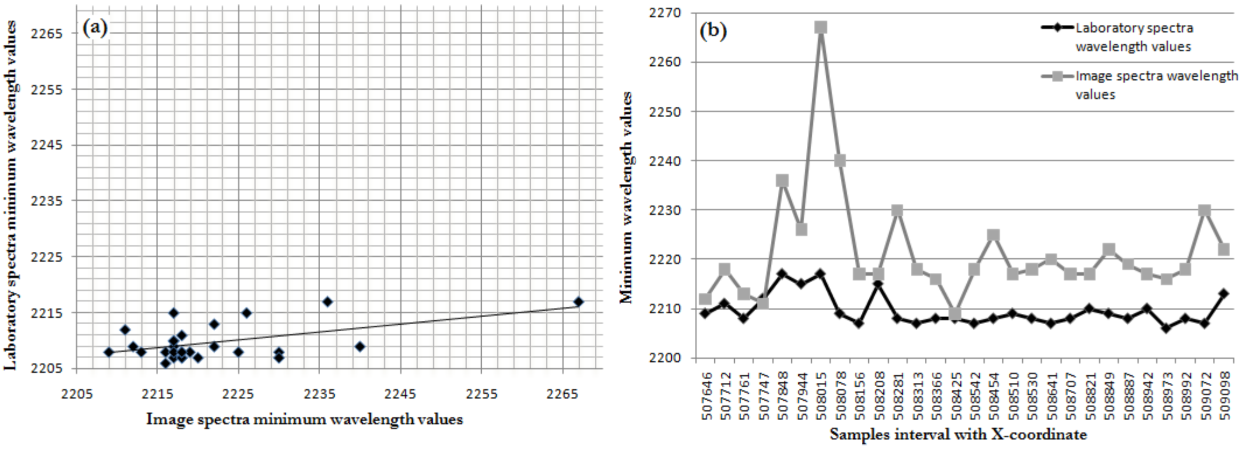

Figure 5.18 (a) Plot of laboratory spectra wavelength positions versus image spectra wavelength positions along the profile section; (b) Plot of laboratory spectra wavelength positions and image spectra wavelength position separately on sample location points

- **Using Identified Minerals From Field Data and Classified Mineral from the Image**

Minerals identified from the field data (where detail study was carried out; station 038 – 064 along the profile section) were checked against same points on the SAM classification result in the image. Minerals in many points were in agreement while on few occasion, they are wrongly classified. Based on visual inspection of the two, there is over 70% agreement between the field data and the image. Most of the field data have more than one mineral identified in a sample, but in the image data, classification is done based on dominant mineral spectra, except in a case of opal and kaolinite that is group together as endmember and also halloysite referring to halloysite and kaolinite. Therefore, there is still reasonable agreement between the field and the airborne data. Comparison between minerals found in the field data and that of the image is shown in Table (5.3)

Station Number	Minerals identified from field data	Image SAM Classification minerals	X-Coordinate	Y-Coordinate
AL_10_038	Opal + Kaolinite	Opal + Kaolinite	507646	907117
AL_10_039	Opal + Halloysite + Kaolinite	Kaolinite (b)	507712	907081
AL_10_040a	Kaolinite + halloysite	Kaolinite (b)	507761	907041
AL_10_040b	Montmorillonite + halloysite + Opal	Montmorillonite	507747	907037
AL_10_041	Opal + Palygorskite	Palygorskite	507848	907013
AL_10_042	Montmorillonite	Opal + Kaolinite	507944	907005
AL_10_043	Opal + Palygorskite	Opal + Kaolinite	508015	906996
AL_10_044	Kaolinite + Halloysite	Kaolinite (b)	508078	906940
AL_10_045	Kaolinite + Halloysite	Kaolinite (b)	508156	907041
AL_10_046	Opal	Opal + Kaolinite	508208	907179
AL_10_047	Kaolinite	Kaolinite (b)	508281	907213
AL_10_048	Kaolinite	Halloysite	508313	907250
AL_10_049	Kaolinite + Halloysite	Halloysite	508366	907075
AL_10_050	Kaolinite + Halloysite	Kaolinite (a)	508425	907054
AL_10_051	Kaolinite + Opal + Halloysite	Kaolinite (a)	508542	907093
AL_10_052	Kaolinite + Halloysite	Kaolinite (b)	508454	907128
AL_10_053	Kaolinite + Halloysite +Opal	Halloysite	508510	907264
AL_10_054	Kaolinite	Kaolinite (a)	508530	907339
AL_10_055	Kaolinite	Halloysite	508641	907358
AL_10_056	Kaolinite + Opal + Halloysite	Agricultural field	508707	907259
AL_10_057	Kaolinite + Halloysite	Kaolinite (b)	508821	907201
AL_10_058	Kaolinite + Halloysite	Kaolinite (b)	508849	907180
AL_10_059	Kaolinite + Halloysite	Kaolinite (a)	508887	907171
AL_10_060	Kaolinite + Halloysite	Kaolinite (b)	508942	907150
AL_10_061	Halloysite + Kaolinite	Kaolinite (b)	508973	907130
AL_10_062	Kaolinite	Kaolinite (a)	508992	907142
AL_10_063	Kaolinite + Halloysite + K-alunite	Kaolinite (b)	509072	907124
AL_10_064	Opal	Kaolinite (b)	509098	907236

Table 5.3: Comparison between minerals from field data and mineral classification from the image (SAM result)

5.3. LiDAR-DEM Data: Link between Structure and Mineralogy

Outcome of interpreted structures from LiDAR-DEM data was used to generate spatial distribution of faults and fracture (lineament) and other structures in the study area as shown in Figure (5.19). The faults in the study area do not all follow the NNE - SSW trending of the Wonji Belt Fault (WFB) described as the pattern of faulting in the south and north of the MER (Boccaletti et al., 1998; Korme et al., 2004). In contrast to this, most of the faults strikes in NW-SE direction, same is observed by Abebe et al (2007) of Bora-Berecha area faulting and E-W trending in some cases.

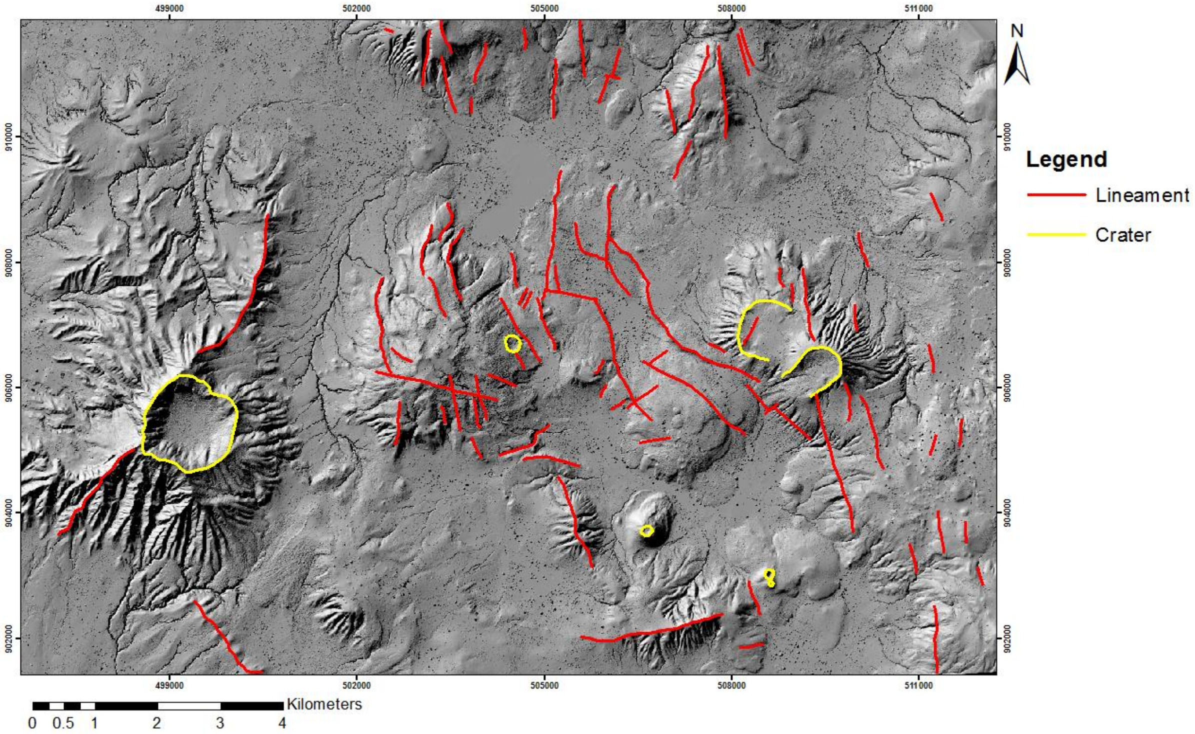

Figure 5.19: Lineament map of the study area overlay on LiDAR-DEM image

The lineament map display on the surficial mineral map gives some understanding of the impact of structure on alteration mineral distribution in the study area (Figure 5.20a and 5.20b). The output maps show that structure as well as lithology controls the alteration in the study area. The alterations are seen to occur around structures (lineaments) which could be faults lines or fractures and also occurring around the crater (Figure 5.20b). Crossing-cutting indicates that there was multiple episode of faulting. The NW-SE striking faults are older faults while the NE-SW cut crossing them are younger (common in the central part of the study area). The structure exists before the alteration in some cases (pre-alteration) while in other cases the alteration is younger and exists after the structure (post-alteration). In Figure (5.20b), the fault line on top of the lower crater cut across kaolinite and other minerals like montmorillonite, it can be interpreted that the structure exists after the alteration (i.e. structure is younger than the alteration) or that the structure exist before the alteration, but become inactive and after some period of time get active again, thus seen as cutting across different alterations. In some other part of the area, the alteration follows after existing structure leading to formation of minerals like kaolinite on top of the crater. The alteration in Berecha area is thus considered to have structural control. Studies from others have also shown that structures such as faults, shear zones or fracture have some form of control on formation of many types of ore deposits (mineralization) associated with hydrothermal system (Forde and Bell, 1994; Jeremy and Richards, 2004).

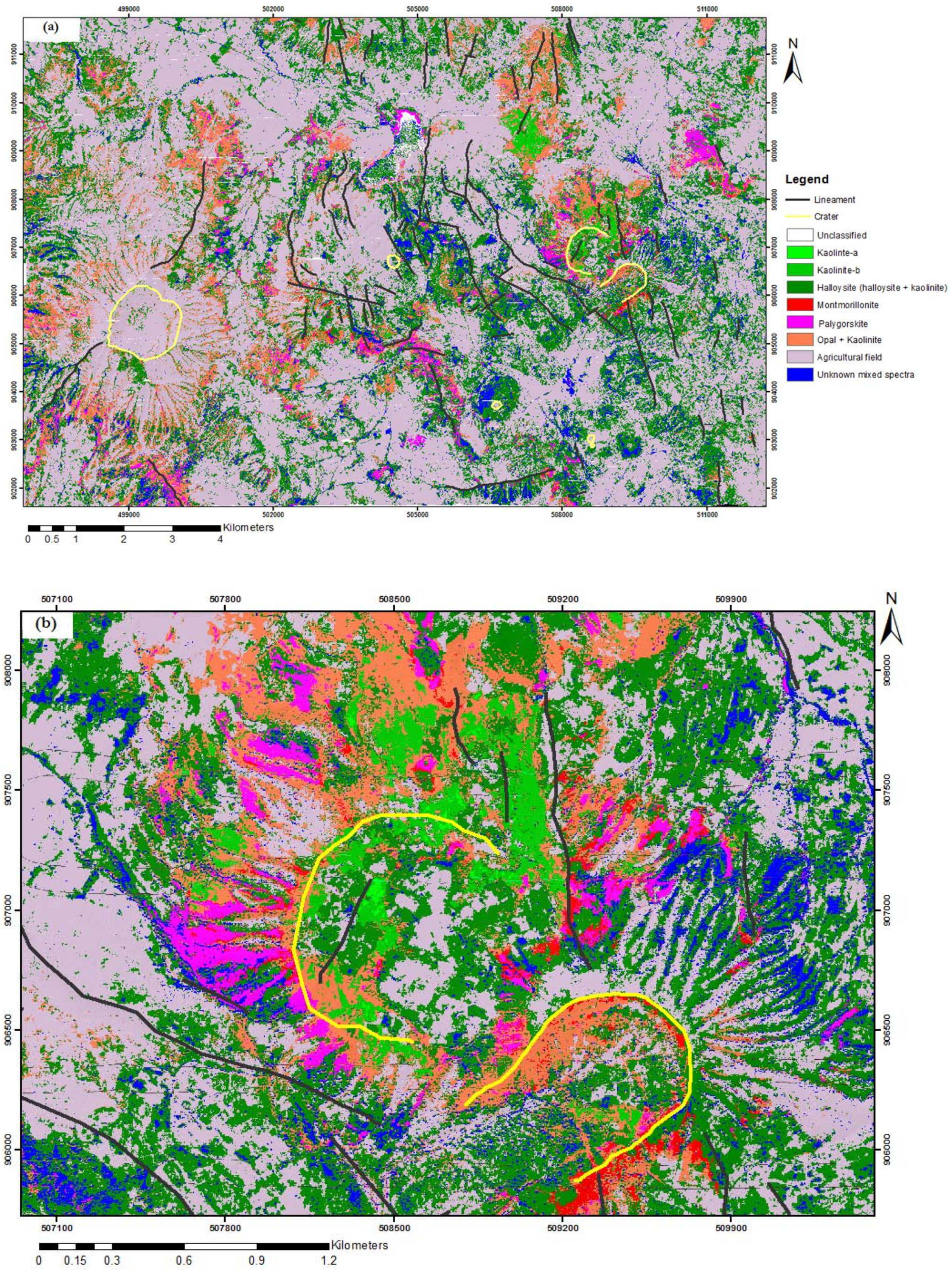

Figure 5.20: (a) Lineament map overlay on surficial mineral map; (b) Zoom in of detailed study area

5.4. Result of 3-D Model

In order to have more insight into the characteristics of hydrothermal alteration in the study area, the spatial distribution of the alteration minerals and the control of structure on the alteration minerals, 3-D model was generated combining the information extracted from previous results (Figure 5.21a and 5.21b). The model shows the geomorphology of the study area in relation to spatial distribution of the alteration minerals. The alterations were found mostly around the volcanoes above the low land. This agrees with geological environments which host most alteration minerals (usually volcanic rocks). Most of the pure kaolinite minerals (i.e. unmixed kaolinite) with intense alteration were seen to form on the flat surface on top of the volcano (see Figure 5.21b). This is related to the formation of argillic alteration above the water table where lateral spread of the deep reservoir fluids, together with the effects of cooling and fluids mixing occur (White and Hedenquist, 1990). Pattern of other alteration minerals (halloysite, opal, montmorillonite and palygorskite) are also seen in the 3-D model. Intense alteration occurs mostly towards the central part of the study area around the volcanoes and on the south-eastern part. Less alteration occurs in the north-western part of the study area in the lowland area. Other lowland area which is mainly alluvial lithological units (volcano-sedimentary) is not associated with much alteration. The 3-D model reveals more of the association of alteration minerals in Berecha area with the volcanic rocks (high elevated centers). The unknown mixed spectra which were assumed to be mixture of eroded minerals or materials are seen to be more on the lowland following the drainage pattern. The area mapped as agricultural field (vegetation cover) is also showing clearly in the lowland which is a model of reality because agricultural field is usually on the lowland for easy accessibility. The effect of structures in form faults and fracture (lineaments) on the alteration minerals in the study area is also reflects in the three dimensional view. The alterations minerals are seen occurring around the structures. Some fault line cut across different alteration type while some fault lead to formation of particular alteration type. The massive occurrence of kaolinite towards the northern part above the crater is likely form as a result of existing structure in that area (see Figure 5.21a).

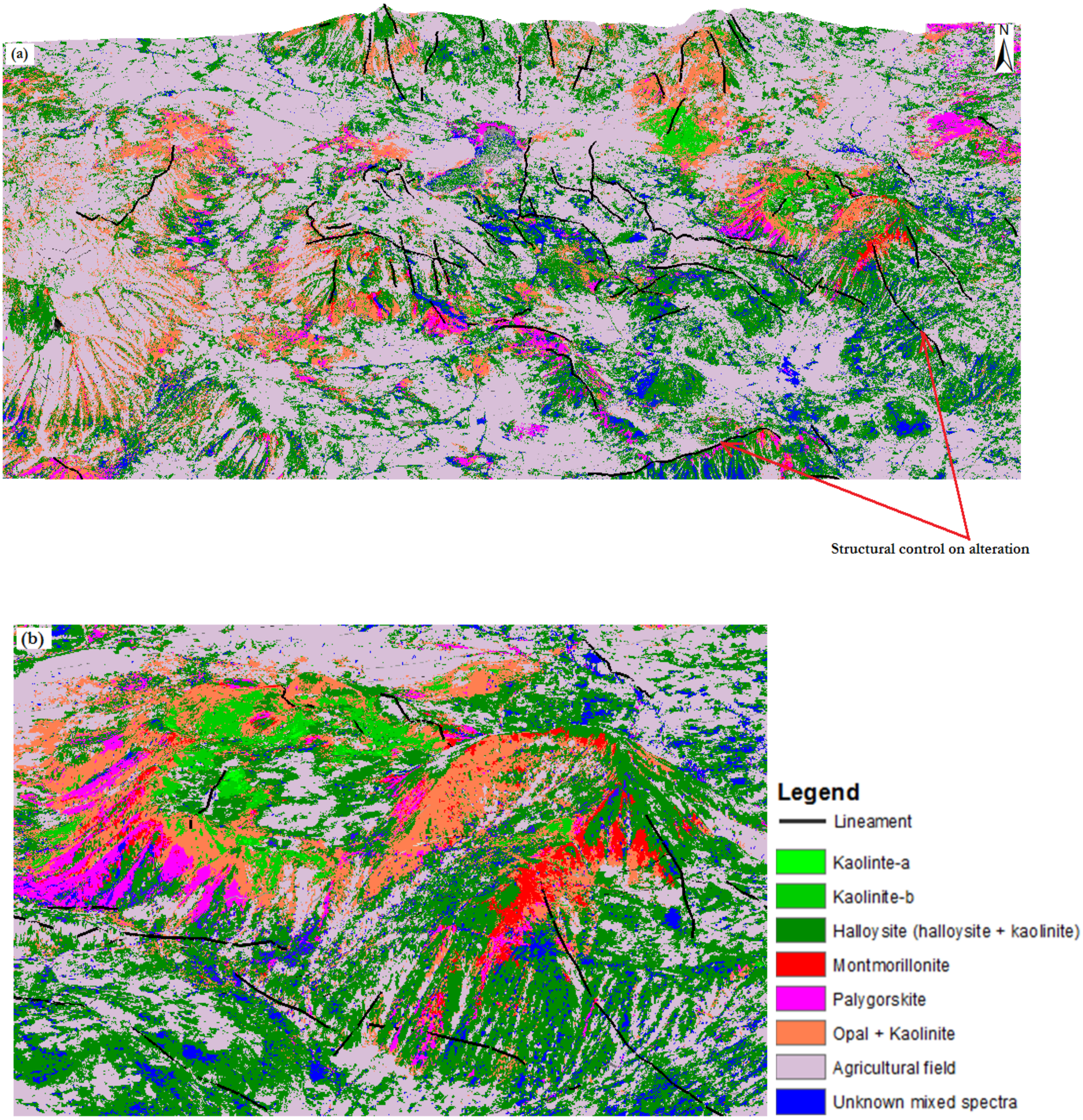

Figure 5.21: (a) 3-D Model of study area showing spatial distribution of alterations minerals with lineament map overlay; (b) Zoom in of detailed study area

6. LINKING RESULTS AND CONCEPTUAL MODEL OF HYDROTHERMAL SYSTEMS TO BERECHA AREA

This chapter described various styles of hydrothermal systems and combining it with results obtained from the previous analysis to understand the type of system that exist in Berecha area.

6.1. Styles of Hydrothermal Alteration

Hydrothermal system undergoes physical and chemical change at shallow depth such as interaction of fluid at depth with near-surface water, changes from lithostatic to hydrostatic pressure (resulting in boiling), permeability changes, reaction between fluid and host rock, which all together characterizes most epithermal deposits (White and Hedenquist, 1990). Thus, understanding of hydrothermal system is important in term of style, origin or pattern of alteration, mineral assemblages, depth and temperature of formation, gauge mineral etc (Hedenquist et al., 2000). In epithermal environment, two main styles occur: high sulfidation and low sulfidation (Sillitoe and Hedenquist, 2003). These terms reflect the two end member sulfidation states deduced from the sulfide mineral assemblages. The *high sulfidation* deposits contain sulfide-rich assemblages of high sulfidation state such as pyrite-enargite and pyrite-luzonite, while *low sulfidation* deposits in contrast contains low-sulfidation pair of pyrite-arsenopyrite (Sillitoe and Hedenquist, 2003). The term low and high sulfidation can also reflect the oxidation state of the fluid that deposits the sulfides (Corbett and Leach, 1997). However, in between the high and low sulfidation, is intermediate sulfidation system (Hedenquist et al., 2000).

6.1.1. High Sulfidation Style

High sulfidation refers to epithermal deposits that are formed under oxidized, acidic conditions, occurring mainly in calc-alkaline andesitic-dacitic arc environment (Sillitoe and Hedenquist, 2003). The sulfide assemblage of high sulfidation deposit is often characterized by copper minerals especially the high sulfidation state sulfosalts; enargite-luzonite-covellite plus pyrite assemblage (White and Hedenquist, 1995). Quartz is a gangue mineral common in high sulfidation but adularia and calcite, both indicating near-neutral pH conditions, are absent. Texturally, high-sulfidation deposits show massive bodies of vuggy quartz where veins and breccias may be important hosts to ore (White and Hedenquist, 1995). Quartz - alunite - pyrophyllite -dickite - sericite halos are alteration mineralogy of high sulfidation (Hedenquist et al., 2000). High-sulfidation disseminated deposits are found in places like Summitville in Colorado; Akeshi, Iwato, and Kasuga in Japan; Chinkuashih in Taiwan; Masbate and Nalesbitan in Philippines; Temora in Australia (White and Hedenquist, 1990). Figure (6.1) shows a model of hydrothermal alteration pattern in high sulfidation system.

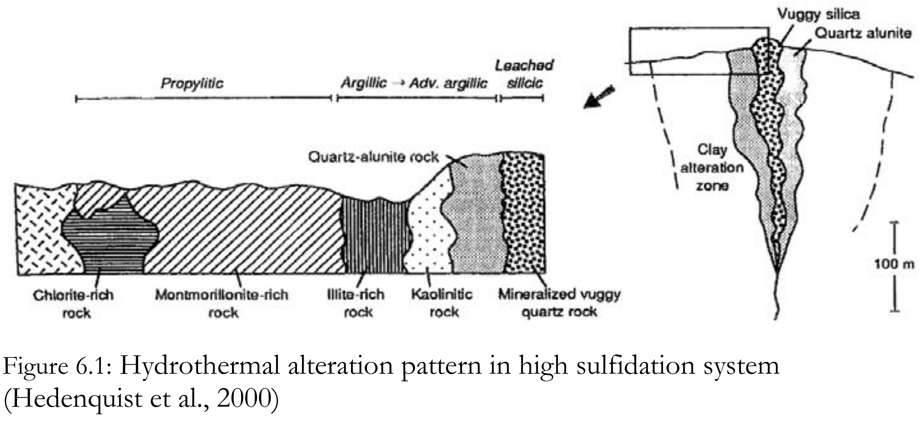

Figure 6.1: Hydrothermal alteration pattern in high sulfidation system (Hedenquist et al., 2000)

6.1.2. Low Sulfidation Style

Low sulfidation refers to epithermal deposits that are formed under reduced, near–neutral conditions, occurring mainly in bimodal rhyolite-basaltic setting, although it still occur in alkali to calc-alkalic rock type (Sillitoe and Hedenquist, 2003). One distinct characteristics of low sulfidation style is the occurrence of low sulfide minerals such as sphalerite, arsenopyrite, chalcopyrite and pyrite (White and Hedenquist, 1995). Quartz and adularia are major gangue mineral in low sulfidation deposits in association with calcite or sericite (Hedenquist et al., 2000). Minerals such as kaolinite and alunite (±pyrophyllite, diaspora) that are formed under relatively acidic conditions are also common (White and Hedenquist, 1995). Low sulfidation system is associated with mineralizing fluid of low salinity (<1-2wt% NaCl) but gas rich fluid up to (4% gases mainly CO_2 with H_2S). However, there could be more saline fluids (10-15wt% NaCl) when deposit is Ag and base metal rich (Hedenquist and Lowenstern, 1994). Low-sulfidation deposits show a wide variety of textures, including banded, crustiform quartz and chalcedony veins, vein breccias, stockwork and disseminated (Hedenquist et al., 2000; White and Hedenquist, 1995). Examples of low-sulfidation deposits include Round Mountain in Nevada, Kelian in Indonesia, Pajingo in Australia, Emperor in Fiji, Wapolu in Papua New Guinea and Acupan in Philippines (White and Hedenquist, 1990). A model of hydrothermal alteration pattern related to low sulfidation epithermal deposit is shown in Figure (6.2).

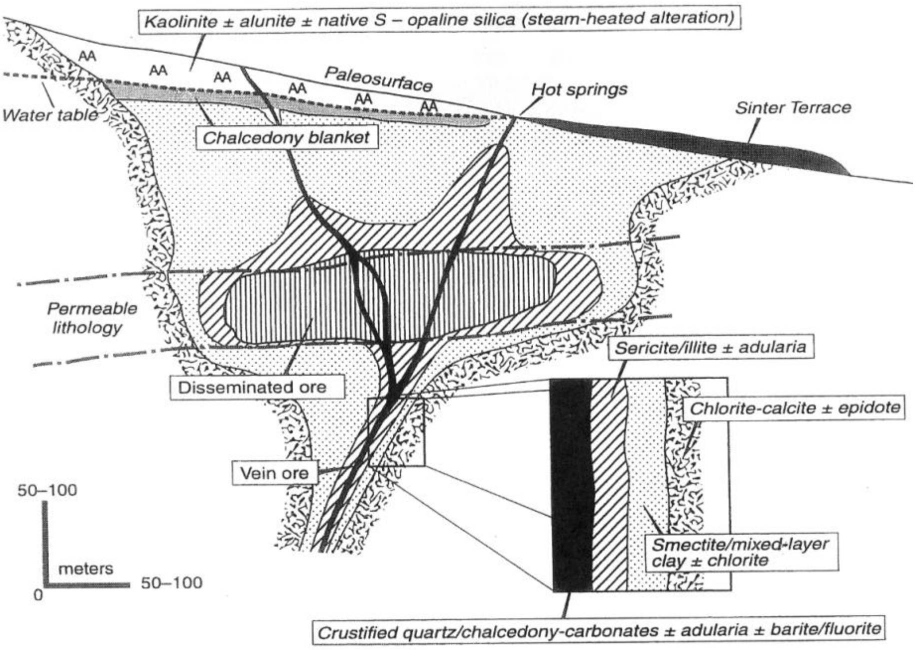

Figure 6.2: Hydrothermal alteration pattern in low sulfidation system (Hedenquist et al., 2000)

6.2. Hydrothermal Alteration of Berecha Area

Results obtained from analysis of hydrothermal alteration mineral in Berecha area indicates the presence of clay minerals such as kaolinite and halloysite (kandite group), montmorillonite and nontronite (smectite group), opal, some alunite, calcite, chlorite and mixture of these minerals. Table 6.1 show summary of characteristic features of Berecha area discovered during this study and its comparison with model of high and low sulfidation system (underline red lines show similar features between Berecha area and the two style of sulfidation).

	High sulfidation	**Low sulfidation**	**Berecha area**
Genetically related volcanic rock	Mainly Andesite to Rhyodacite (calc- alkali magma	Bimodal Rhyolite to Basalt (alkali to calc-alkalic magma)	Bimodal Rhyolite to Basalt
Fluid	Acid pH, probably saline initially	Near-neutral pH, low salinity, gas-rich (CO_2, H_2S)	No observation of pH and salinity
Silicic alteration	Vuggy silica (residual ore bodies); partial to massive silicification; quartz vein and silicified breccias, shallow silicification, including chalcedony and/ or opaline blanket, no sinter	Quartz vein and veinlets, silicified breccias and /or stockwork, shallow silicification, including chalcedony and/ or opaline blanket, silica sinter	Quartz vein, shallow silicification with opaline and chalcedony, some silica sinter noticed
Advanced argillic	*Alunite-kaolinite / dickite-pyrophyllite-diaspore of hypogene origin, typically surrounding silicic cores; also sericite pyrophyllite roots *Kaolinite-alunite blankets of steam heated or supergene origin	*Kaolinite-alunite- (illite / smectite-native sulfur) ± opaline blankets of steam heated origin; commonly underlain by chalcedony blankets *Kaolinite / halloysite -alunite-jarosite blankets o zones supergene origin	*kaolinite +opaline ± alunite likely of steam heated origin
Argillic or Intermediate argillic	Illite and illite / smectite halo to advanced argillic core	Illite / smectite halo to veins; illite ± smectite halo to deeper sericite zones	Montmorillonite and Nontronite (smectite group) present.
Key sulfide species	Enargite, luzonite, covelite, famatinite, pyrite	Sphalerite, galena, arsenopyrite, chalcopyrite, pyrite	Presence of pyrite found
Carbonate gangue	Absent	Present but typically minor	Presence of few occurrence at the surface and bladed calcite seen in some drill core investigated in the area
Other gangue	Barite common, typically late	Barite uncommon, fluorite present locally	Barite not observed in samples analyzed
Main metals	Au-Ag, Cu, As- Sb	Au ± Ag	No observation of main metal (i.e.Au/Ag)
Minor metal	Zn, Pb, Bi, W, Mo, Sn, Hg	Zn, Pb, Cu, Mo, As, Sb, Hg	Pb, Zn, As, Cd, Cu, Fe, Mn, Ni, Sb, Ba, Bi, Li

Table 6.1: Table showing characteristics features of different sulfidation systems after (Sillitoe and Hedenquist, 2003)and that of Berecha area (Metal details - from geochemical analysis of the study area by Ferede Gobena)

From Table (6.1), the effect of hydrothermal alteration of Berecha area is strongly reflected in the bimodal volcanic rock types (rhyolite and basalt) especially on the rhyolite rock. Alteration zonation includes silicification, advanced argillic and argillic. The silicic alteration manifest in form of quartz vein (locally developed) and patches of chalcedony, no evidence of vuggy silica. The most widespread alteration effects are represented essentially in advanced argillic alteration assemblage consisting mainly of kaolinite + opal + smectite ± alunite. Argillic alteration is less in the area with occurrence of some smectite ± illite. Pyrite is found as sulphide mineral in the area with absence of high sulphide minerals like enargite and luzonite usually found in high sulfidation system. Bladed calcites were found in the drill core and few occurrences at the surface. Geochemical result of stream sediment carried out in the area also reveals metals associated with the hydrothermal alteration of Berecha area. The metals analyzed include Pb, Zn, As, Cd, Cu, Fe, Mn, Ni, Sb, Ba, Bi, Li, traces of some of these metals occur in the area but not in high values. The advanced argillic alteration in the area is likely to be of steam heated origin forming within the vadose zone as H_2S oxidizes to sulfate in the presence of atmospheric 0_2 (Hedenquist et al., 2000), evidence of the steaming ground is found in the area (Figure 6.3).

Figure 6.3: Photograph showing steaming ground in part of Berecha area

According to Hedenquist et al (2000), Steam heated water in low sulfidation environment form blankets of kaolinite, smectite, cristobalite (high-temperature polymorph of silica) and locally low alunite and native sulfur which might not have direct relationship to the ore deposit, but such blankets typically overlie the ore in the hanging wall. Sinter type of silicic alteration forming from near neutral pH hot spring at the surface which is one of the distinguishing features of low sulfidation style of epithermal system was also noticed in the area by co-researcher that we study the area together. These characteristics features shows that Berecha area is more related to *low sulfidation system* than high sulfidation system; with low temperature of formation of about 100^0C - 300^0C and shallow depth varying between 100-600 m which is typical of low sulfidation environment (Hedenquist et al., 2000).

Part of mineral map obtained from Berecha area in 3-D view was compared with model of low sulfidation system (Figure 6.4)

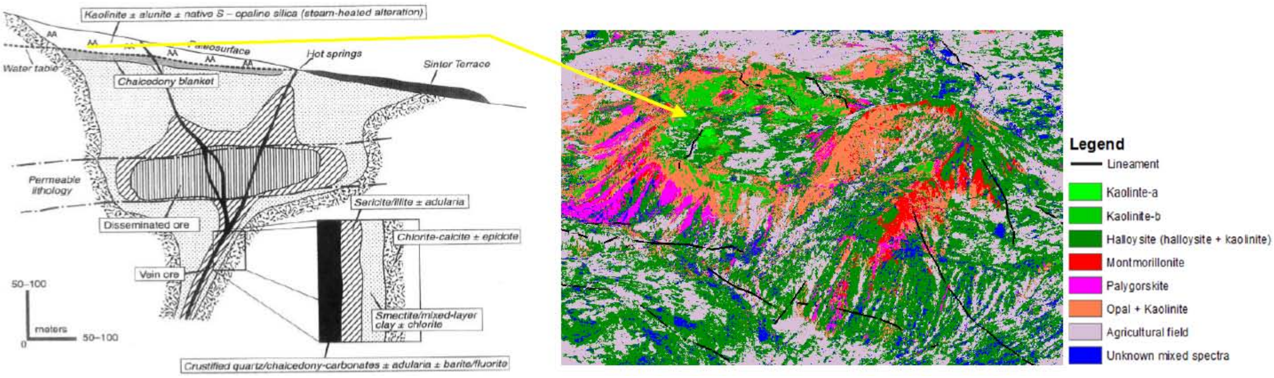

Figure 6.4: Comparison of 3-D model of Berecha alteration (detailed study area) with typical low sulfidation system model

The alteration on top of the crater (on the flat surface) is similar to the steam heated alteration (kaolinite ± alunite ± native sulfur – opaline silica) occurring at the surface in a low sulfidation system model. According to White and Hedenquist (1990), steam heated alteration occur when there is lateral spread of the deep reservoir fluids, boiling and cooling effect as well as fluid-reaction. The alteration in some part of Berecha area is related to this with kaolinite ± alunite ± opal mineral assemblages. Rough (quick) analysis of spectra measurement taken from the drill core (TG-2) in part of the study area [location of drill core close to the area shown in Figure (6.4)] reveals that the alteration minerals changes with depth. Kaolinite occur mainly in the upper part which changes to occurrence of other minerals like smectite (montmorillonite and nontronite), FeChlorite and NH-alunite with depth. The change in alteration minerals with depth in this part of the study area with presence of minerals like smectite and chlorite (low sulfidation mineral assemblage, see Figure 6.4) show more similarity between Berecha area and typical low sulfidation system model. This proves further that Berecha area is related to low sulfidation system and might possibly host significant mineralization.

- **Comparison of Berecha Alteration with World Alteration Systems**

The hydrothermal alteration system of Berecha area can be compared with other alteration systems that exist in other part of the world in terms of geological setting, alteration assemblage pattern, gaugue minerals, among other things. Berecha alteration system is similar to numerous low-sulfidation alteration systems in the *Midas, Sleeper, DeLamar, Mule Canyon districts of Northern Great Basin in Western United States*. The geological setting of alteration system in Northern Great Basin is associated with bimodal rock (rhyolite and basalt), rhyolite domes and volcaniclastic sedimentary rocks; this is similar to that of Berecha area. Similarity is also found in the alteration mineralogy; silicic alteration is found in Northern Great Basin mostly as opal or chalcedony which is also similar to Berecha where shallow silicic alteration occurs as opal, chalcedony and some quartz veins. The mineral assemblage in Northern Great Basin include; opal-chalcedony, quartz, illite/sericite, ±adularia, ±carbonate, ± montmorillonite (John, 2001). Some of these mineral assemblages exist in Berecha area, but mineral like sericite and adularia were not found and only few occurrence of carbonate is present.

Another system in which Berecha alteration system can be compare with is low sulfidation system in *Logan creek in Australia.* Mineralization in Logan creek is associated with Rhyolite and acid tuffs which is similar to rhyolite and pumice pyroclastic tuff in Berecha area. Silicification is common alteration in Logan Creek (White et al., 1995). This is similar to Berecha area although other form of alteration like advanced argillic exists in Berecha area.

Gold mineralization in Northern Great Basin is found in narrow (≤2 m wide), rhythmically banded silica, ± calcite ± adularia veins; hydrothermal tectonic breccias and repeated fault brecciation (John, 2001) while the Au mineralization in Logan creek is found mostly in open spaces veins and also common in stockwork veining (White et al., 1995). Relating these world systems to Berecha area, possible mineralization that might be associated with the alteration can be traced to veins in the alteration part of the study area. Thorough and detailed analysis of spectra measurement taken from the drill core in the study area can also give idea about alteration minerals present in the study area with depth, which can also be a guide to mineral exploration in the study area. Also areas with high anomaly of important metals in geochemical analysis could be a guide to where mineralization is likely to occur. According to White and Hedenquist (1990), studies of alteration mineralogy and zoning may provide valuable insights into the hydrology of a system, and indicate possible sites of deposition of epithermal deposits; however, geochemistry offers a direct approach to locating mineralization. Therefore, the zone of geochemistry anomaly in collaboration with where structural control occurs in form of vein in the altered zone is important in identifying mineralization in the study area.

7. CONCLUSION AND RECOMMENDATION

7.1. Conclusions

In this research, the characteristics of hydrothermal alteration system of Berecha area of Main Ethiopian Rift and the control of structure on their spatial distribution were studied using integrated approach of remotely sensed data (airborne hyperspectral data and LiDAR-DEM data) and field data. Technique such as Wavelength Mapping, Minimum Noise Fraction Transformation and Spectral Angle Mapper (SAM) were used to analyze the hyperspectral data in order to characterize the surface mineralogy of the area. The Wavelength mapping technique differentiate altered areas from unaltered area and also show patterns within the altered areas while Minimum Noise Fraction Transformation pointed out spectrally distinct area present in the study area. SAM algorithm was used for overall classification of the alteration minerals of the study area as well as creation of surficial mineral map. The use of SWIR spectroscopy in acquiring the laboratory spectra of field data combined with remote sensing dataset enable the identification of main alteration areas present in the study area. The earlier stated research questions (section 1.3) and the research findings in this study are summarized below.

Research Question 1: Which lithological units and mineral assemblages can be map from the study area using remote sensing data?

With the application of remote sensing data in collaboration with field data analysis, SWIR spectroscopy was able to detect the main very fine grained mineral assemblages which occur in the study area, including Kaolinite, Halloysite, Opal, Montmorillonite, Nontronite, Calcite, K-alunite, Palygorskite, MgChlorite, Zoisite, Illite and mixture of these minerals. Common minerals in the study area that are found both in the field data and the image include Kaolinite, Halloysite, Opal, Montmorillonite and Palygorskite. Lithological unit of the area was no longer mapped in this study because a published geological map of Main Ethiopian Rift (MER) which covers the study area became available in the course of the research. Digitization of the study area was only carried out from the existing map.

Research Question 2: Do factors like structure and lithology control the spatial distribution of the minerals in the study area?

Factors such as structure and lithology were found to have control on the spatial distribution of the alteration minerals in the study area. The altered areas are distributed along the structures (lineaments) over the study area and also occurring around crater (see Figure 5.19a and 5.19b). The lithology was also observed to control the distribution of alteration minerals in the study area; most of the alteration in the study area is associated with the bimodal volcanic lithological units (mainly rhyolite and basalt). The rhyolitic volcanic rocks host more alteration minerals than the basaltic volcanic rock. Some alteration occurs on pumice pyroclastic deposits and trachyte lithological units with few occurrences in the volcano-sedimentary rock (Alluvial). Kandite minerals in association with opal, smectite and plagioclase occur more in the rhyolitic rock while less of kandite minerals is associated with basaltic rock unit. Minerals with similar composition often occur together in same lithology e.g. kaolinite and halloysite while minerals with different composition are not often seen together (see Figure 5.3a and 5.3b).

Research Question 3: Which type of system is associated with hydrothermal alteration of the study area and can it be compared with systems that occur in some other part of the world?

From comparison of different conceptual model of hydrothermal alteration system with characteristic features associated with alteration of the study area, it can be conclude that Berecha alteration is closely related to ***low sulfidation system***. The features that characterized Berecha area in relation to low sulfidation is discussed in section 6.2 and the table that shows similarity of Berecha area been more related with low sulfidation system than high sulfidation system. Berecha alteration system is similar to other systems that occur in some other parts of the world in terms of geological setting, alteration assemblage pattern, gangue minerals, and other features. Similar features were found in alteration system of Berecha area and Northern Great Basin in Western United States as well as Logan creek in Australia. The two systems are low-sulfidation and host economic quantity of mineralization (mainly Au-Ag). Berecha area also has potential of hosting significant mineralization based on findings discovered in this research about Berecha alteration system in term of geological setting, mineral assemblage, alteration mineral pattern and other characteristics.

7.2. Research Limitations

The limitations encountered in the course of this research were as follows:

- Inadequate wavelength calibration of the AISA Hawk sensor cause a wavelength shift of 2.2 μm absorption features as determined on kaolinite absorption feature, this creates some difficulty in proper analysis of minerals in this region.
- The AISA Hawk data is recently acquired which requires a lot of pre-processing stages and much time was invested in this. As a result, some processing steps such as pixel purity index (PPI) and others steps after MNF which leads to matching unknown spectra to known spectra in order to identify unknown minerals in the image could not be performed due to time frame applicable to this research.
- Factors such as poor accessibility to the study area and rainy season in the area during the fieldwork create a challenge of getting more field data than what was obtained, therefore no ground truth to validate some part of the image.

7.3. Reccommendation

Based on the results obtained and the limitations of this research, the following are recommended:

- Spectral measurements taken from the drill core in the archive of Geological Survey of Ethiopia during field work which was based on their investigation on geothermal and hydrothermal activity in the area study area could be analysis and interpret; this will likely give insight to alteration mineralogy in the area with depth as time frame for this thesis did not permit analysis of the drill core.
- Other processing steps useful in obtaining more information about the study area which cannot be carried out in this research due to time frame should be considered as this could help to have more insight into characteristic of hydrothermal alteration of Berecha area.
- If more field work of detail study will be carried out in nearest future, dry season should be considered appropriate such that enough data will be obtained for effective result and the challenges of muddy road, vehicle stocked etc will not be encountered again

LIST OF REFERENCES

Abebe, B., Acocella, V., Korme, T., and Ayalew, D., 2007, Quaternary faulting and volcanism in the Main Ethiopian Rift: Journal of African Earth Sciences, v. 48, p. 115-124.

Arthur, A.M., 2007, Field Guide for the ASD FieldSpec Pro- Raw DN Mode: National Environmental Research Council - Field Spectroscopy Facility, United Kingdom. http://fsf.nerc.ac.uk/instruments/asd_fieldspec.shtml.

Ayele, A., Teklemariam, M., and Kebede, S., 2002, Geothermal Resource Exploration in the Abaya and Tulu Moye-Gedemsa Geothermal Prospects, Main Ethiopian Rift. , Geological Survey of Ethiopia. Hydrogeology, Engineering Geology and Geothermal Department, p. 176pages.

Azimuth, 2005, AZGCORR User's manual, Airborne Remote Sensing Hyperspectral Direct Georeferencing package, Azimuth Systems (UK).

Bakker, W., 2010, PyEnvi User's manual, ITC, Enschede, Netherlands.

Bishop, A.C., Woolley, A.R., and Hamilton, W.R., 2001, Guide to Mineral, Rocks & Fossils Philip's, a division of Octopus Publishing Group Limited, p. 336.

Boccaletti, M., Bonini, M., Mazzuoli, R., Abebe, B., Piccardi, L., and Tortorici, L., 1998, Quaternary oblique extensional tectonics in the Ethiopian Rift (Horn of Africa): Tectonophysics, v. 287, p. 97-116.

Boccaletti, M., Mazzuoli, R., Bonini, M., Trua, T., and Abebe, B., 1999, Plio-Quaternary volcanotectonic activity in the northern sector of the Main Ethiopian Rift: relationships with oblique rifting: Journal of African Earth Sciences, v. 29, p. 679-698.

Bretar, F., and Chehata, N., 2010, Terrain Modeling From Lidar Range Data in Natural Landscapes: A Predictive and Bayesian Framework: Ieee Transactions on Geoscience and Remote Sensing, v. 48, p. 1568-1578.

Caroline Le Turdua, Tiercelin, J.-J., Gibert, E., Travi, Y., Lezzar, K.-E., Richert, J.-P., Massault, M., Gasse, F.o., Bonnefille, R., Decobert, M., Gensous, B., Jeudy, V., Tamrat, E., Mohammed, M.U., Martens, K., Atnafu, B., Chernet, T., Williamson, D., and Taieb, M., 1999, The Ziway–Shala lake basin system, Main Ethiopian Rift: Influence of volcanism, tectonics, and climatic forcing on basin formation and sedimentation, p. 43pages.

Clark, R.N., Swayze, G.A., Wise, R.A., Livo, K.E., Hoefen, T.M., Kokaly, R.F., and Sutley, S.J., 2007, USGS Digital Spectral Library splib06a, http://speclab.cr.usgs.gov/spectral-lib.html.

Corbett, G.J., and Leach, T.M., 1997, short course manual on Southwest Pacific rim gold-copper systems: Structure, alteration and mineralisation. Chapter 1, Characteristics of gold-copper hydrothermal systems, 12-21 p.

CSIRO, 2010, TSG manual, Commonwealth Scientific and Industrial Research Organisation: Sydney, Australia.

Demessie, M., 1996, Bibliography of the geology of Ethiopia 1870 - 1994: Orléans, Centre International pour la Formation et les Echanges Géologiques (CIFEG), 266 p.

Dipaola, G.M., 1970, Geological-Geothermal Report on the Central part of The Ethiopian Rift Valley: Ethiopia, Geological Survey Of Ethiopia, p. 48.

Forde, A., and Bell, T.H., 1994, Late structural control of mesothermal vein-hosted gold deposits in central Victoria, Australia: Mineralization mechanisms and exploration potential: Ore Geology Reviews, v. 9, p. 33-59.

Goetz, A.F.H., Vane, G., Solomon, J.E., and Rock, B.N., 1985, Imaging Spectrometry for Earth Remote Sensing: Science, v. 228, p. 1147-1153.

Heald, P., Foley, N., and Hayba, D., 1987, Comparative anatomy of volcanic-hosted epithermal deposits; acid-sulfate and adularia-sericite types: Economic Geology, v. 82, p. 1.

Hedenquist, J.W., Arribas, A.R., and Gonzalez-Urien, E., 2000, Exploration for Epithermal Gold Deposits: SEG Reviews, v. 13, p. 245-277.

Hedenquist, J.W., and Lowenstern, J.B., 1994, The role of magmas in the formation of hydrothermal ore deposits: Nature, v. 370, p. 519-527.

Hunt, G.R., 1979, Near-infrared (1.3-2.4 mu m) spectra of alteration minerals; potential for use in remote sensing: Geophysics, v. 44, p. 1974-1986.

Jeremy, P.R., and Richards, M.T., 2004, Structural Controls on Ore Genesis, Reviews in Economic Geology, 181 p.

John, D.A., 2001, Miocene and Early Pliocene Epithermal Gold-Silver Deposits in the Northern Great Basin, Western United States: Characteristics,Distribution, and Relationship to Magmatism: Economic Geology, v. 96, p. 1827-1853.

Korme, T., Acocella, V., and Abebe, B., 2004, The Role of Pre-existing Structures in the Origin, Propagation and Architecture of Faults in the Main Ethiopian Rift: Gondwana Research, v. 7, p. 467-479.

Kruse, F., Boardman, J., and Huntington, J., 2003, Comparison of airborne hyperspectral data and EO-1 Hyperion for mineral mapping: IEEE Transactions on Geoscience and Remote Sensing, v. 41, p. 1388-1400.

Kruse, F.A., 1995, Geologic Mapping Using Combined Analysis of Airborne Visible/Infrared Imaging Spectrometer (AVIRIS) and SIR-C/X-SAR Data: Analytical Imaging and Geophysics

Kruse, F.A., Lefkoff, A.B., Boardman, J.W., Heidebrecht, K.B., Shapiro, A.T., Barloon, P.J., and Goetz, A.F.H., 1993, The spectral image processing system (SIPS)--interactive visualization and analysis of imaging spectrometer data: Remote Sensing of Environment, v. 44, p. 145-163.

NERC-ARSF, 2008, Hyperspectral data quality reports (overview of any issues with data), Final report: National Environmental Research Council - Airborne Research and Survey Facility, United Kingdom. http://www.npm.ac.uk/rsg/projects/arsf/trac/wiki/Reports.

NOAA, 2011, Remote Sensing for Coastal Management, National Oceanic and Atmospheric Administration, http://www.csc.noaa.gov/crs/rs_apps/sensors/lidar.htm.

Pontual, S., Merry, N., and Gamson, P., 1997a, Regolith Logging, Spectral Analysis Guide for Mineral Exploration, G-MEX Vol 8, AusSpec International.

Pontual, S., Merry, N., and Gamson, P., 1997b, Spectral Interpretation Field Manual , Spectral Analysis Guide for Mineral Exploration, G-MEX Vol 1, AusSpec International.

Reed, M., 1997, Hydrothermal alteration and its relationship to ore fluid composition, Geochemistry of hydrothermal ore deposits, Volume Chapter 7, John Wiley and Sons, Inc, p. 303–365.

Rowan, L.C., Schmidt, R.G., and Mars, J.C., 2006, Distribution of hydrothermally altered rocks in the Reko Diq, Pakistan mineralized area based on spectral analysis of ASTER data: Remote Sensing of Environment, v. 104, p. 74-87.

SIC, 2011, Satellite Imaging Corporation, http://www.satimagingcorp.com/satellite-sensors/aster.html.

Sillitoe, R., and Hedenquist, J.W., 2003, Linkages between Volcanotectonic settings, Ore-Fluid Compositions, and Epithermal Precious Metal Deposits: SEG Newsletter, v. Special Publish 10, p. 315-343.

Sun, Y., Seccombe, P.K., and Yang, K., 2001, Application of short-wave infrared spectroscopy to define alteration zones associated with the Elura zinc-lead-silver deposit, NSW, Australia: Journal of Geochemical Exploration, v. 73, p. 11-26.

Tadesse, S., 1999, Geology and Gold Mineralization in the Pan-African Rocks of the Adola Area, Southern Ethiopia: Gondwana Research, v. 2, p. 439-447.

Tadesse, S., Milesi, J.-P., and Deschamps, Y., 2003, Geology and mineral potential of Ethiopia: a note on geology and mineral map of Ethiopia: Journal of African Earth Sciences, v. 36, p. 273-313.

Trua, T., Deniel, C., and Mazzuoli, R., 1999, Crustal control in the genesis of Plio-Quaternary bimodal magmatism of the Main Ethiopian Rift (MER): geochemical and isotopic (Sr, Nd, Pb) evidence: Chemical Geology, v. 155, p. 201-231.

Tsegaye, A., Manetti, P., Bonini, M., Corti, G., Innocenti, F., Mazzarini, F., and Pecksay, Z., 2005, Geological map of the northern Main Ethiopian Rift and its implications for the volcano-tectonic evolution of the rift.

van der Meer, F., 2001, *Basic Physics of Spectrometry*, Chapter 1 of Imaging Spectrometry: Basic Principles and Prospective Applications, Kluwer Academic Publishers, Netherlands, 15 p.

White, N.C., and Hedenquist, J.W., 1990, Epithermal environments and styles of mineralization: Variations and their causes, and guidelines for exploration: Journal of Geochemical Exploration, v. 36, p. 445-474.

White, N.C., and Hedenquist, J.W., 1995, Epithermal Gold Deposits: Style, Characteristics and Exploration: SEG Newsletter, v. 13, p. 1, 9-23.

White, N.C., Leake, M.J., McCaughey, S.N., and Parris, B.W., 1995, Epithermal gold deposits of the southwest Pacific: Journal of Geochemical Exploration, v. 54, p. 87-136.

WoldeGabriel, G., Aronson, J.L., and Walter, R.C., 1990, Geology, geochronology, and rift basin development in the central sector of Main Ethiopia Rift: Geological Society of America Bulletin, v. v. 102, p. 439-458.

Yang, K., Browne, P.R.L., Huntington, J.F., and Walshe, J.L., 2001, Characterising the hydrothermal alteration of the Broadlands-Ohaaki geothermal system, New Zealand, using short-wave infrared spectroscopy: Journal of Volcanology and Geothermal Research, v. 106, p. 53-65.

Yang, K., Huntington, J.F., Boardman, J.W., and Mason, P., 1999, Mapping hydrothermal alteration in the Comstock mining district, Nevada, using simulated satellite-borne hyperspectral data: Australian Journal of Earth Sciences: An International Geoscience Journal of the Geological Society of Australia, v. 46, p. 915 - 922.

APPENDIX

Appendix 01

Table showing different rock type in the study area

ID	STATION	COMMENT / ROCK TYPE	X-COORDINATE	Y-COORDINATE
1	AL_10_001/ 10ch001	Clay minerals	504638	908180
2	AL_10_002/ 10ch002	Trachyte	504744	908157
3	AL_10_003/ 10ch003	Small alteration patch in trachyte	505096	908497
4	AL_10_004/ 10ch004	Big alteration area	507041	908903
5	AL_10_005/ 10ch005	White clay mineral	507005	909025
6	AL_10_006	Fault zone, contain some veins wt pumice area	507830	902062
7	AL_10_007	Pinkish coloured outcrop, trachyte like	503495	909198
8	AL_10_008	Bouldered rock (acidic to Intermediate rock)	503639	908956
9	AL_10_009	River-cut exposure, Altered rock	504093	908039
10	AL_10_010	Acidic-intermediate rock, pumice?	504821	907547
11	AL_10_011	Different types of clay minerals	504988	907410
12	AL_10_012	Rock with reddish colour, (more basic than kaolinite)	504950	907032
13	AL_10_013	Altered red and white clay mineral	505073	905838
14	AL_10_016	Different types of clay minerals	512044	902343
15	AL_10_017	Rock outcrop; original rock becoming weathered	512032	902382
16	AL_10_018	Chalcedony? reddish quartz, Rock with high quartz minerals	512082	902396
17	AL_10_019	Rock type with quartz, feldspar, calcite, on way to borehole alteration	512662	902515
18	AL_10_020	Banded rock, with quartz layering and other minerals	505443	909600
19	AL_10_021	Road cut outcrop of clay mineral	505637	909448
20	AL_10_022	Rocks and minerals with coarse quartz grains	505931	909472
21	AL_10_023	Rocks with different clay minerals	507079	909056
22	AL_10_024	Quartz vein-like in alteration area	507121	909005
23	AL_10_025	Different clay with purple and yellowish material	507253	909022
24	AL_10_026	Chalcedony?	507356	908993
25	AL_10_027	Reddish clay minerals with pumice tuff rock altering to kaolinite	507190	909572
26	AL_10_028	River cut exposure	507462	909483
27	AL_10_031	Different alteration rocks and minerals	507856	907898
28	AL_10_032	Red and white clay minerals	507842	907684
29	AL_10_034	Clay mineral	500922	910276
30	AL_10_035	Pyroclastic and chalcedony outcrop,	503224	909074
31	AL_10_036	Acidic rock area with alteration minerals	503441	908985
32	AL_10_037	White and red clay alteration, close to the top of Mt. Jima	503825	907782
33	AL_10_038	Clay minerals	507646	907117
34	AL_10_039	Pumice pyroclastic tuff? some quartz grains present	507712	907081
35	AL_10_040a	Clay mineral, reddish white	507761	907041
36	AL_10_040b	Clay with some grains	507747	907037
37	AL_10_041	Soil material like	507848	907013
38	AL_10_042	Yellow soil material like	507944	907005
39	AL_10_043	Pyroclastic tuff?	508015	906996
40	AL_10_044	Clay mineral, compact	508078	906940

ID	STATION	COMMENT / ROCK TYPE	X-COORDINATE	Y-COORDINATE
41	AL_10_045	Clay mineral	508156	907041
42	AL_10_046	Rock with different mineral	508208	907179
43	AL_10_047	Clay mineral, reddish colour	508281	907213
44	AL_10_048	Clay mineral, reddish white	508313	907250
45	AL_10_049	Clay mineral: reddish white	508366	907075
46	AL_10_050	White clay mineral	508425	907054
47	AL_10_051	White clay: compacted	508542	907093
48	AL_10_052	Clay mineral, with banded type of clay mineral	508454	907128
49	AL_10_053	Clay minerals within alluvial deposit	508510	907264
50	AL_10_054	Clay mineral	508530	907339
51	AL_10_055	Cloudy white clay mineral	508641	907358
52	AL_10_056	Red clay mineral	508707	907259
53	AL_10_057	White clay mineral	508821	907201
54	AL_10_058	Clay mineral, pure white colour	508849	907180
55	AL_10_059	Clay mineral, reddish white	508887	907171
56	AL_10_060	Cloudy white clay mineral	508942	907150
57	AL_10_061	Different clay mineral types	508973	907130
58	AL_10_062	Purple colour clay mineral	508992	907142
59	AL_10_063	Clay mineral with different colour	509072	907124
60	AL_10_064	Quartz vein? / opal fissure	509098	907236
61	AL_10_065/ 10ch006	Clay mineral	505924	909456
62	AL_10_066/ 10ch007	Clay mineral	505544	909393
63	AL_10_067/ 10ch008	Quartz vein piece in hillside rubble	508221	901842
64	AL_10_068/ 10ch009	Quartz vein	508064	902007
65	AL_10_069/ 10ch011	Quartz vein 5cm in situ; strike 350	507903	902011
66	AL_10_070/ 10ch014	Clay mineral	508956	906274
67	AL_10_071/ 10ch015	Silified vein-like?	509282	906172
68	AL_10_072 / 10ch016	Clay mineral top of ridge	510226	905434
69	AL_10_073/ 10ch017	Clay mineral, with some quartz	510267	905320
70	AL_10_074/ 10ch019	Pumice breccia with quartz	509338	905941
71	AL_10_075/ 10ch020	Quartz vein pieces everywhere along 330	509131	906277
72	AL_10_076/ 10ch021	clay mineral	509204	906938
73	AL_10_077/ 10ch022	clay mineral	509211	906989
74	AL_10_078/ 10ch023	clay mineral	509208	907058
75	AL_10_079/ 10ch024	clay mineral	509193	907087
76	AL_10_080/ 10ch025	clay mineral	509115	907185
77	AL_10_081/ 10ch026	Abundant quartz veins	508963	907553
78	AL_10_082/ 10ch027	clay mineral	500980	902344
79	AL_10_083/ 10ch028	clay mineral	499860	901813
80	AL_10_084/ 10ch029	clay mineral	499853	901790
81	AL_10_085/ 10ch030	clay mineral	499819	901738
82	AL_10_086/ 10ch031	clay mineral	499891	901799
83	AL_10_087/ 10ch032	Weathered pumice on hillside	500069	901807

Appendix 02

Table showing TSG and results from other methods applied in analyzing the 83 mineral and rock samples

ID	STATION No	Mineral_1	Mineral_2	Mineral_3	X - Coordinate	Y- Coordinate
1	AL_10_001/ 10ch001	Kaolinite	Null	Null	504638	908180
2	AL_10_002/ 10ch002	Opal	Null	Null	504744	908157
3	AL_10_003/ 10ch003	Kaolinite	Null	Null	505096	908497
4	AL_10_004/ 10ch004	Kaolinite	Null	Null	507041	908903
5	AL_10_005/ 10ch005	Kaolinite	Null	Null	507005	909025
6	AL_10_006	Opal	MgChlorite	Null	507830	902062
7	AL_10_007	Kaolinite	Opal	Halloysite	503495	909198
8	AL_10_008	Opal	Palygorskite	Null	503639	908956
9	AL_10_009	Opal	K-alunite	Null	504093	908039
10	AL_10_010	Montmorillonite	Halloysite	Null	504821	907547
11	AL_10_011	K-alunite	Kaolinite	Halloysite	504988	907410
12	AL_10_012	Kaolinite	Halloysite	Null	504950	907032
13	AL_10_013	Montmorillonite	Kaolinite	Halloysite	505073	905838
14	AL_10_016	K-alunite	Kaolinite	Halloysite	512044	902343
15	AL_10_017	Opal	Null	Null	512032	902382
16	AL_10_018	Opal	Nontronite	Halloysite	512082	902396
17	AL_10_019	Opal	Kaolinite	K-alunite	512662	902515
18	AL_10_020	Kaolinite	Opal	Null	505443	909600
19	AL_10_021	Kaolinite	Null	Null	505637	909448
20	AL_10_022	Opal	Kaolinite	Halloysite	505931	909472
21	AL_10_023	Nontronite	Opal	Halloysite	507079	909056
22	AL_10_024	Opal	Kaolinite	Halloysite	507121	909005
23	AL_10_025	Kaolinite	Halloysite	Null	507253	909022
24	AL_10_026	Opal	Kaolinite	Null	507356	908993
25	AL_10_027	Kaolinite	Opal	Halloysite	507190	909572
26	AL_10_028	Halloysite	Kaolinite	Palygorskite	507462	909483
27	AL_10_031	Opal	Kaolinite	Montmorillonite	507856	907898
28	AL_10_032	Kaolinite	Opal	Null	507842	907684
29	AL_10_034	Kaolinite	Halloysite	Null	500922	910276
30	AL_10_035	Montmorillonite	Opal	Halloysite	503224	909074
31	AL_10_036	Kaolinite	Halloysite	Null	503441	908985
32	AL_10_037	Kaolinite	Halloysite	Null	503825	907782
33	AL_10_038	Opal	Kaolinite	Null	507646	907117
34	AL_10_039	Opal	Halloysite	Kaolinite	507712	907081
35	AL_10_040a	Kaolinite	Halloysite	Null	507761	907041
36	AL_10_040b	Montmorillonite	Halloysite	Opal	507747	907037
37	AL_10_041	Opal	Palygorskite	Null	507848	907013
38	AL_10_042	Montmorillonite	Null	Null	507944	907005
39	AL_10_043	Opal	Palygorskite	Null	508015	906996
40	AL_10_044	Kaolinite	Halloysite	Null	508078	906940

ID	STATION	Mineral_1	Mineral_2	Mineral_3	X-Coordinate	Y-Coordinate
41	AL_10_045	Kaolinite	Halloysite	Null	508156	907041
42	AL_10_046	Opal	Null	Null	508208	907179
43	AL_10_047	Kaolinite	Null	Null	508281	907213
44	AL_10_048	Kaolinite	Null	Null	508313	907250
45	AL_10_049	Kaolinite	Halloysite	Null	508366	907075
46	AL_10_050	Kaolinite	Halloysite	Null	508425	907054
47	AL_10_051	Kaolinite	Opal	Halloysite	508542	907093
48	AL_10_052	Kaolinite	Halloysite	Null	508454	907128
49	AL_10_053	Kaolinite	Halloysite	Opal	508510	907264
50	AL_10_054	Kaolinite	Null	Null	508530	907339
51	AL_10_055	Kaolinite	Null	Null	508641	907358
52	AL_10_056	Kaolinite	Opal	Halloysite	508707	907259
53	AL_10_057	Kaolinite	Halloysite	Null	508821	907201
54	AL_10_058	Kaolinite	Halloysite	Null	508849	907180
55	AL_10_059	Kaolinite	Halloysite	Null	508887	907171
56	AL_10_060	Kaolinite	Halloysite	Null	508942	907150
57	AL_10_061	Halloysite	Kaolinite	Null	508973	907130
58	AL_10_062	Kaolinite	Null	Null	508992	907142
59	AL_10_063	Kaolinite	Halloysite	K-alunite	509072	907124
60	AL_10_064	Opal	Null	Null	509098	907236
61	AL_10_065/ 10ch006	Kaolinite	Null	Null	505924	909456
62	AL_10_066/ 10ch007	Kaolinite	Null	Null	505544	909393
63	AL_10_067/ 10ch008	Opal	Montmorillonite	Null	508221	901842
64	AL_10_068/ 10ch009	Opal	Null	Null	508064	902007
65	AL_10_069/ 10ch011	Opal	Null	Null	507903	902011
66	AL_10_070/ 10ch014	Opal	Palygorskite	Null	508956	906274
67	AL_10_071/ 10ch015	Kaolinite	Null	Null	509282	906172
68	AL_10_072 / 10ch016	Nontronite	Opal	Zoisite	510226	905434
69	AL_10_073/ 10ch017	Halloysite	Montmorillonite	Opal	510267	905320
70	AL_10_074/ 10ch019	Opal	MgChlorite	Null	509338	905941
71	AL_10_075/ 10ch020	Opal	Null	Null	509131	906277
72	AL_10_076/ 10ch021	Opal	Null	Null	509204	906938
73	AL_10_077/ 10ch022	Calcite	Montmorillonite	Null	509211	906989
74	AL_10_078/ 10ch023	Kaolinite	Opal	Null	509208	907058
75	AL_10_079/ 10ch024	Kaolinite	Null	Null	509193	907087
76	AL_10_080/ 10ch025	Kaolinite	Opal	Null	509115	907185
77	AL_10_081/ 10ch026	Halloysite	Opal	illite	508963	907553
78	AL_10_082/ 10ch027	Opal	Halloysite	Null	500980	902344
79	AL_10_083/ 10ch028	Opal	Null	Null	499860	901813
80	AL_10_084/ 10ch029	Opal	Halloysite	Null	499853	901790
81	AL_10_085/ 10ch030	Opal	Halloysite	Null	499819	901738
82	AL_10_086/ 10ch031	Opal	Null	Null	499891	901799
83	AL_10_087/ 10ch032	Opal	Halloysite	Null	500069	901807

Appendix 03

Table showing Kaolinite crystallinity index values from Field data

ID	STATION Number	Kaolinite Crystallinity index	Crystallinity Code	Mineral_1	Mineral_2	Mineral_3
1	AL_10_001/ 10ch001	1.024	K4a	Kaolinite	Null	Null
2	AL_10_003/ 10ch003	1.094	K4b	Kaolinite	Null	Null
3	AL_10_004/ 10ch004	1.049	K4b	Kaolinite	Null	Null
4	AL_10_005/ 10ch005	1.071	K4b	Kaolinite	Null	Null
5	AL_10_007	1.044	K4b	Kaolinite	Opal	Halloysite
6	AL_10_011	1.05	K4b	K-alunite	Kaolinite	Halloysite
7	AL_10_012	1.029	K4a	Kaolinite	Halloysite	Null
8	AL_10_013	1.035	K4a	Montmorillonite	Kaolinite	Halloysite
9	AL_10_016	1.011	K4a	K-alunite	Kaolinite	Halloysite
10	AL_10_019	1.016	K4a	Opal	Kaolinite	K-alunite
11	AL_10_020	1.053	K4b	Kaolinite	Opal	Null
12	AL_10_021	1.052	K4b	Kaolinite	Null	Null
13	AL_10_022	1.026	K4a	Opal	Kaolinite	Halloysite
14	AL_10_023	1.096	K4b	Nontronite	Opal	Halloysite
15	AL_10_025	1.071	K4b	Kaolinite	Halloysite	Null
16	AL_10_027	1.056	K4b	Kaolinite	Opal	Halloysite
17	AL_10_028	1.062	K4b	Halloysite	Kaolinite	Palygorskite
18	AL_10_031	1.045	K4b	Opal	Kaolinite	Montmorillonite
19	AL_10_032	1.074	K4b	Kaolinite	Opal	Null
20	AL_10_034	1.064	K4b	Kaolinite	Halloysite	Null
21	AL_10_035	1.077	K4b	Montmorillonite	Opal	Halloysite
22	AL_10_036	1.066	K4b	Kaolinite	Halloysite	Null
23	AL_10_037	1.05	K4b	Kaolinite	Halloysite	Null
24	AL_10_038	1.062	K4b	Opal	Kaolinite	Null
25	AL_10_039	1.032	K4a	Opal	Halloysite	Kaolinite
26	AL_10_040a	1.071	K4b	Kaolinite	Halloysite	Null
27	AL_10_044	1.052	K4b	Kaolinite	Halloysite	Null
28	AL_10_045	1.047	K4b	Kaolinite	Halloysite	Null
29	AL_10_047	1.084	K4b	Kaolinite	Null	Null
30	AL_10_048	1.109	K4b	Kaolinite	Null	Null
31	AL_10_049	1.062	K4b	Kaolinite	Halloysite	Null
32	AL_10_050	1.083	K4b	Kaolinite	Halloysite	Null
33	AL_10_051	1.057	K4b	Kaolinite	Opal	Halloysite
34	AL_10_052	1.067	K4b	Kaolinite	Halloysite	Null
35	AL_10_053	1.036	K4b	Kaolinite	Halloysite	Opal
36	AL_10_054	1.075	K4b	Kaolinite	Null	Null
37	AL_10_055	1.083	K4b	Kaolinite	Null	Null
38	AL_10_056	1.048	K4b	Kaolinite	Opal	Halloysite
39	AL_10_057	1.107	K4b	Kaolinite	Halloysite	Null
40	AL_10_058	1.076	K4b	Kaolinite	Halloysite	Null
41	AL_10_059	1.077	K4b	Kaolinite	Halloysite	Null
42	AL_10_060	1.059	K4b	Kaolinite	Halloysite	Null
43	AL_10_061	1.082	K4b	Halloysite	Kaolinite	Null
44	AL_10_062	1.048	K4b	Kaolinite	Null	Null
45	AL_10_063	1.042	K4b	Kaolinite	Halloysite	K-alunite
46	AL_10_065/ 10ch006	1.078	K4b	Kaolinite	Null	Null
47	AL_10_066/ 10ch007	1.06	K4b	Kaolinite	Null	Null
48	AL_10_071/ 10ch015	1.059	K4b	Kaolinite	Null	Null
49	AL_10_078/ 10ch023	1.016	K3	Kaolinite	Opal	Null
50	AL_10_079/ 10ch024	1.12	K4b	Kaolinite	Null	Null
51	AL_10_080/ 10ch025	1.06	K4b	Kaolinite	Opal	Null